新規希土類酸化物の構造と機能発現メカニズムの解明およびダイナミクスに関する研究

（研究課題番号 21560704）

平成 21 年度~23 年度科学研究費補助金　（基盤（c））

研究成果報告書

平成 24 年 3 月

研究代表者　　中野裕美・准教授
研究者番号 00319500

（豊橋技術科学大学　研究基盤センター）

はしがき

本冊子は、平成 21 年度から 23 年度の 3 年間にわたり交付された、「**新規希土類酸化物の構造と機能発現メカニズムの解明およびダイナミクスに関する研究**」を研究課題とする科学研究費補助金　基盤（c）（研究課題番号 21560704）の研究成果報告書である。

研究期間に関わる 3 年間は、主にペロブスカイト関連構造を有する希土類酸化物のダイナミクスに関する研究をはじめ、新機能を有する酸化物の合成・開発を行い、材料の機能発現メカニズムについて複合的手法により解明する研究を行ってきた。ダイナミクスに関わる研究については、石沢伸夫教授（名古屋工業大学）に、精度の高い高温 X 線回折測定や構造解析に関する多大な助言を頂いた。また、酸化物合成については、(有)MSP の三宅正司取締役（大阪大学名誉教授）との出会いがあり、佐治他三郎氏にミリ波照射を用いた低温・短時間合成をご協力いただき、予想以上の成果を収めることができた。新機能を有する無機材料の合成・開発においては、23 年度に最初に配属された学生(大園君)の卒業研究で、今後の研究につながる新しい無機材料の合成ができ、心を躍らせている。

この 3 年間は、21 年 6 月に龍谷大学から豊橋技術科学大学に赴任し、新天地での研究を立ち上げる期間でもあり、多くの方々に支えられた。研究基盤センター長　若原昭浩教授、滝川浩史教授、豊橋キャンパスイノベーション　亀頭直樹社長(豊橋技術科学大学名誉教授)には、慣れない環境の中で多くのご助言や励ましをいただき、研究の幅が広がったことによって、予想以上の成果を得ることができた。京都大学　馬渕守教授、袴田昌高助教、湯浅元仁博士、名古屋工業大学　福田功一郎教授、東京工業大学　八島正知教授、豊橋技術科学大学山田基弘助教には、研究の面で多くのご助言、ご協力をいただいた。

今回もまたすてきな方々と出会い、ここに一定の成果をまとめられたことを心から喜び、深く感謝の意を表する。

平成 24 年 3 月吉日

豊橋技術科学大学
研究基盤センター
准教授　中野裕美

科学研究費補助金　（基盤（c））

期間：平成 21 年度から 23 年度

研究課題：**新規希土類酸化物の構造と機能発現メカニズムの解明およびダイナミクスに関する研究**

研究課題番号：21560704

研究代表者：中野裕美（豊橋技術科学大学　准教授）

研究者番号：00319500

研究経費：　平成 21 年度 2,080 千円　(内　間接経費　480 千円)

平成 22 年度　910 千円（内　間接経費 210 千円）

平成 23 年度　780 千円（内　間接経費 180 千円）

総合計 3,770 千円（内　間接経費 870 千円）

原著論文(査読付き)

1. “Rapid synthesis and structural analysis of Li-Nb-Ti-O solid solutions with superstructure by millimeter-wave heating” H. Nakano, T. Saji, M. Yuasa, S. Miyake, and M. Mabuchi, *J. Ceram. Soc. Jpn.***119** (11) (2011) 808-812.
2. “The Effect of Post Treatments on the Powder Morphology of Titanium Dioxide (TiO_2) Powders Synthesized for Cold Spray” T. Salim, M. Yamada, H. Nakano, K. Shima, H. Isago, M. Fukumoto, *Surface and Coatings Technology* **206** (2011)366-371.
3. “Microstructure and luminescence of rare earth doped $Li(Nb,Ti)O_3$ solid solutions, H. Hayashi, H. Nakano, *Materials Science and Engineering*, **18** (2011) 082018.
4. “Crystal structures of solid solution $(Ba_{1-x}Ca_x)(Sc_{1/2}Nb_{1/2})O_3$ system” H. Nakano , T. Ida , M. Takemoto , H. Ikawa, *Materials Science and Engineering*, **18** (2011) 082023.
5. “The Synthesis of Titanium Dioxide (TiO_2) Powder for Cold Spray Process” N Tjitra Salim, M Yamada, *H Nakano* and M Fukumoto *Materials Science and Engineering* **18** (2011) 032019.
6. “Microstructural evidence of Hall mobility anisotropy in c-axis textured Al-doped ZnO “Y. Kinemuchi, H. Nakano, H. Kaga, S. Tanaka, K. Uematsu, and K. Watari *J. Am. Ceram .Soc.* **94** [8] 2339–2343 (2011)
7. *“*Microstructure of interfacial region between cold-splayed copper coating and AlN substrate coated with sputtered titanium and copper” H. Nakano, M. Yamada, M. Fukumoto, E. Yamaguchi, *J. Thermal Spray Technology.* **20**(3) 407-411 (2011).
8. “Synthesis and structural characterization of a new aluminum oxycarbonitride, $Al_5(O, C, N)_4$”H. Inuzuka; M. Kaga; D. Urushihara; H. Nakano,T. Asaka, K. Fukuda, *Journal of Solid State Chemistry* **183**（2010）2570-2575.
9. “Enhanced boundary-scattering of electrons and photons in nanograined zinc oxide” Y. Kinemuchi, H. Naknao, M. Mikami, K. Kobayashi, K. Watari, Y. Hotta, *J. Appl. Phys.* **108**, (2010) 053721.
10. “Hydrogen gas reaction with Eu^{3+}-dopes Al_2O_3-SiO_2 glasses” M. Nogami, K. Watanabe, Y. Ito, H. Ito, H. Nakano, *J. Am. Ceram. Soc.* **93**(6) (2010) 1663-1667.
11. “Cold spraying of TiO_2 photocatalyst coating with nitrogen process gas” M. Yamada, H. Isago, H. Nakano, M. Fukumoto, *J. Thernal. Spray Technology* **19**(6) (2010) 1218-1223.
12. *“Imma* Perovskite-Type Oxynitride $LaTiO_2N$ Structure and Electron Density” M. Yashima,, M. Saito, H. Nakano, T. Takata, K. Ogisu, and K.Domen,,*Chem.Comm.* **46**(2010) 4704-4706.

13. “Evaluation and preparation of $Li_{1+x-y}Nb_{1-x-3y}Ti_{x+4y}O_3$ solid solution with superstructure as new phosphor” H. Hayashi, H. Nakano, *J. Alloys and Compounds.* **502**（2010）360-364.

14. “Microstructure and luminescence of Eu-doped $Li_{1+x-y}Nb_{1-x-3y}Ti_{x+4y}O_3$ solid solutions with superstructure” H. Hayashi, H. Nakano and M. I .Jones, *J. Ceram. Soc. Jpn*. **118**(3) (2010),226-230.

15. “Synthesis and Structural Characterization of Al_4SiC_4-Homeotypic Aluminum Silicon Oxycarbide, $[Al_{4.4}Si_{0.6}][O_{1.0}C_{2.0}]C$,” M. Kaga, T. Iwata, H. Nakano, and K. Fukuda, *J. Solid State Chem.*, **183**,（2010）636-642.

16. “Fabrication of ZnO ceramics using ZnO/Al_2O_3 nanocomposite particles prepared by mechanical treatment” S. Tasaki, J. Tatami, H. Nakano, T. Wakihara, K. Komeya and T. Meguro, *J. Ceram. Soc. Jpn*, **118**(2),(2010),118-121.

17. “In-situ observation of phase transformations in layered perovskite $BaEu_2Mn_2O_7$” H. Nakano, N. Ishizawa, N. Kamegashira, *J. Europ.Ceram.Soc*. 30(2010) 233-236.

18. “First discovery and structural characterization of a new compound in Al-Si-O-C system” T. Iwata, M. Kaga, H. Nakano, K. Fukuda, *J. Solid State Chem.* **182** (2009) 2252-2260.

19. “Changes by annealing in grain boundaries for Co-Cu alloy with nanolamellar structure” H. Nakano, M. Yuasa, M. Mabuchi, *Spripta Materialia*, **61**(4) (2009) 371-374.

20. “Syntheses and crystal structures of Ge-bearing layered carbides $Zr_2Al_4C_5$ and $Zr_3Al_4C_6$” K. Sugiura, T. Iwata, N. Sunada, S. Hashimoto, H. Nakano, K. Fukuda, *J. Ceram. Soc. Jpn.* **117**(1), (2009) 22-26.

Proceedings

21. “Rapid synthesis and evaluation of Li-Nb-Ti-O M-phase solid solutions by millimeter-wave heating” H. Nakano, K. Ozono, T. Saji, S. Miyake, H. Hayashi, *Proceedings of ECERS XII*, Stockholm, Sweden, Jun 20-23 (2011).CD

22. “Crystal structure and phase transition of $(Sr_{0.67}Ln_{0.33})(Mn_{0.33}Ti_{0.67})O_3$(Ln: Nd, Sm, Eu, Gd)” H. Nakano, K. Fukuda, M. Kobayashi, N. Kamegashira, *Proceedings of ECERS XII*, Stockholm, Sweden, Jun 20-23 (2011).CD

23. “Relationship Between Microstructure and Hardness of ZrN/TiN Multi-Layers with Various Bilayer Thicknesses” Y. Aoi**,** S. Furuhata and H. Nakano, *Advances in Science and Technology* Vol **63** (2010) pp.392-395.

24. *"In-situ* measurement of phase transition of layered perovskite $BaLn_2Mn_2O_7$" H. Nakano**,** N. Ishizawa, H. Sato, N. Kamegashira, *Advances in Science and Technology* Vol.**67** (2010) pp.113-117.
25. *"In-situ* TEM Observation of Crystallization Process for $LiNbO_3$ and $NaNbO_3$"H. Naknao, Y. Suyama. *Advances in Science and Technology* vol.**63** (2010) pp.47-51.
26. "Characterization of the Product of the Reaction between Layered FeOCl and $C_5H_{11}ONa$" T. Shiono, F. Tando, H. Nakano and Y. Sugahara, *U.S.-Japan Joint Workshop on Future Trends in Organic-Inorganic Nanocomposite Hybrid Materials NANO HYBRIDS 2009* May 12-May 16, Himeji (2009) pp39.
27. "Influence of grain-boundary on textured Al-ZnO" Y. Kinemuchi, H. Kaga, S. Tanaka, K. Uematsu, H. Nakano, K. Watari", *Ceramic Engineering and Science proceedings* **29**(10) (2009) pp 63-68.
28. "Macro- and Micro-scale thermal conductivities of SiC single crystal and ceramic" I. Yamada, S. Kume, H. Nakano, K. Watari, *Key Engineering Materials*(2009) pp 179-183.

学会発表

1. 希土類添加Li-Nb-Ti-O蛍光体の合成と構造解析　大園啓太・中野裕美,佐治他三郎、三宅正司、小林美学　日本セラミックス協会年会　京都大学　(2012)3/19-21.
2. 層状ペロブスカイトの一次相転移その場観察　中野裕美、石沢伸夫、日本セラミックス協会年会　京都大学　(2012)3/19-21.
3. ゲルマニウム系ゼオライト類似化合物の形態制御　平靖之、地井元規、中野裕美、日本セラミックス協会年会　京都大学　(2012)3/19-21.
4. ソーダライト型アルミのゲルマニウム酸塩の合成と評価　平靖之、地井元規、五十嵐睦夫、中野裕美、日本セラミックス協会年会　京都大学　(2012)3/19-21.
5. ミリ波照射による希土類添加Li-Nb-Ti-O蛍光体の焼結と発光特性　大園啓太、中野裕美、林裕之、佐治他三郎、三宅正司、　日本セラミックス協会東海支部学術研究発表会　（名古屋工業大学）(2011) 12/3　p29.
6. 希土類添加Li-Nb-Ti-O蛍光体のミリ波加熱による低温短時間合成と発光特性 大園啓太、 中野裕美・ 林裕之・ 佐治他三郎、三宅正司、日本セラミックス協会秋季シンポジウム、北海道大学、(2011)9/7-9 p295.
7. 希土類添加Li-Nb-Ti-O蛍光体の短時間合成のための助剤の検討　林　裕之、大園啓太、中野裕美、日本セラミックス協会秋季シンポジウム、北海道大学、(2011)9/7-9 p288.

8. 機械的処理による$BaCO_3$／TiO_2ナノ複合粒子を用いた$BaTiO_3$ナノ粒子の合成 橋本厚、多々見純一、目黒竹司、脇原徹、米屋勝利、中野裕美、井上真希、小西幸宏、鈴木利昌、日本セラミックス協会秋季シンポジウム、北海道大学、(2011)9/7-9 p305.
9. 高速衝突固体セラミックス粒子の金属機材表面への付着挙動　山田基弘、島幸一郎、M. E. Dicknson, N. T. Salim, 中野裕美、福本昌宏、日本セラミックス協会秋季シンポジウム、北海道大学、(2011)9/7-9 p225.
10. The Bonding Mechanism of Cold Sprayed TiO_2 Coating、N. Tjitra Salim, H. Nakano, M. Yamada, M. Fukumoto、日本材料学会セラミック材料部門委員会講演会　7/13　京都工芸繊維大学　(2011)7/13 p9-10.
11. 光触媒酸化チタン成膜におけるコールドスプレー法とサスペンション溶射法の比較　山田基宏, 砂金寛昭, N.T. Salim, 中野裕美, 福本昌宏, F.-L. Toma, S. Langner, L.-M. Berger, 日本溶射学会　第93回（2011年度春季）全国講演大会, (2011)6/6-7　大阪.
12. Li-Nb-Ti系酸化物の構造異方性が作り出したミリ波照射による美的ナノ組織、中野裕美、佐藤裕久、湯浅元仁、馬渕守日本セラミックス協会2011年年会、静岡大学 (2011)3/16-18, p361.
13. Al-Si-O-C系における新物質群の結晶構造と分域構造、加賀元了、漆原大典、中野裕美、福田功一郎、日本セラミックス協会2011年年会、静岡大学　(2011)3/16-18, p68.
14. 排ガス浄化触媒セリアージルコニアナノ粒子の結晶構造解析、佐藤大祐、八島正知、脇田崇弘、中野裕美、日本セラミックス協会2011年年会、静岡大学　(2011)3/16-18, p92.
15. コールドスプレーおよびサスペンション溶射により作成した光触媒酸化チタン被膜の特性、山田基弘、砂金寛昭、N.T.Salim,中野裕美、福本昌宏、日本セラミックス協会2011年年会、静岡大学　(2011)3/16-18,p125.
16. The effect of substrates on adhension strength of cold-sprayed TiO_2 coating , N.T.Salim,M. Yamada, H. Isago, H. Nakano, M. Fukumoto, 日本セラミックス協会2011年年会、静岡大学　(2011)3/16-18,p125.
17. 超構造を有するLi_2O-Nb_2O_5-TiO_2系固溶体のミリ波照射による低温短時間合成の試み　中野裕美、湯浅元仁、佐治他三郎、佐藤裕久、三宅正司、馬渕守、第４９回基礎科学討論会　岡山コンベンションセンター　(2011)1/11-12 p24.

18. Al-Si-O-C系における複合酸炭化物の発見と生成反応の熱力学的考察　漆原大典、加賀元了、中野裕美、浅香透、福田功一郎、第４９回基礎科学討論会　岡山コンベンションセンター　(2011)1/11-12 p43.
19. *Imma* ペロブスカイト型酸窒化物LaTiO2N,結晶構造と電子密度分布○齊藤未央・八島正知・中野裕美・高田剛・荻巣清徳・堂免一成（東工大院総理工・豊橋技科大研究基盤セ・東大院工）平成22年度 日本結晶学会年会、大阪大学コンベンションセンター（吹田キャンパス）(2010)12/3-5.
20. コールドスプレー法によるAlN基板へのCu膜形成と接合界面の微構造　中野裕美、山田基宏、福本昌宏　日本材料学会セラミック材料部門委員会講演会　7/13　京都工芸繊維大学　（2010）.
21. 溶射およびコールドスプレー銅粒子の付着メカニズム 山田基宏, 中野裕美, 福本昌宏 日本溶射協会　第９１回（２０１０年度春季）全国講演大会 (2010)7/5-6　大阪市.
22. FeOClとn-C5H11ONaの反応から生成するγ-Fe2O3のキャラクタリゼーション　塩野岳史、丹藤文彰、中野裕美、菅原義之、日本セラミックス協会年会　　東京農工大(2010)3/22-24 p188.
23. SNDMによるAl添加ZnOのミクロスケール電気特性評価　田崎智子、多々見純一、脇原徹、米屋勝利、目黒竹司、中野裕美、北條純一、　東京農工大(2010)3/22-24 p17.
24. アナターゼ型酸化チタンの大気中高速成膜、砂金寛昭、山田基宏、中野裕美、福本昌宏、　東京農工大(2010)3/22-24　p66.
25. *Imma*ペロブスカイト型酸窒化物$LaTiO_2N$結晶構造と電子密度分布、斎藤未央、八島正和、中野裕美、高田剛、荻巣清徳、堂免一成、　東京農工大(2010)3/22-24 p78.
26. 機械的処理による複合粒子を用いた$BATiO_3$ナノ粒子の合成、橋本厚、多々見純一、中野裕美、脇原徹、米屋勝利、目黒竹司　　東京農工大(2010)3/22-24 P171.
27. ZrN/TiN薄膜の積層周期と界面整合性　古畑哲、中野裕美、青井芳史、日本セラミックス協会年会写真展　　東京農工大(2010)3/22-24（2010）
28. 層状炭化物ホモロガス相の合成および結晶構造解析　岩田知之、杉浦啓太、中野裕美、福田功一郎　日本セラミックス協会基礎討論会　沖縄コンベンションセンター　(2010)1/2-13.
29. 可視光応答型光触媒$LaTi_2NO$の結晶構造と電子密度分布、斎藤真央、八島正和、中野裕美、高田剛・荻巣清徳・堂免一成　日本結晶学会年年会　関西学院大学(2010)12/5-6　.

30. First discovery and structural characterization of a new compound in Al-Si-O system 加賀元了、岩田知之、中野裕美、福田功一郎、日本セラミックス協会東海支部学術研究発表会 名古屋大学 (2009) 11/28p32.
31. 無機層状化合物FeOClと*n* -$C_5H_{11}ONa$の反応による有機誘導体および□-Fe_2O_3の合成 塩野岳史、丹藤 文彰、中野裕美、菅原 義之 21年度粉末冶金秋季大会 名古屋国際会議場 (2009) 10/27-29 .
32. 層状炭化物ホモロガス相$(MC)_l(T_4C_3)m$（M＝Zr、Y and Hf, T = Al, Si and Ge）の結晶構造 杉浦啓太、岩田知之、中野裕美、福田功一郎 日本セラミックス協会秋季シンポジウム（愛媛大）（2009）9/16-18 p177.
33. 機械的処理によるAlN-Y_2O_3ナノ複合粒子を用いて作成したAlNセラミックスの微構造と電気的特性 多々見純一、宮崎慎二、脇原徹、米屋勝則、目黒竹司、中野裕美、日本セラミックス協会秋季シンポジウム（愛媛大）（2009）9/16-18 p85.
34. コールドスプレー法により形成したCu膜とAlNセラミック基盤の界面組織解析 中野裕美、山田基宏、福本昌宏、山口英二、日本セラミックス協会秋季シンポジウム（愛媛大）（2009）9/16-18 p103.
35. 浸炭処理と溶融塩法の複合化による硬度傾斜を有するセラミックス被覆層の開発 ○坪田輝一、山根裕介、川端健一、南裕樹、中野裕美、青井芳史、佐々木宗生 日本セラミックス協会秋季シンポジウム(愛媛大)(2009)9/16-18トピックス講演 p96.
36. ZrN/TiN薄膜の積層周期の変化による硬度と微構造の関係 古畑哲、中野裕美、青井芳史 日本セラミックス協会秋季シンポジウム（愛媛大）（2009）9/16-18.p108.
37. 有機誘導体化を利用したTiOClからのγ-Fe_2O_3の合成 塩野岳史、丹藤文彰、菅原義之、中野裕美、先進セラミックス第124委員会 （早稲田大学）（2009）9/11.
38. ナノラメラ構造を有するCo-Cu合金の熱処理によるCu分布変化と界面構造変化の分析電子顕微鏡による解析 中野裕美、湯浅元仁、馬渕守 第25回分析電子顕微鏡討論会（幕張メッセ）（2009） 9/1-2 p 81.
39. 酸化チタン皮膜の大気中高速形成と光触媒特性評価 山田基宏、砂金寛昭、中野裕美、福本昌宏 日本材料学会セラミック材料部門委員会 （京都工芸繊維大）（2009）7/17 p21-22.
40. Li-Nb-Ti系酸化物固溶体に及ぼす希土類元素の効果 林裕之、中野裕美 第26回希土類討論会 札幌コンベンションセンター（2009）5/28 p12-13.
41. 希土類Mn酸化物の層状ペロブスカイト構造特有の一次相転移 中野裕美、石沢伸夫、亀頭直樹 札幌コンベンションセンター(2009）5/28 p14-15.

招待講演

42. 高熱伝導率発現機構解明のための微構造解析 中野裕美・渡利広司 日本セラミックス協会秋季シンポジウム、北海道大学、(2011) 9/9.p116
43. （平成21年度学術賞受賞講演）TEMその場観察による酸化物の微構造解析 中野裕美、日本セラミックス協会2011年年会、静岡大学 (2011)3/16, p65.
44. Rapid synthesis and structure of the M-phase solid solution by millimeter-wave heating H. Nakano et.al *Thermec2011*（ケベック,カナダ）(2011) 8/4.
45. TEMによる魅惑のナノワールド―機能性発現のための微構造解析― 中野裕美、日本セラミックス協会東海支部学術研究発表会（名城大学）(2010)12/18 p96.
46. 機能発現機構解明のための微構造解析ー接合界面の構造ー 中野裕美 溶射技術研究会中部支部 (豊橋技術科学大学）(2010)10/7.
47. ミリ波照射が$LiNbO_3$-TiO_2系固溶体の超構造形成制御に与える影響 中野裕美、佐藤裕久、亀頭直樹、三宅正司、佐治他三郎 EMAP研究会 (大阪大学) (2010) 10/1.
48. Microstructure analysis of AlN ceramics by transmission electron microscopy H. Nakano ***3rd International Symposium on SiAlONs and Non-Oxides***, (カッパドキア,トルコ) (2010) 6/1-4.

受賞

平成 22 年 日本セラミックス協会 第６４回学術賞
「静および動的観察による微構造形成と機能発現機構の解明」中野裕美

グループ関連受賞

平成 23 年日本溶射学会奨励賞
"Synthesis of Titanium Dioxide Powders via Hydrolysis of Titanyl Sulphate for Cold Spray Coating" ○ Noviana Tjitra Salim, 山田基宏, 中野裕美, 福本昌宏、（2010）

平成 23 年日本セラミックス協会秋季シンポジウム若手最優秀ポスター賞
「高速衝突交代セラミックス粒子の金属機材表面への付着挙動」○山田基弘、島幸一郎、M.E.Dicknson,N.T.Salim, 中野裕美、福本昌宏 （2011）

平成 22 年度 日本結晶学会年会 ポスター賞
Imma ペロブスカイト型酸窒化物 LaTiO2N,結晶構造と電子密度分布○齊藤未央・八島正知・中野裕美・高田剛・荻巣清徳・堂免一成（東工大院総理工・豊橋技科大研究基盤セ・

東大院工）（2011）

著書

1. “MICROSTRUCTURAL EVOLUTION BY IN-SITUTEM OBSERVATIONS AND SIMULATIONS” H. Nakano and H. Tanaka, MOMENTUM PRESS (2011) in press
2. “高温 TEM によるセラミック材料の表情の読み取り”「セラミックデータブック (2011 年版」 中野裕美、(株）テクノプラザ発行 （2011）P94-97.

総説、解説等

1. “配向酸化亜鉛セラミックスにおける粒界キャリア散乱” 杵鞭義明・加賀久・中野裕美・田中 諭・植松敬三・多々見純一・渡利広司、セラミックス (2012) in press
2. Review “Microstructural evolution by in-situ TEM observations of oxides” H. Nakano, *J. Ceram. Soc. Jpn.* 119(1) 1-7 (2011).
3. “コールドスプレー法における各種材料皮膜のアプリケーションとセラミックス成膜について”,山田基宏, 中野裕美, 福本昌宏：溶射, 48-2 (2011), 59-63.
4. “コールドスプレー法による光触媒酸化チタン成膜技術の開発” 山田基宏，中野裕美，福本昌宏 セラミックス **46** No.7（2011） 536-540.
5. *セラミックコーティングのブレークスルー*どのように「ブレークスルー」しますか？小野さとみ，中野裕美，明渡純 セラミックス **46** No.7（2011） 529-530.

研究成果の概要

イ希土類酸化物の構造解析と高温 TEM による構造相転移

$(Sr_{0.67}Ln_{0.33})(Mn_{0.33}Ti_{0.67})O_3$ (Ln: rare erath)を Ar 雰囲気下で合成し、単相を得ることができた。La 以外では斜方晶 *Pnma* を有する結晶構造であったが、すでに報告されている Ca 系$(Ca_{0.67}Ln_{0.33})(Mn_{0.33}Ti_{0.67})O_3$とは異なり反射強度が弱く、このことは、Sr のイオン半径が大きくこれによりセルサイズが大きくなたっためである。 また、多くのナノサイズのドメイン形成が観察され、冷却過程内での構造相転移の可能性が示唆された。このため高温 TEM による相転移をその場観察した。一般に、ペロブスカイト酸化物は酸素八面体の傾斜に基づいた結晶構造を有しており、逐次相転移の場合、高温では対称性の高い結晶構造へ相転移を起こすことが知られている。今回のように、電気伝導度データには現れないような微小回転に基づくものについては、高温 TEM による電子回折法の精度の高さを実感した。解析の結果、Ln:Nd, Eu, Gd, Sm について、 *Pnma* から *Imma* への相転移を確認し、相転移温度と希土類のイオン半径、Mn-O 角度、トーレランスファクター（t-因子）と電気伝導度との相関性について議論し今後の新酸化物設計において指針を得ることができた。

ロ希土類系酸化物の低温・短時間合成と物性評価

Li-Nb-Ti-O 系の酸化物については、固溶体はある限られた組成域で、M-相と言われるユニークな周期構造（超構造）を形成する(図１)。この系については、最初にWest が（1984 年）超構造を有することを発見し、2 日がかりで合成した。国内では浦部、中野らがWest とともに国内では最初にこの研究に取り組み、その特異な超構造形成機構解明に取り組んできた。しかし電気炉による合成では、均質な構造にするために 1100℃、24 時間以上を要した。より低い温度で合成できないか？という発想から、24GHz のミリ波炉による実験を開始し、たった１時

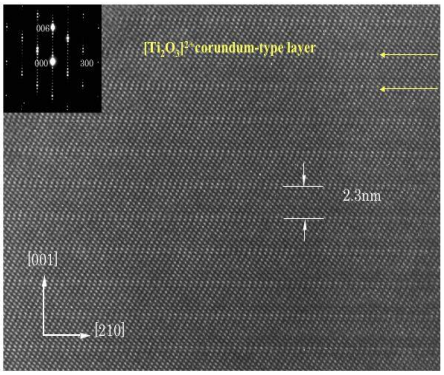

Fig. 1 TEM image of 10-layer structure of $LiNbO_3$-TiO_2 solid solution

間の熱処理で、焼結温度を数百度下げても均質な超構造を形成することを TEM, SEM, XRD 等の複合的分析により明らかにした。また、第一原理計算による構造計算により、この複雑な周期構造が比較的安定であり、このため早い速度でイオン拡散が起こってもこの構造を優先的に形成することがわかった。
また、この特異な構造を利用し、LED 用近紫外励起赤色蛍光体としての可能性を見出した。この蛍光体材料についても、23 年度～ミリ波照射による低温・短時間合成に取り組み、電気炉とほぼ同等の発光特性が得られるような条件を見出した。まだまだ改良の余地があるか、次の研究段階につながる成果であると考えている。

ハ　高温 TEM その場観察によるダイナミクス的考察

層状構造を有するペロブスカイト $BaLn_2Mn_2O_7$ については、構造相転移を利用し、熱処理温度により多彩な構造を有する酸化物の合成が報告され、高温 XRD や電気伝導度、熱分析による相転移が観察され議論がなされてきた。近年著者らは、高温 TEM によるその場観察の結果、これまでに報告例のない一次相転移を高温域で起こすことを見出し, Gd, Pr においてはすでに報告してきた。今回、Eu や Tb について、同様の一次相転移を起こすことをその場観察により明らかにした。この相転移は明らかにペロブスカイト構造で報告されているような、酸素八面体の傾斜による逐次相転移とは性格の異なるものである。最近では、このような層状構造（ペロブスカイト+岩塩構造）がハイブリッド構造として、熱電材料においても高機能発現の場として注目されている。もしハイブリッド構造特有の相転移であれば、Mn 系以外の結晶構造においても同様の相転移が起こる可能性があり、物性との関連性が明らかになれば、興味深い研究材料であると考えている。今回の研究成果を含め、高温 TEM によるダイナミクス的研究に関するこれまでの成果を著書にまとめた。多くの研究者に高温 TEM その場観察による材料解析についての魅力が伝われば幸いである。

二　機能発現メカニズムの解明

この研究に関しては研究者らとの共同研究により遂行し、なぜこのような機能が発現するのか？なぜ思ったような機能にならなかったのか？について、より正確に、ナノスケールからマクロなスケールでの複合的な解析を行った。

その結果、接合（異相）界面に関する研究でいくつかの成果を上げることが

できた。セラミックス基材へ Cu 膜コーティングされた異相界面での解析や、金属基材へ TiO_2 膜コーティングされた異相界面等について、主に TEM による原子レベルでの解析により、これまで不明瞭だったコールドスプレー技術による膜形成機構の解明をすることができた。これらの解析に際し、もっとも苦労したのは、TEM 観察用の断面薄片試料の作成技術である。異材で形成された材料であったため、きれいな薄片試料が作製できるまでに試行錯誤して２か月間を費やしたが、結果として多くの新知見を得ることができた。この実験であらためて TEM 用の観察試料作製の重要性を実感した。

希土類酸化物の合成と評価に関連する研究成果

Journal of the Ceramic Society of Japan 119 [11] 808-812 2011 Paper

Rapid synthesis and structural analysis of Li–Nb–Ti–O solid solutions with superstructure by millimeter-wave heating

Hiromi NAKANO,† Tasaburo SAJI,* Motohiro YUASA, Syoji MIYAKE* and Mamoru MABUCHI****

Toyohashi University of Technology, Tempaku, Toyohashi 441–8580
***MSP Corp., Takaitanaka, Higashi-Osaka 577–0065**
****Kyoto University, Yoshidahonmachi, Sakyo-ku, Kyoto 606–8501**

We have succeeded in synthesizing $Li_{1+x-y}Nb_{1-x-3y}Ti_{x+4y}O_3$ solid solutions ($0.11 \leq x \leq 0.18$, $0 \leq y \leq 0.09$) having a superstructure by millimeter-wave heating for only 1 h. Synthesizing temperatures were attempted in the range from 873 to 1273 K. A homogeneous LNT solid solution with a superstructure was formed above 1173 K. Such LNT solid solutions were characterized using X-ray diffraction, a scanning electron microscope, and a transmission electron microscope (TEM) from micro-scale to nano-scale. Element analysis revealed that the superstructure was formed by periodical insertion of intergrowth layers with a high concentration of Ti ions. The structural stability of the LNT solid solution was estimated by a first-principles calculation. The results revealed that the structure was stable due to the formation of the superstructure, which is composed through an anisotropic arrangement of the Ti ions.

Key-words : Millimeter-wave heating, Li–Nb–Ti–O solid solution, Superstructure, Transmission electron microscopy (TEM)

[Received June 9, 2011; Accepted July 22, 2011]

1. Introduction

In the Li_2O–Nb_2O_5–TiO_2 system, $Li_{1+x-y}Nb_{1-x-3y}Ti_{x+4y}O_3$ ($0.11 \leq x \leq 0.33$, $0 \leq y \leq 0.09$) (LNT) forms with a superstructure, and this is known as the M-phase. Since the discovery of the M-phase by Castrejon et al.,[1),2)] such structures have been investigated.[3)–6)] The superstructure of the M-phase is formed by periodical insertion of an intergrowth layer in a matrix having a trigonal structure. The relationship between the dielectric properties and the period of the M-phase's intergrowth layer has been studied.[7),8)] Yamamoto et al. synthesized an anisotropy structure of an M-phase solid solution in which rod-precipitates were arranged regularly by a crystal growth method.[9)] Recently, an Eu-doped LNT solid solution has been developed as a new photoluminescence material.[10)] The synthesis of a homogeneous M-phase, however, required treatment at 1373 K for 24 h, after calcination at 1273 K for 3 h, in an electric furnace. Accordingly, a fast synthesizing technique that uses lower energy is required for practical application of this material.

Heating by millimeter-wave radiation has certain advantages in industrial processes or applications from the viewpoints of the homogeneity of large materials, control of grain growth, and densification at low temperature.[11),12)] Millimeter-wave frequency is typically over 30 GHz (<10 mm), but in this paper, a frequency of 24 GHz is considered. High-density Si_3N_4 or AlN ceramics, which are not easily sintered ceramics, could be synthesized using suitable additives by millimeter-wave heating at lower temperatures and shorter times than with a conventional sintering method.[13),14)] Recently, we have characterized the relationship between the microstructure and bending strength of alumina ceramics synthesized by millimeter-wave heating. The results revealed that a higher boundary velocity (V_b) than pore velocity (V_p) caused nanometer-sized pores to remain in the grains, where rapid diffusion of atoms occurred in the electromagnetic field.[15)]

In the present study, we were the first to succeed in synthesizing M-phase $Li_{1+x-y}Nb_{1-x-3y}Ti_{x+4y}O_3$ solid solutions ($0.11 \leq x \leq 0.18$, $0 \leq y \leq 0.09$) by millimeter-wave heating for only 1 h. Synthesizing temperatures were attempted in the range from 873 to 1273 K. Structural analysis of the LNT solid solutions was performed carefully using X-ray diffraction, a scanning electron microscope, and a transmission electron microscope (TEM) from micro-scale to nano-scale. The structural stability of the LNT solid solution was estimated by a first-principles calculation. As discussed below, this was done because a stable M-phase could be synthesized quickly and homogeneously by the millimeter-wave radiation.

2. Experimental procedure

The starting materials used were Li_2CO_3, Nb_2O_5 and TiO_2 (>99.9% grade) to prepare the solid solution of LNT. The compositions of the LNT solid solutions prepared in this work followed the general formula $Li_{1+x-y}Nb_{1-x-3y}Ti_{x+4y}O_3$, with $0.11 \leq x \leq 0.18$, $0 \leq y \leq 0.09$. The TiO_2 content of the specimens was varied from 15 to 35 mol %. The powders were mixed and pressed in air at various temperatures from 873 to 1273 K for 1 h by millimeter-wave heating. The millimeter-wave heating equipment consists of a 24-GHz gyrotron millimeter-wave generator and a multi-mode chamber (MSP Corp., Japan). The heating rate was approximately 30 K/min, and the specimen was cooled down in the chamber after sintering.

Structural analysis was carried out by X-ray diffraction (XRD) using a RINT 2500 (Rigaku Co., Ltd., Japan) operating at 40 kV and 200 mA. The angles were corrected by an external standard method for calculation of the lattice parameters. Microstructure images were observed with a scanning electron microscope (SEM) (SU8000, Hitachi Co., Ltd., Japan) operating at 3 kV. High-resolution TEM (HRTEM) images and selected area

† Corresponding author: H. Nakano; E-mail: hiromi@crfc.tut.ac.jp

electron diffraction (SAED) patterns were also observed by a device (2100 F, JEOL Co., Ltd., Japan) operating at 200 kV and equipped with energy-dispersed spectroscopy (EDS).

First-principles calculations were carried out in the Cambridge Serial Total Energy Package (CASTEP),[16] in which the density functional theory[17),18] was used with a plane wave basis set. The exchange correlation interactions were treated using the spin-polarized version of the generalized gradient approximation within the scheme of Perdew Burke Ernzerhof.[19] The ultrasoft pseudopotentials[20] represented in reciprocal space were used for all elements in the calculations. The wave functions were expanded to the plane wave basis set with an energy cutoff of 400 eV. The Brillouin zone was sampled using a Monkhorst-Pack $5 \times 2 \times 1$ k-point mesh. All atomic positions were fully relaxed until the Hellmann Feynman force on each atom was reduced to within 0.01 eV/Å.

3. Results and discussion

Two types of LNT solid solutions were prepared, one with calcination at 1073 K for 5 h in an electric furnace and the other without calcination. Then, these specimens were synthesized at 1273 K for 1 h by millimeter-wave heating. These structures were analyzed by XRD, and no secondary phases were observed in either of them. **Figure 1** shows XRD patterns of LNT solid solutions with various Ti content at 1273 K for 1 h without calcination. Satellite reflections were detected around 012, 202 and $\bar{1}32$ reflections of the $LiNbO_3$ cell, which were caused by the superstructure formed by the LNT solid solution. The periods of the satellite reflections in the XRD pattern increased with increasing Ti content. To confirm the effect of the millimeter-wave heating, the LNT solid solutions were also synthesized in the electric furnace at 1273 K for 1 h. **Figure 2** shows XRD patterns and SEM images of LNT solid solution with Ti 20 mol % by millimeter-wave heating and by heating with an electric furnace. In the case of using the electric furnace for heating, the intensities of satellite reflections were lower and the peaks were broader than those found for millimeter-wave heating; the SEM image shows that the grain size is clearly 1/10 the size of that obtained by millimeter-wave heating. The changes in the lattice constants of the LNT solid solutions were calculated as shown in **Fig. 3**. In Fig. 3(a), the lattice constants were in good agreement between LNT solid solutions with calcination and those without calcination. The results show that the LNT solid solution with a superstructure was formed quickly and homogeneously by millimeter-wave heating even without calcination. On the other hand, Fig. 3(c) shows the lattice constants of the specimens

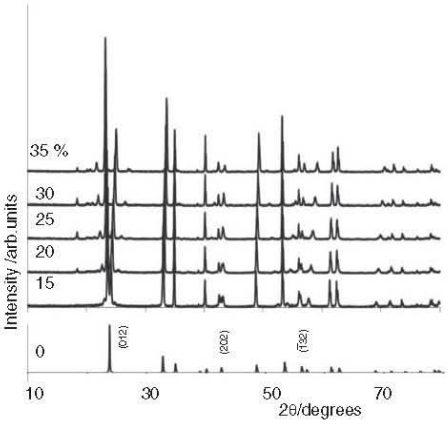

Fig. 1. XRD patterns of LNT solid solutions with various Ti content at 1273 K for 1 h. Note that the indices are based on the $LiNbO_3$ structure.

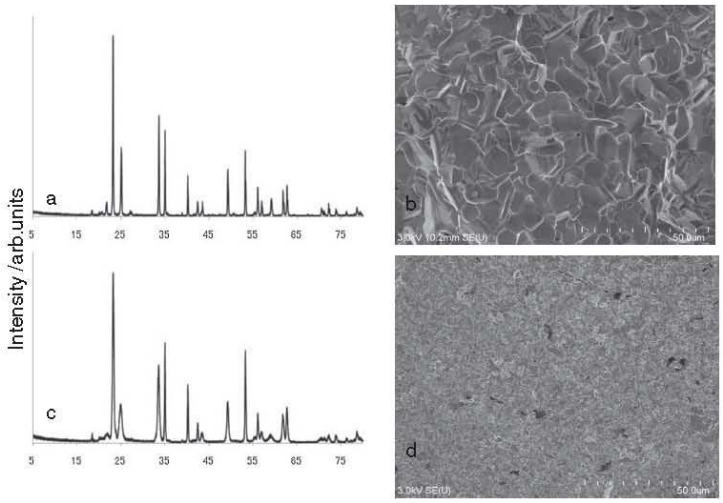

Fig. 2. XRD patterns and SEM images of LNT solid solutions with Ti 20 mol %. Millimeter-wave heating in (a) and (b), electric-furnace heating in (c) and (d) at 1273 K for 1 h.

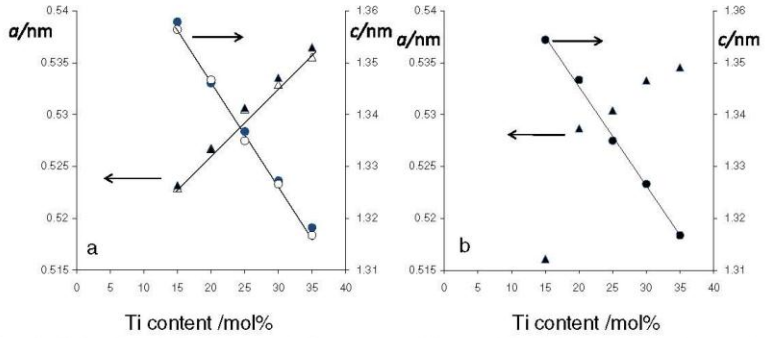

Fig. 3. (Color online) Relationship between lattice constants and Ti content. Black-filled circles or triangles are oxides without calcination. Millimeter-wave heating in (a) and electric-furnace heating in (b) at 1273 K for 1 h.

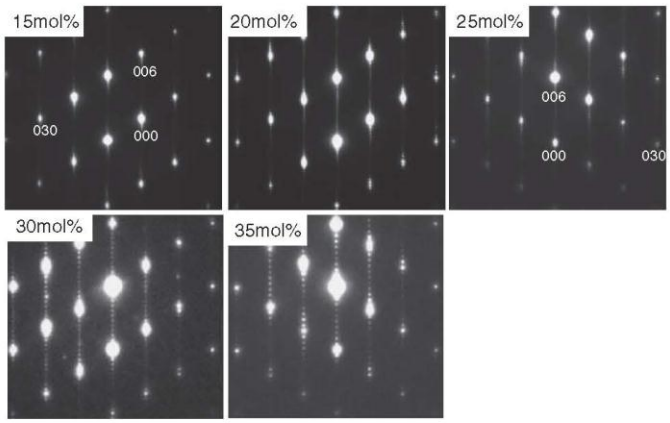

Fig. 4. SAED patterns of LNT solid solutions taken from [100] or [$\bar{1}$00] zone axis with Ti content of 15, 20, 25, 30, 35 mol %.

synthesized in the electric furnace. The slope of the change in the *c*-parameters in Fig. 3(c) was in agreement with that of millimeter-wave heating in Fig. 3(a), but the trends of the *a*-parameters varied widely. This means that the solid solution was synthesized for a short time even in the electric furnace, but it is expected that the superstructure would be formed during the grain growth process for a longer time. The grain shapes clearly changed from spherical to plate-like, as seen in Fig. 2(b).

Next, we analyzed the superstructure of the LNT solid solutions by an electron diffraction method. **Figure 4** shows the SAED patterns of LNT solid solutions synthesized by millimeter-wave heating at 1273 K with various Ti content taken from the [100] or [$\bar{1}$00] zone axis. The super-lattice reflections were detected between fundamental reflections along the *c*-direction. Our results showed that the number of satellite reflections decreased by 31, 23, 19, 13, and 11 times, relative to the (006) spacing, for Ti contents of 15, 20, 25, 30, and 35 mol %, respectively; accordingly, the change in the layers' spacing decreased as the Ti content increased. The periodicities were in good agreement with that of the LNT solid solution synthesized in the electric furnace at 1373 K for 24 h.[21] The periodicities

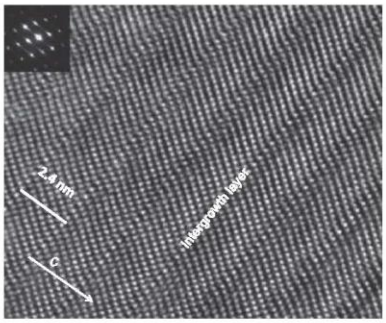

Fig. 5. HRTEM image of LNT solid solution with Ti 35 mol %.

hardly increased with increasing Ti content above 40 mol % in the previous examinations.[21] **Figure 5** shows an HRTEM image of the LNT solid solution with Ti 35 mol % synthesized by

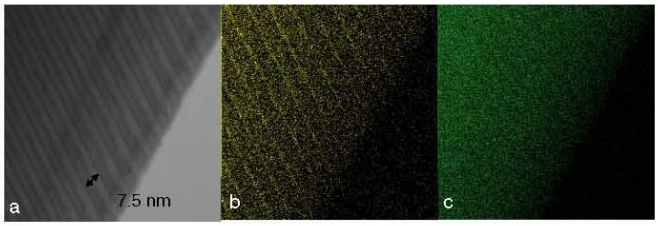

Fig. 6. (Color online) STEM image of LNT solid solution with 15 mol % in (a), Ti mapping image in (b), and Nb mapping image in (c).

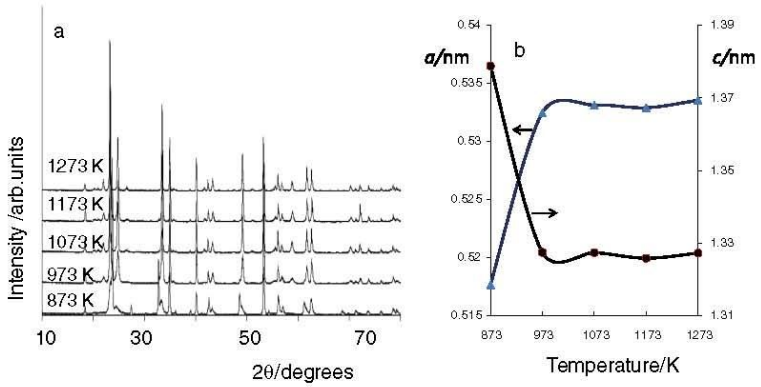

Fig. 7. (Color online) XRD patterns of LNT solid solution with Ti content of 30 mol % in (a) and changes in lattice constants in (b) at various temperatures for 1 h.

millimeter-wave heating. The intergrowth layer inserted periodically in the $LiNbO_3$-like sub-cell showed a value 11 times that of (006) spacing. The intergrowth layer seemed to be composed of a single atomic layer with different contrast, as seen in the HRTEM image of a 10-layer M-phase composition.[6)]

We compared atomic-scale Ti concentration between sites at the intergrowth layer and at the matrix by EDS analysis. **Figure 6** shows a STEM image of the LNT solid solution with Ti 15 mol % in (a), Ti mapping image in (b), and Nb mapping image in (c). In Fig. 6(a), dark contrasts were observed between intergrowth layers, which might be caused by the strain due to insertion of the intergrowth layer. Mapping images were successfully obtained, and these showed that Ti ions were distributed with higher concentration at the intergrowth layers. In other words, the superstructure of the LNT solid solution was composed through an anisotropic arrangement of the Ti ions of rock-salt-type Li_2TiO_3.[5)]

In order to understand the effect of the millimeter-wave irradiation, synthesizing temperatures were attempted in the range from 873 to 1273 K. **Figure 7** shows XRD patterns in (a) and lattice constants in (b) of the LNT solid solutions with Ti 30 mol % at various temperatures. The satellite reflections were detected even at 973 K, but the intensity of the satellite reflections became lower with decreasing temperature. This means that the period of the superstructure was not formed homogeneously. At 873 K, the LNT solid solution did not form because the secondary phase was detected as a TiO_2 phase around 28 degrees and the lattice constants were nearly equal to that of $LiNbO_3$. The period of the superstructure was confirmed precisely by the SAED pattern and HRTEM image. The results show that homogeneous M-phases were formed with a superstructure above 1173 K. **Figure 8** shows an HRTEM image and SAED pattern of the LNT solid solution with Ti 30 mol % at 1073 K for 1h. The image

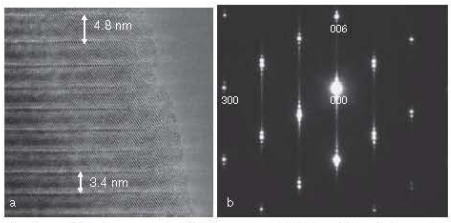

Fig. 8. TEM image and SAED pattern of LNT solid solution with Ti content of 30 mol % at 1073 K for 1 h.

shows that the period of the intergrowth layer had various periodicities with slightly different width along the c-direction. In the SAED pattern, weak streaks along the c-axis were also observed, indicating an inhomogeneous period of the intergrowth layer. At 873 K, almost all grains have no superstructure, but a few grains have a superstructure in which their periods are inhomogeneous.

Why did the anisotropic structure form quickly by millimeter-wave heating? We focused the distribution of Ti ions in the LNT solid solutions because Ti ions were distributed with higher concentration at the intergrowth layer, as shown in the mapping data (Fig. 6). In order to investigate the structural stability, two types of their cells were used and compared: One involved an anisotropic distribution of Ti ions in the cell, in other words, a rich distribution of Ti ions at the intergrowth layer (Ti-rich model), and the other had a poor distribution of Ti ions at the intergrowth layer (Ti-poor model). The structural stability of the LNT solid solution was estimated by a first-principles calculation. The simulation cells were constructed based on the crystallographic data for a 10-layer LNT solid solution with a lattice constant of $a = b = 0.510\,\mathrm{nm}$ and $c = 2.319\,\mathrm{nm}$.[6] The initial cell size was $0.510 \times 1.531 \times 2.319\,\mathrm{nm}^3$ to fulfill stoichiometry. Periodic boundary conditions were applied in all three directions. The stabilities of the LNT solid solutions are discussed in terms of the cohesive energy, E_{coh}, defined by Eq. (1):

$$E_{\mathrm{coh}} = \left(E_{\mathrm{tot}} - \sum_{\beta} n_{\beta} E_{\beta}\right) \Big/ \sum_{\beta} n_{\beta} \qquad (1)$$

where E_{tot} is total energy of the cell of the LNT solid solution model, E_{β} is the energy of isolated β atoms (or ions) (β = Li, Nb, Ti, O) in the cell, and n_{β} is the number of β atoms. The values of the cohesive energy calculated from the isolated atoms were $-6.60\,\mathrm{eV/atom}$ for the Ti-poor model and $-6.65\,\mathrm{eV/atom}$ for the Ti-rich model. In cases where the cohesive energy was calculated from the ions, the values were $-178.41\,\mathrm{eV/atom}$ for the Ti-poor model and $-178.47\,\mathrm{eV/atom}$ for the Ti-rich model. Therefore, the structural stability of the Ti-rich model was higher regardless of the calculation method used for the cohesive energy, and the difference between these cohesive energies was significant for the structural stability.[22] The results reveal that the structure is stable due to the formation of the superstructure, which is composed through an anisotropic arrangement of the Ti ions. At the experimental stage, the relationship between the structural stability and the effect of the millimeter-wave irradiation is not clear. Actually, a stable M-phase could be synthesized during grain growth even for a short heating time by using millimeter-wave heating.

4. Conclusions

We aimed to synthesize the Li–Nb–Ti–O solid solution having a superstructure, known as the M-phase, quickly and homogeneously by millimeter-wave heating. Synthesizing temperatures were attempted in the range from 873 to 1273 K. As a result, we were the first to successfully synthesize $Li_{1+x-y}Nb_{1-x-3y}Ti_{x+4y}O_3$ solid solutions ($0.11 \le x \le 0.18$, $0 \le y \le 0.09$) with a superstructure for only 1 h above 1173 K. The LNT solid solutions were characterized, from micro-scale to nano-scale, using X-ray diffraction, a scanning electron microscope, and a transmission electron microscope (TEM). The changes in the lattice constants revealed that the LNT solid solution began to form even in an electric furnace at 1273 K for 1 h. However, it is expected that the superstructure would be formed during the grain growth process over a long time. On the other hand, the LNT solid solution synthesized by millimeter-wave heating had a homogeneous superstructure after only 1 h, and the grain sizes became significantly larger. Element analysis revealed that the superstructure was formed by periodical insertion of intergrowth layers with higher concentration of Ti ions than at the matrix. The structural stability of the LNT solid solution was estimated by a first-principles calculation. The results revealed that the structure was stable due to the formation of the superstructure, which is composed through an anisotropic arrangement of the Ti ions.

Acknowledgements This work was partially supported by a Grant-in-Aid for Scientific Research (c) No. 21560704 (H. N.) by the Japan Society for the Promotion of Science and by the Kazuchika Okura Memorial Foundation (2010).

References

1) M. E. Villafuerte-Castrejon, J. A. Gracia, E. Cisneros, R. Valenzuela and A. R. West, *Trans. J. Brit. Ceram. Soc*, **83**, 143–145 (1984).
2) M. E. Villafuerte-Castrejon, A. Aragon-Pina, R. Valenzuela and A. R. West, *J. Solid State Chem.*, **71**, 103–108 (1987).
3) R. I. Smith and A. R. West, *Mater. Res. Bull.*, **27**, 277–285 (1992).
4) H. Hayashi, H. Nakano, K. Suzumura, K. Urabe and A. R. West, *Forth Ceram. Soc*, **2**, 391–398 (1995).
5) H. Hayashi, K. Urabe and K. Niihara, *Key Eng. Mater.*, **161–163**, 501–504 (1999).
6) L. Farber, I. Levin, A. Borisevichi, I. E. Grey, R. S. Roth and P. K. Davies, *J. Solid State Chem.*, **166**, 81–90 (2002).
7) A. Y. Borisevich and P. K. Davies, *J. Am. Ceram. Soc.*, **85**, 573–578 (2002).
8) Y. Yamamoto, H. Hayashi, T. Sekino, T. Nakayama, T. Kondo, M. Wada, T. Adachi and K. Niihara, *Mater. Res. Innovations*, **7**, 74–79 (2003).
9) Y. Yamamoto, T. Sekino, T. Kusunose, T. Nakayama, Y. Morimoto, S. Miyazawa and K. Niihara, *J. Cryst. Growth*, **264**, 445–451 (2004).
10) H. Hayashi, H. Nakano and M. I. Jones, *J. Ceram. Soc. Japan*, **118**, 226–230 (2010).
11) Y. Makino, *ISI International*, **47**, 539–544 (2007).
12) Y. Makino and S. Miyake, *J. High. Temp.*, **29**, 3–12 (2003) [in Japanese].
13) H. Yoshioka, Y. Makino, S. Miyake and H. Mori, *J. Alloys Compd.*, **408–412**, 905–909 (2002).
14) H. Park and H. Kim, *J. Am. Ceram. Soc.*, **80**, 750–756 (1997).
15) H. Nakano, H. Nakano, Y. Makino and S. Sano, *J. Alloys Compd.*, **547**, 485–489 (2008).
16) M. C. Payne, M. P. Teter, D. C. Allan, T. A. Arias and J. D. Joannopoulos, *Rev. Mod. Phys.*, **64**, 1045–1097 (1992).
17) P. Hohenberg and W. Kohn, *Phys. Rev.*, **136**, B864–B871 (1964).
18) W. Kohn and L. Sham, *Phys. Rev.*, **140**, A1133–A1138 (1965).
19) J. P. Perdew, K. Burke and M. Ernzerhof, *Phys. Rev. Lett.*, **77**, 3865–3868 (1996).
20) D. Vanderbilt, *Phys. Rev. B*, **41**, 7892–7895 (1990).
21) D. Seki, T. Sirakami, Y. Tsuchida and K. Urabe, Proc. Fall Meeting of Ceramic Society of Jpn., 2002F (2002) p. 124 [in Japanese].
22) W. Y. Yu, N. Wang, X. B. Xiao, B. Y. Tang, L. M. Peng and W. J. Ding, *Solid State Sci.*, **11**, 1400–1407 (2009).

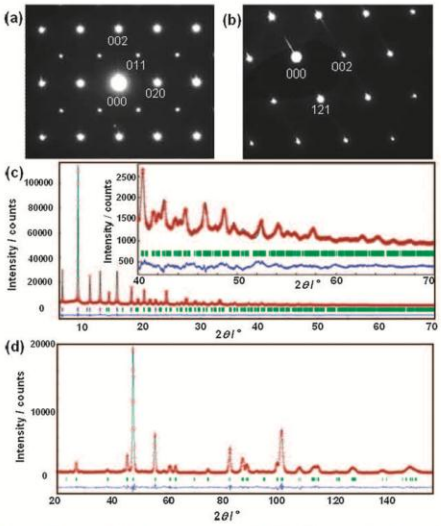

Fig. 1 Electron diffraction patterns of $LaTiO_2N$ for (a) [100] and (b) [2$\bar{1}$0] zone axes. Rietveld patterns of (c) synchrotron and (d) neutron data of $LaTiO_2N$. Inset in (c) is an enlargement of higher 2θ region. Reflections in (a) and (b) are indexed based on the *Imma* lattice. The *Imma* 011 reflections in (a) are forbidden for the $R\bar{3}c$ structure.

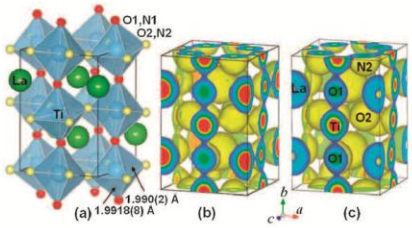

Fig. 2 (a) Refined crystal structure and (b) isosurface of MEM electron density at 0.5 $Å^{-3}$ of *Imma* $LaTiO_2N$. (c) Isosurface of DFT valence electron density at 0.5 $Å^{-3}$ of 4th model of $(LaTiO_2N)_4$. These figures were drawn with a computer program VESTA.[18]

To validate the *Imma* structural model and to evaluate the electronic states of $LaTiO_2N$, we optimized the crystal structure of $(LaTiO_2N)_4$, based on the Density Functional Theory (DFT). Six local structure models of the O and N atomic arrangements around Ti atom were investigated in the DFT structural optimization (See (S9) in ESI†). These calculations were performed with the initial crystallographic parameters based on the *Imma*, $P\bar{1}$ and $R\bar{3}c$ refinements using the present diffraction data. As shown in Table S3 of (S10) in ESI†, the ground state was obtained for the *Imma* structure model (4th model in Fig. S7(d) of (S9) in ESI†). Optimized unit-cell and positional parameters for the 4th model agreed well with the experimental ones ((S11) in ESI†).

Table 1 Crystallographic parameters and reliability factors in Rietveld and MPF analyses for the neutron powder diffraction data of $LaTiO_2N$[a]

Atom	Site	g	x	y	z	U/Å^2
La	4*e*	1.00(3)	0	1/4	0.9970(8)	0.0067(9)
Ti	4*b*	1	0	0	1/2	0.003(2)
O1	4*e*	0.67(4)	0	1/4	0.5623(6)	0.0138(5)
N1	4*e*	0.33(4)[b]	0	1/4	= x(O1)	= U(O1)
O2	8*g*	0.67(4)	1/4	0.0322(3)	1/4	= U(O1)
N2	8*g*	0.33(4)[b]	1/4	= y(O2)	1/4	= U(O1)

[a] Crystal symmetry: Orthorhombic; Space group: *Imma*; Unit-cell parameters: a = 5.5731(2), b = 7.8708(3), c = 5.6072(2) Å, $\alpha = \beta = \gamma = 90°$; Reliability factors in Rietveld analysis: R_{wp} = 5.08%, R_I = 4.01%, R_F = 2.49%, S = 1.70; Reliability factors in 1st MPF analysis: R_I = 2.36%, R_F = 1.42%. The decrease of R_I and R_F from the Rietveld analysis to MPF one indicates the validity of the MEM nuclear density. The nuclear density is consistent with the refined structure (See Fig. S6(b) of (S8) in ESI). [b] Refinements of occupancy factors: g(X): Occupancy factor of X atom. In preliminary refinements, the occupancy factors at the anion sites satisfied the relations, g(O1) + g(N1) = 1 and g(O2) + g(N2) = 1 within the 3σ where σ is the estimated standard deviation, thus the anion occupancies were analyzed using the constraints: g(O1) + g(N1) = 1 and g(O2) + g(N2) = 1 in the final refinement.

Fig. 2b, 3b and 4b show the MEM experimental electron densities of $LaTiO_2N$, while the Fig. 2c, 3c and 4c show the DFT theoretical valence electron densities of optimized $(LaTiO_2N)_4$, which are consistent with each other. Both experimental and theoretical electron density maps clearly show that the Ti–(O,N) bond is covalent, while the La atom is more ionic. The minimum electron density (MED) at the Ti–(O,N) bond (0.56 $Å^3$) agree with theoretical ones (0.38–0.87 $Å^3$, average value = 0.62 $Å^3$). The covalent bonding is formed by the overlap of (N 2p, O 2p) and Ti 3d orbitals (Fig. 5). The DFT calculations indicate that the Ti–N bond length (1.94(5) Å) is shorter than the Ti–O one (2.07(9) Å) and that the covalency of Ti–N bond (average MED = 0.78 $Å^3$) is higher than that of Ti–O bond (average MED = 0.52 $Å^3$). The top of the valence band is mainly composed of the N 2p orbital, while the Ti 3d orbital forms the bottom of the conduction band. The estimated band gap (1.30 eV; Fig. 5; (S10) and (S12) in ESI†) is a little lower than the experimental value (2.1 eV)[3], which is usual in the DFT calculations. The covalent bonding and the existence of N atoms are responsible for the reduced band gap of $LaTiO_2N$, which lead to the visible-light response of the $LaTiO_2N$ photocatalyst.

In summary we have presented here the first example of the *Imma* perovskite-type oxynitride. $LaTiO_2N$ was determined to have the *Imma* perovskite-type structure with $a^0b\ b$ tilt system by the Rietveld analysis of high-resolution synchrotron and neutron powder diffractometry, and transmission electron microscopy. The refined crystallographic parameters agree well with ones of the optimized structure obtained by Density Functional Theory calculations. Experimental and theoretical electron densities indicate the covalent bonding between Ti cation and N,O anions. The DFT calculations indicate that the Ti–N bond length is shorter than the Ti–O one and that the covalency of Ti–N bond is higher than that of Ti–O bond. The top of the valence band is mainly composed of the N 2p orbital, while the Ti 3d orbital forms the bottom of the

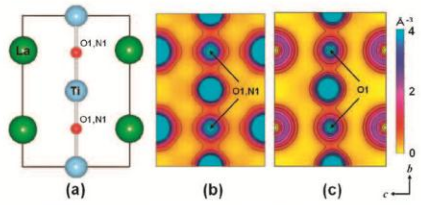

Fig. 3 (a) Refined crystal structure, (b) MEM electron-density and (c) DFT valence-electron-density distributions on the *bc* plane of $LaTiO_2N$ at $x = 0$. Contours from 0.4 to 4.0 $Å^{-3}$ (Step = 0.4 $Å^{-3}$). Fig. (c) was obtained by the DFT calculations for the 4th structure model (Fig. S7(d) of (S9) in ESI†).

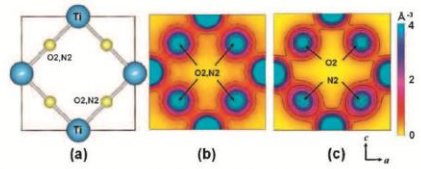

Fig. 4 (a) Refined crystal structure, (b) MEM electron-density and (c) DFT valence-electron-density distributions on the *ac* plane of $LaTiO_2N$ at $y = 0$. Contours from 0.4 to 4.0 $Å^{-3}$ (Step = 0.4 $Å^{-3}$). Fig. (c) was obtained by the DFT calculations for the 4th structure model (Fig. S7(d) of (S9) in ESI†).

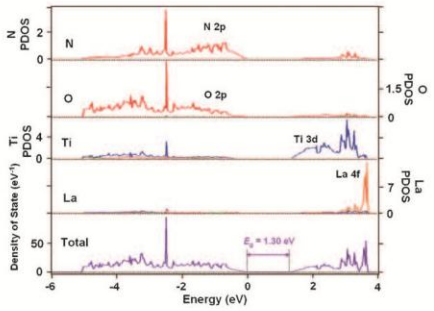

Fig. 5 Total and partial density of states of $LaTiO_2N$ obtained by the DFT calculations for the 4th structure model (Fig. S7(d) of (S9) in ESI†). Green, red, blue and orange lines stand for partial density of states of s, p, d and f orbitals, respectively. Purple line denotes the total density of states.

conduction band. The covalent bonding and existence of N atoms are responsible for the reduced band gap, which lead to the visible-light response of $LaTiO_2N$ photocatalyst. These findings will be useful to design and develop the oxynitride materials.

We thank Mr H. Yamada, Dr J. Kim, Mr K. Nemoto, Prof. K. Ohoyama, Dr T. Wakita, Mr T. Takizawa and Mr K. Kawachi for assistance. This work was partially supported by the Ministry of Education, Science, Sports and Culture, Grant-in-Aid for Scientific Research (B).

Notes and references

‡ Synchrotron X-ray powder diffraction measurements of $LaTiO_2N$ were performed at 29.5 °C on a Debye-Scherrer camera with an imaging plate as a detector installed at BL02B2 experimental station of the SPring-8, Hyogo Japan.[14] We utilized a monochromatized X-ray with a short wavelength of 0.44311 Å, which enables high-resolution measurements of 0.386 Å. Neutron powder diffraction data of $LaTiO_2N$ were measured by the diffractometer HERMES[15] with a 1.84885 Å neutron beam. Synchrotron and neutron diffraction data were analyzed by a combination technique[16,17] of Rietveld analysis, the maximum-entropy method (MEM), and MEM-based pattern fitting (MPF). A program RIETAN-FP[16] was utilized for the Rietveld analysis and MPF. MEM calculation was done with PRIMA program.[17] Structure and density distribution were drawn with VESTA program.[18]

1 (*a*) V. I. Pârvulescu, P. Grange and B. Delmon, *Catal. Today*, 1998, **46**, 233–316; (*b*) M. A. Peña and J. L. G. Fierro, *Chem. Rev.*, 2001, **101**, 1981–2017; (*c*) *Perovskite Oxide for Solid Oxide Fuel Cells*, ed. T. Ishihara, Springer Pub. Co., NY, 2009; (*d*) K.-I. Kobayashi, T. Kimura, H. Sawada, K. Terakura and Y. Tokura, *Nature*, 1998, **395**, 677–680.
2 M. W. Lufaso and P. M. Woodward, *Acta Crystallogr., Sect. B: Struct. Sci.*, 2001, **57**, 725–738.
3 (*a*) A. Kasahara, K. Nukumizu, G. Hitoki, T. Takata, J. N. Kondo, M. Hara, H. Kobayashi and K. Domen, *J. Phys. Chem. A*, 2002, **106**, 6750–6753; (*b*) A. Kasahara, K. Nukumizu, T. Takata, J. N. Kondo, M. Hara, H. Kobayashi and K. Domen, *J. Phys. Chem. B*, 2003, **107**, 791–797.
4 Y.-I. Kim and P. M. Woodward, *J. Solid State Chem.*, 2007, **180**, 3224–3233.
5 D. Logvinovich, L. Bocher, D. Sheptyakov, R. Figi, S. G. Ebbinghaus, R. Aguiar, M. H. Aguirre, A. Reller and A. Weidenkaff, *Solid State Sci.*, 2009, **11**, 1513–1519.
6 M. Jansen and H. P. Letschert, *Nature*, 2000, **404**, 980–982.
7 Y. Horibe, J.-S. Ahn, P. A. Sharma, S. Mori, C.-H. Chen, S.-J. Oh and S.-W. Cheong, *J. Phys. Soc. Jpn.*, 2009, **78**, 044704.
8 C. J. Howard, K. S. Knight, B. J. Kennedy and E. H. Kisi, *J. Phys.: Condens. Matter*, 2000, **12**, L677–L683.
9 T. Moriga, K. Ikeuchi, R. Mashima, D. Aoki and K.-I. Murai, *J. Ceram. Soc. Jpn.*, 2007, **115**, 637–639.
10 F. Tessier and R. Marchand, *J. Solid State Chem.*, 2003, **171**, 143–151.
11 S. J. Clarke, B. P. Guinot, C. W. Michie, M. J. C. Calmont and M. J. Rosseinsky, *Chem. Mater.*, 2002, **14**, 288–294.
12 (*a*) M. Yashima, Y. Lee and K. Domen, *Chem. Mater.*, 2007, **19**, 588–593; (*b*) M. Yashima, K. Ogisu and K. Domen, *Acta Crystallogr., Sect. B: Struct. Sci.*, 2008, **64**, 291–298.
13 N. E. Brese and M. O'Keeffe, *Acta Crystallogr., Sect. B: Struct. Sci.*, 1991, **47**, 192–197.
14 E. Nishibori, M. Takata, K. Kato, M. Sakata, Y. Kubota, S. Aoyagi, Y. Kuroiwa, M. Yamakata and N. Ikeda, *Nucl. Instrum. Methods Phys. Res., Sect. A*, 2001, **467–468**, 1045–1048.
15 K. Ohoyama, T. Kanouchi, K. Nemoto, M. Ohashi, T. Kajitani and Y. Yamaguchi, *Jpn. J. Appl. Phys.*, 1998, **37**, 3319–3326.
16 F. Izumi and R. A. Dilanian, *Recent Res. Develop. Phys.*, 2002, **3**, 699–726.
17 F. Izumi and K. Momma, *Solid State Phenom.*, 2007, **130**, 15–20.
18 K. Momma and F. Izumi, *J. Appl. Crystallogr.*, 2008, **41**, 653–658.

Crystal structure and phase transition of $(Sr_{0.67}Ln_{0.33})(Mn_{0.33}Ti_{0.67})O_3$ (Ln: Nd, Sm, Eu, Gd)

Hiromi Nakano[1], Koichiro Fukuda[2], Migaku Kobayashi[3], Naoki Kamegashira[1]

1: Toyohashi University of Technology
Toyohashi, Japan
hiromi@crfc.tut.ac.jp

2: Nagoya institute of Technology
Nagoya, Japan

3: Numazu College of Technology
Numazu, Japan

Corresponding author:nkamegas@kktci.co.jp

Abstract

Perovskiet oxides, $(Sr_{0.67}Ln_{0.33})(Mn_{0.33}Ti_{0.67})O_3$ (Ln: Nd, Sm, Eu, Gd), are synthesized at 1573 K in an Ar flow. These crystal structures are determined to be orthorhombic structures with a space group of *Pnma* (No. 62) by X-ray diffraction and electron diffraction methods. The transmission electron microscope (TEM) images reveal nano-domains formed by the phase transition. The phase transition is observed in-situ using a high-temperature TEM. High-temperature phases of these Sr-Ln oxides possess an orthorhombic structure with a space group of *Imma* (No. 74). The phase transition represents a structural change from the three-tilt system to a two-tilt system that is controlled by the tilting of an $(Mn,Ti)O_6$ octahedron. The transition temperatures are related to the rare earth ion's radius and distortion of the octahedron.

Keywords: Perovskite, Crystal structure, XRD, electron diffraction, high-temperature TEM

Introduction

Rare-earth manganese perovskites ($LnMnO_3$, Ln = rare-earth) and their related compounds exhibit interesting electrical, magnetic and optical properties [1,2]. They are best known for their excellent magneto-resistance characteristics [3-5]. For the appearance of useful properties in perovskite systems, various oxides are formed by the combination of the A-site ion or the B-site ion with different valences and ionic sizes. In such a partial-substitution oxide, the shape and tilt of the MnO_6 octahedron depend on the rare-earth species at the A-site [6,7]. Oxides with a combination of Mn and Ti ions at the B-sites were synthesized under various atmospheres by varying the oxidation states of these ions. The Ln_2MnTiO_6 (Ln = rare-earth) phase was synthesized in a reducing atmosphere, and it had an orthorhombic structure (*Pnma*) for Ln = La-Nd, a monoclinic structure (*P*121/*n*1) for Ln = Sm-Gd, and a hexagonal structure (*P*63*cm*) for Yb [8-12]. The authors have synthesized oxides with various structures in an Ar flow, including $(Ca_{0.5}Ln_{0.5})(Mn_{0.5}Ti_{0.5})O_3$ (Ln = La-Yb) and $(Ca_{0.67}Ln_{0.3})(Mn_{0.33}Ti_{0.67})$ (Ln = La, Nd, Sm, Eu) with orthorhombic structures (*Pnma*) [13, 14]. In such a partial-substitution oxide, the shape and tilt of the MnO_6 octahedron depend on the rare-earths species at the A-site [6,7]. It is shown that in a tilt system, the predicted space groups are systematically summarized. Recently, a new oxide, $(Sr_{0.67}Sm_{0.33})(Mn_{0.33}Ti_{0.67})O_3$, was synthesized in an Ar flow. The structure had orthorhombic symmetry (*Pnma*), and an in-situ phase transition from *Pnma* to *Imma* has been reported [15].

In this paper, $(Sr_{0.67}Ln_{0.33})(Mn_{0.33}Ti_{0.67})O_3$ (Ln: Nd, Sm, Eu, Gd), was successfully synthesized at 1573 K in an Ar flow. The structure and in situ phase transition were analyzed by X-ray diffraction, electron diffraction, and a high-temperature transmission electron microscope.

Experimental

A polycrystalline oxide of $(Sr_{0.67}Ln_{0.33})(Mn_{0.33}Ti_{0.67})O_3$ (Ln: Nd, Sm, Eu, Gd) was synthesized by a solid-state reaction method. Starting materials (Ln_2O_3, $CaCO_3$, Mn_2O_3 and TiO_2) with 99.9% or better purity were used, and they were pre-treated by heating to adjust the oxidation state of these ions. Each of the pretreated reagents was weighed and then mixed with the others, and the mixture was pressed into pellets. The pellets were heated at 1573 K for 3 days in a purified Ar flow. The specimens were characterized using XRD (Cu Kα), and the XRD data was refined by the Rietveld method using the RIETAN program [16].

The specimens were crushed and placed on a copper mesh with carbon-coated micro-grids and then subjected to high-resolution TEM observations. The TEM (JEM-3000F, JEOL, Tokyo, Japan) was operated at 300 kV with spherical aberration $Cs = 1.0$ nm.

In situ observations were performed using a thermal stage in a temperature range from room temperature to 1073 K in the TEM (JEM-2100F, SHTH specimen holder, JEOL). The temperature was controlled manually, and the heating rate was about 800 K/h.

Results and Discussion

The structures of the oxides were clarified by Rietveld analysis of the XRD data, and they were found to be orthorhombic structures with the space group *Pnma*. Table 1 shows the atomic parameters of the room-temperature phase of the oxide. The crystal symmetry was also determined by an electron diffraction method, and it was in good agreement with the results shown in Table 1. We have reported results for the Sr-Sm oxide in a previous paper [15]. At this time, the parameters could be more refined and discussed as a better value of *R*wp.

The microstructures were observed using a high-resolution transmission electron microscope (HREM). Figure 1 shows a twining structure along the [101] zone axis. The insets shows simulated diffraction patterns (a and b) and superposed diffraction pattern (c). The simulation was performed using the atomic parameters in Table 1. The domain boundaries were not straight but coherent without mismatch. The twin boundary was formed by 90° rotation along the [101]/[10$\bar{1}$] zone axis.

Table 1. Crystallographic data and fractional atomic coordinates of $Sr_{0.67}Ln_{0.33}Mn_{0.33}Ti_{0.67}O_3$ (Ln=Nd, Sm, Gd, Eu).

	Ln=Nd	Ln=Sm	Ln=Eu	Ln=Gd
a (nm)	0.5516(1)	0.55094(9)	0.5509(1)	0.55001(9)
b (nm)	0.7808(1)	0.77814(6)	0.77780(5)	0.7782(1)
c (nm)	0.5515(1)	0.5510(1)	0.55077(9)	0.54995(6)
R_{wp} (%)	11.6	10.8	10.9	10.8
s	1.07	1.09	1.10	1.10
$x_{(Sr,Ln)}$	0.4877(3)	0.4847(2)	0.4843 (4)	0.4849 (5)
$z_{(Sr,Ln)}$	0.001(1)	0.001(2)	0.001(1)	0.003(2)
x_{O1}	0.003(2)	0.004(2)	0.008(2)	0.007(3)
z_{O1}	0.073(5)	-0.041(5)	0.078(5)	-0.086(6)
x_{O2}	0.269(4)	0.229(2)	0.268(4)	0.232(6)
y_{O2}	0.518(2)	0.464(2)	0.520(2)	0.483(4)
z_{O2}	0.240(7)	0.263(3)	0.235(5)	0.264(7)
$B_{(Sr,Ln)}$ (nm^2)	0.007(2)	0.007(2)	0.0061(8)	0.008(2)
$B_{(Mn,Ti)}$ (nm^2)	0.004(3)	0.004(2)	0.0021(9)	0.004(2)
B_{O1} (nm^2)	0.006(3)	0.005(2)	0.004(3)	0.005(4)
B_{O2} (nm^2	0.006	0.005	0.004	0.005

Space group *Pnma*:(Sr,Ln) and O1 in 4*c* (x,1/4,z), (Mn,Ti) in 4*a* (0,0,0), and O2 in 8*d* (x, y, z).

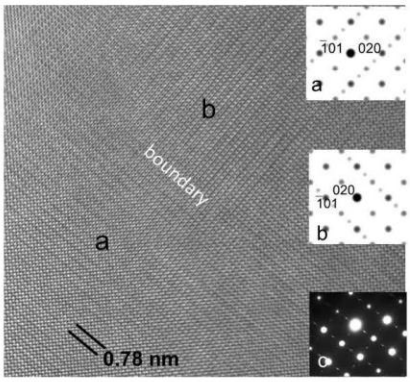

Fig.1 Twining of Sr-Nd oxide taken from the [101] zone axis.

Figure 2 shows the complex nano-domain structure of the Sr-Gd oxide, which was composed of three types of orientations. Each domain corresponded to those of the simulated diffraction patterns (a-c), and a selected area electron diffraction (SAED) pattern (d) was represented as a superposed diffraction pattern. The twin boundary of the [101]/[10$\bar{1}$] zone axis and the boundary of [101]/[010] were clearly observed in the HRTEM image. The complex twining was formed coherently because the (020) spacing is close to the (101) spacing in the Sr-Gd oxide, with a difference of 0.05%.

Other types of twin structures, which are formed by 60° rotation along the [210] zone axis, were also observed in all Sr-Ln oxides. In general, such a twin structure is formed by phase transition from higher symmetry to lower symmetry during the cooling process in perovskite [17]. Therefore, in this case, we expected that a phase transition would occur.

In situ observation of the phase transition was performed using a high-temperature TEM. Figure 3 shows changes by heating in the SAED patterns of Sr-Gd oxide taken from the [210] zone axis. In Fig. 3(a), this pattern was superposed of three patterns with *Pnma* symmetry, rotated by 60°. At 823 K, the intensity of reflections by twining decreased. Then, the structure transformed into a more highly symmetrical structure around 923 K. The high-temperature phase seems to have an orthorhombic *Imma* structure, as seen in Sr-Sm oxide[15]. In Sr-Nd oxide, the transition temperature was lower than that of Sr-Gd oxide.

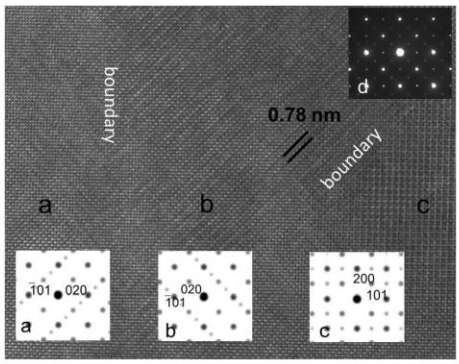

Fig.2 Nano-domains of Sr-Gd oxide taken from the [101]/[010] zone axis.

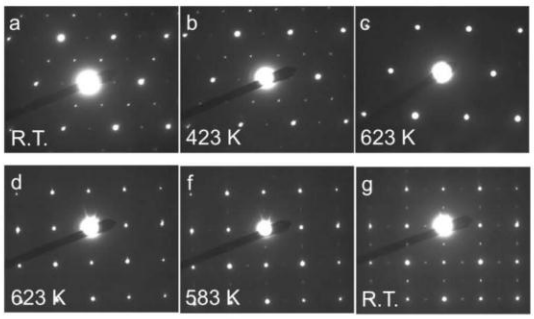

Fig. 4 Structural changes by heating in Sr-Nd oxide taken from [210] in (a)-(c) and those by cooling in that taken from [101] in (d)-(g).

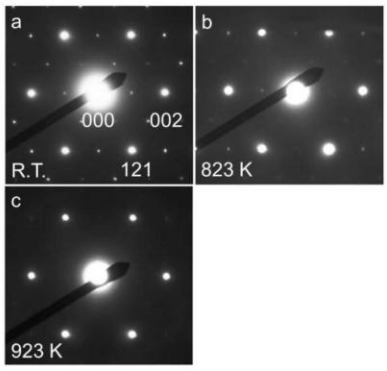

Fig.3 Structural changes by heating in Gd-oxide taken from [210].

Figure 4 shows changes in SAED patterns of Sr-Gd oxide by heating in (a)-(c) taken from the [210] axis and by cooling in (d)-(g) taken from the [101] axis. The phase transition was reversible. The transition occurred around 623 K, and the nano-domain structures disappeared above 623 K. During the cooling process, the nano-domain structures appeared again. Here, the high-temperature phase seems to have an orthorhombic *Imma* structure [6,7]. The phase transition occurred similarly in Sr-Eu oxide around 773 K. In the Sr-Ln oxide, the transition temperature was ordered Nd (623 K) < Sm (723 K) < Eu (773 K) < Gd (923 K). At this time, the phase transition was controlled by the tilting of an $(Mn,Ti)O_6$ octahedron from the three-tilt system (*Pnma*) to a two-tilt system (*Imma*). Therefore, the transition temperature was related to the ionic radius of the rare-earth ion in the A-site. The ionic radius is ordered Nd > Sm > Eu > Gd. In the largest cell size of Sr-Nd oxide, the degree of the octahedral tilting was smallest. As a result, the transition temperature was closely related to the radius of the rare earth ion and degree of octahedral tilting.

Conclusions

The perovskite oxides, $(Sr_{0.67}Ln_{0.33})(Mn_{0.33}Ti_{0.67})O_3$ (Ln: Nd, Sm, Eu, Gd), were synthesized at 1573 K in an Ar flow. These crystal structures were determined to be *Pnma* (No. 62) by X-ray diffraction and electron diffraction methods. High-resolution TEM observations of the oxides revealed that nano-domain structures were formed by twinning in these specimens. The twinning was formed easily by the phase transition during the cooling process. The twin boundary was coherent due to the small lattice mismatch. The phase transition of the oxide was successfully observed in situ by high-temperature TEM. The phase transition from *Pnma* to *Imma* was observed by heating, and it was found to be reversible by cooling. The transition temperature was ordered Nd (623 K) < Sm (723 K) < Eu (773 K) < Gd (923 K). Finally, the temperature was closely related to the radius of the rare earth ion and degree of octahedral tilting.

Acknowledgement

This work was partially supported by a Grant-in-Aid for Scientific Research (c) No. 21560704 by the Japan Society for the Promotion of Science.

References

1. R. Shiina, T. Nishitani, and H. Shiba, Magnetic ordering, orbital, and lattice distortion in perovskite manganites. *J. Phys. Soc, Jpn.* **66**(10), (1997), 3159-3170.
2. J. Q. Li, Structural properties of the perovskite manganite. *J. Apply. Phys.* **90**(2), (2001), 637-643.
3. S. Jin, M. Mavvormack, T.H. Tiefel, and R. Ramesh, Colossal magnetoresistance in La-Ca-Mn-O ferromagnetic thin-films. *J. Appl. Phys.* **76**(10), (1994), 6929-6933.
4. Y. Tokura, A. Urushibara, Y. Moritomo, T. Arima, A. Asamitsu, G. Kido, and N. Furukawa, Giant magnetotransport phenomena in filling-controlled Kondo lattice system: $La_{1-x}Sr_xMnO_3$. *J. Phys. Soc. Jpn.* **63**, (1994), 3931-3935.
5. A. Urushibara, Y. Moritomo, T. Arima, A. Asamitsu, G. Kido, and Y. Tokura, Insulator-metal transition and giant magnetoresistance in $La_{1-x}Sr_xMnO_3$. *Phys. Rev.B*, **51**, (1995), 14103-14109.
6. P. M. Woodward, Octahedral tilting in perovskites I. Geometrical considerations. *Acta Cryst.* **B53**, (1997), 32-43.
7. P. M. Woodward, Octahedral tilting in perovskites II. Structure stabilizing forces. *Acta Cryst.* **B53**, (1997), 44-66.
8. H. Nakano, N. Kamegashira, K. Urabe, In-situ observation of the change in domain structure due to phase transition in a perovskite La_2MnGaO_6. *Mater. Res. Bull.* **37**, (2002), 2107-2115.
9. N. Kamegashira, N. Nakajima, K. Watanabe, M. Kobayashi, Synthesis and crystal structure of Sm_2MnTiO_6, *J. Alloys and Compounds*, **311**, (2000), 74 –78.
10. N. Kamegashira, N. Nakajima, K. Watanabe, M. Kobayashi, Synthesis, crystal structure and magnetic properties of a new compound Eu_2MnTiO_6. *Int. J. Materials and Product Technology*, Special Issue, SPM1, **1**, (2001), 139 –146.
11. N. Kamegashira, M. Kobayashi, J. Saito, Synthesis, crystal structure and some properties of $Ln_2MnTiO6$ phases (Ln=rare earth). *Frontiers of Solid State Chemistry*, ed. By S. H. Feng and J. S. Chen, Words Scientific, (2002), 47 –52.
12. H. Nakano, N. Kamegashira, and K. Urabe, Structure analysis of a new oxide Yb_2TiMnO_6. *Mater. Res. Bull.***36**, (2001), 57-68.
13. M. Kobayashi, R. Katsuraya, S. Kurita, M. Yamaguchi, H. Satoh, N. Kamegashira, Synthesis and crystal structure of (Ca, R)(Mn, Ti)O_3 (R, rare earth). *J. Alloys and Compounds*, **408-412**, (2006), 1173-1176.
14. M. Kobayashi, M. Yamaguchi, N. Kamegashira, Refinement of crystal structure of $MLaMnTiO_6$ (M = Ba, Sr) and $CaSmMnTiO_6$. *International Symposium on Designing, Processing and Properties of Advanced Engineering Materials*, (1997), 505-510.
15. H. Nakano, M. Kobayashi, N. Kamegashira, Nano-domain twin structure formed by phase transition in new perovskite ocide $(Sr_{0.67}Sn_{0.33})(Mn_{0.33}Ti_{0.67})O_3$. *J. Am. Ceram. Soc.* **90** (4), (2007), 1276-79.
16. F. Izumi, A software package fir the Rietveld analysis of X-ray and neutron diffraction patterns *J. Crystallogr. Jpn.* **27** (1985), 23-31 [in Japanese].
17. Y. Wang, R.C. Liebermann, Electron microscopy study of domain structure due o phase transitions in natural perovskite. *Phys. Chem. minerals* **20**, (1993), 147-158.

IOP Conf. Series: Materials Science and Engineering **18** (2011) 082018 doi:10.1088/1757-899X/18/8/082018

Microstructure and luminescence of rare earth doped $Li(Nb,Ti)O_3$ solid solutions

Hiroyuki Hayashi[1], **Hiromi Nakano**[2], **Mark I. Jones**[3]

[1] KRI, Inc. Nano-Device Research Laboratory, Kyoto Research Park, 134, Chudoji Minami-machi, Shimogyou-ku, Kyoto 600-8813, Japan

[2] Toyohashi University of Technology Cooperative Research Facility Centre, Tempaku, Toyohashi, 441-8580, Japan

[3] Dept of Chemical & Materials Engineering, University of Auckland, Auckland, Private Bag 92019, Auckland, New Zealand.

E-mail : h-hayasi@kri-inc.jp

Abstract. $Li_{1+x-y}Nb_{1-x-3y}Ti_{x+4y}O_3$ ($0.11 \leq x \leq 0.33$, $0 \leq y \leq 0.09$) solid solutions in the Li_2O-Nb_2O_5-TiO_2 ternary system are known as M Phase with superstructure. Eu doped $Li_{1+x-y}Nb_{1-x-3y}Ti_{x+4y}O_3$ (LNT) solid solutions were prepared by firing mixed powders at temperatures of 1120 ℃ for up to 24 hours. The interval of intergrowth layers of Eu doped LNT solid solution was as twice as that of no doped LNT solid solution. Another rare earth (Dy, Sm, Tm, Er) doped LNT solid solutions were also prepared each other. These LNT solid solutions with 20 mol%-TiO_2 did possess a disorder structure, but did not possess a superstructure. PL intensity of Eu doped LNT solid solution was higher than Eu doped $LiNbO_3$ (LN) solid solution. However, PL intensity of another rare earth doped LNT solid solutions was less than LN solid solutions each other. It was thought that the distribution of Eu and Ti and a relative distance between Eu and Ti were optimized by the formation of the superstructure and PL intensity of Eu doped LNT solid solutions increased.

1. Introduction

$Li_{1+x-y}Nb_{1-x-3y}Ti_{x+4y}O_3$ ($0.11 \leq x \leq 0.33$, $0 \leq y \leq 0.09$) (hereafter LNT) forms solid solutions with a superstructure, known as the M Phase, in the Li_2O-Nb_2O_5-TiO_2 ternary system. Since the discovery of this M Phase by Villafuerte-Castrejon *et al.*[1, 2], both its crystal structure [3, 4, 5, 6] and the applications of Phase M [7, 8, 9] have been studied. LNT solid solutions of M Phase have an hexagonal subcell similar to the unit cell of $LiNbO_3$, which belongs to the Trigonal system (*R3c*), and has lattice constants of a=0.5148nm, c=1.3863nm. The superstructure of LNT solid solutions was identified using HREM as having layer-like domains.[4, 5] where stacking faults are inserted parallel to the c axis in the $LiNbO_3$ structure. The superstructure normally observed in LNT solid solutions can be observed in XRD spectra as a splitting of the (012) peak of the $LiNbO_3$ structure at around $2\theta = 23°$, where the peak can be resolved into 4 different components. The stacking faults have a rock-salt structure and the dimension of the domain along the c axis based on a $LiNbO_3$-like subcell has been controlled by TiO_2 content and sintering temperature.[5] The superstructure periodicity has been shown to decrease with increasing TiO_2 content.

Hayashi *et al.* confirmed that LNT solid solutions doped with Eu was a superior red phosphor to Eu doped LN solid solution, and that the optimum additive amount of Eu_2O_3 was 2.5 wt%. [6] In those

Corresponding author H. Hiroyuki : Kyoto Research Park, 134, Chudoji Minami-machi, Shimogyou-ku, Kyoto 600-8813, Japan

materials, the solid solutions did not display a superstructure for short sintering times, but the superstructure was developed for longer sintering periods. It was also observed that the longer sintering time led to increase PL intensity. [7]
The purpose of this study was to;.
1. Prepare LNT solid solutions doped with Dy, Er, Sm and Tm.
2. Verify the beneficial effect of LNT solid solutions with a superstructure on the PL intensity.

2. Experimental Procedure

The starting materials were Li_2CO_3 (Wako), Nb_2O_5 (Wako, 3N), TiO_2 (Wako) and Eu_2O_3 (Shin-Etsu Chemical Co.,Ltd, 4N). Powder blends were prepared by dry mixing to give compositions of $Li_{1+x-y}Nb_{1-x-3y}Ti_{x+4y}O_3$:RE solid solutions with x=0.43, y=0 (20 mol% TiO_2 content). The RE_2O_3 (RE : Dy, Er, Eu, Sm and Tm) content was 2.5 wt%. The mixed powder was sintered at 1000 ℃ for 3 hours and 1120 ℃ (24 hours) in air. Excitation and emission spectrum of samples was measured using a spectrometer FP-6500 model (JASCO). XRD measurement was carried out with a RINT2500 (Rigaku Co. Ltd.) at 50kV and 200mA. Structure images and selected area electron diffraction patterns (SAED) were observed by High Resolution TEM (JEM-3000F, JEOL Co. Ltd.) at 300kV. Chemical composition was analyzed by using a HREM, which makes it possible to provide electron probes width at half maximum of ~0.5 nm.

3. Results and Discussions

No secondary phases such as $RENbO_4$ or RE_2O_3 were observed in the XRD spectra for the samples. Figure 1 shows variation in the (012) peak for samples doped with different rare earths. The undoped

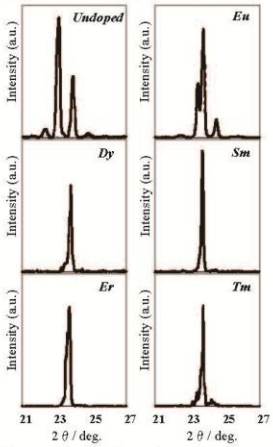

Figure 1 XRD patterns of the (012) peak of undoped and doped LNT:RE solid solutions.

LNT solid solution clearly demonstrates a superstructure, as does the Eu doped LNT solid solution, although the distance between the split peaks in the (012) peak was shorter. The (012) peak of LNT:Dy, LNT:Er, LNT:Sm and LNT:Tm solid solutions was not clearly showed splitting. However, the (012) peaks were not sharp and showed evidence of a shoulder. It was thought that these LNT:RE solid solutions did possess a partially modulated periodic structure. The structure of both the Eu and Sm doped LNT solid solutions were further observed by High resolution TEM.

materials, the solid solutions did not display a superstructure for short sintering times, but the superstructure was developed for longer sintering periods. It was also observed that the longer sintering time led to increase PL intensity. [7]
The purpose of this study was to;.
1. Prepare LNT solid solutions doped with Dy, Er, Sm and Tm.
2. Verify the beneficial effect of LNT solid solutions with a superstructure on the PL intensity.

2. Experimental Procedure

The starting materials were Li_2CO_3 (Wako), Nb_2O_5 (Wako, 3N), TiO_2 (Wako) and Eu_2O_3 (Shin-Etsu Chemical Co.,Ltd, 4N). Powder blends were prepared by dry mixing to give compositions of $Li_{1+x-y}Nb_{1-x-3y}Ti_{x+4y}O_3$:RE solid solutions with x=0.43, y=0 (20 mol% TiO_2 content). The RE_2O_3 (RE : Dy, Er, Eu, Sm and Tm) content was 2.5 wt%. The mixed powder was sintered at 1000 ℃ for 3 hours and 1120 ℃ (24 hours) in air. Excitation and emission spectrum of samples was measured using a spectrometer FP-6500 model (JASCO). XRD measurement was carried out with a RINT2500 (Rigaku Co. Ltd.) at 50kV and 200mA. Structure images and selected area electron diffraction patterns (SAED) were observed by High Resolution TEM (JEM-3000F, JEOL Co. Ltd.) at 300kV. Chemical composition was analyzed by using a HREM, which makes it possible to provide electron probes width at half maximum of ~0.5 nm.

3. Results and Discussions

No secondary phases such as $RENbO_4$ or RE_2O_3 were observed in the XRD spectra for the samples. Figure 1 shows variation in the (012) peak for samples doped with different rare earths. The undoped

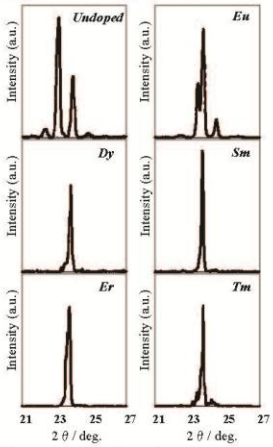

Figure 1 XRD patterns of the (012) peak of undoped and doped LNT:RE solid solutions.

LNT solid solution clearly demonstrates a superstructure, as does the Eu doped LNT solid solution, although the distance between the split peaks in the (012) peak was shorter. The (012) peak of LNT:Dy, LNT:Er, LNT:Sm and LNT:Tm solid solutions was not clearly showed splitting. However, the (012) peaks were not sharp and showed evidence of a shoulder. It was thought that these LNT:RE solid solutions did possess a partially modulated periodic structure. The structure of both the Eu and Sm doped LNT solid solutions were further observed by High resolution TEM.

High resolution TEM image and electron diffraction pattern for the [010] zone axis of undoped LNT solid solution with 20mol% TiO_2 are shown in Figure 2 (a) and (b).The superstructure was

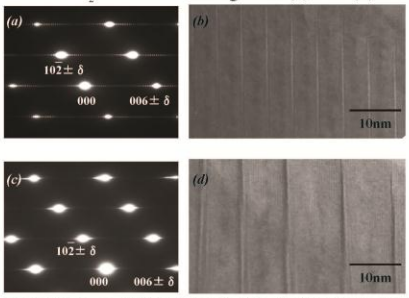

Figure 2 Electron diffraction patterns and High Resolution TEM photographs of undoped (a,b) and Eu doped (c,d) LNT solid solutions

observed as periodic intergrowth layers. Satellite diffraction along *c** axis was clearly observed in the electron diffraction pattern. For the Eu doped 20mol% TiO_2 LNT solid solutions the spacing of the intergrowth layers was about twice that of the undoped LNT solid solution. The structure of Sm doped LNT solid solution (Figure 3) has a partially modulated period with an intergrowth layer interval around 4 times that of the undoped LNT solid solution. This disordered structure was also observed in the Dy, Er and Tm doped LNT solid solutions (data not shown).

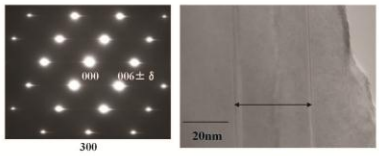

Figure 3 Electron diffraction pattern and High resolution TEM photograph of LNT:Sm solid solutions.

The excitation spectra of both LN:RE and LNT:RE solid solutions are shown in Figure 4. With the exception of the Eu doped LNT solid solution, the excitation intensity of LNT:RE solid solutions was

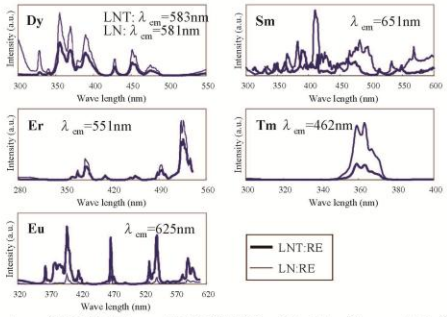

Figure 4 Excitation spectra of LNT:RE and LN:RE (Dy, Er, Eu, Sm and Tm) solid solutions. The bold line shows LNT:RE and the narrow line shows LN:RE

lower than that of the corresponding than LN:RE samples for all dopants. This result was also observed in the emission spectra (Figure 5) where the PL intensity of the Eu doped LNT solid solutions was higher than the Eu doped LN solid solution. For all other rare earths the LNT solid solutions had lower intensity than the corresponding LN:RE solid solutions. These samples also showed emission at different wavelengths with the LNT:Dy demonstrating Yellow emission, LNT:Sm (Red), LNT:Tm (Blue), LNT:Er (Green) and LNT:Dy,Tm (White emission).

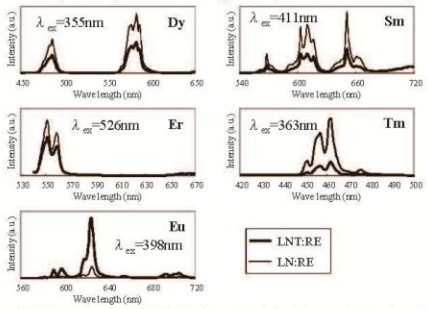

Figure 5 Emission spectra of LNT:RE and LN:RE (Dy, Er, Eu, Sm and Tm) solid solutions. The bold line shows LNT:RE and the narrow line shows LN:RE.

It was thought that the distribution of Eu and Ti and the relative distance between Eu and Ti were optimized by the formation of the superstructure resulting in the increase in PL intensity of the Eu doped LNT solid solutions. The, Sm, Eu and Er doped LNT solid solutions, in particular, are expected as new phosphors excited by a visible radiation.

4. Summary

The luminescence and microstructure of Dy, Er, Eu Sm and Tm doped LNT solid solutions prepared by sintering at 1120 ℃ for 24 hours were evaluated. Eu doped LNT solid solution possessed a superstructure, but this was less well defined in the Dy, Er, Sm and Tm doped LNT solid solutions. The PL intensity of the Eu doped LNT solid solution was much higher than a comparable Eu doped LN solid solution. However, for the other rare earth doped samples the PL intensity of the LNT solid solutions was lower than equivalent LN solid solutions.

Acknowledgement

Mr. Mutsuo Masuda (KRI Inc.) for helpful advice on emission characteristics. One of the author (H.N.) would like to acknowledge partial supported by a Grant-in-Aid for Scientific Research (c). No. 21560704 (H. N.) from the Japan Society for the Promotion of Science.

Reference

[1] Villafuerte-Castrejon M E, Gracia J A, Cisneros E, Valenzuela R and Wes A R 1984 *Trans. J. Brit. Ceram. Soc.*, **83**, 143
[2] Villafuerte-Castrejon M E, Aragon-Pina A, Valenzuela R and West A R 1987 *J. Solid State Ceram.*, **71**, 103
[3] Smith R I and West A R 1992 *Mat. Res. Bull.*, **27**, 277.
[4] Hayashi H, Nakano H, Suzumura K, Urabe K and West A R 1995 *Forth Ceram. Soc.*, **2** 391
[5] Hayashi H, Urabe K and Niihara K 1999 *Key Engineering materials* **161-163**, 501
[6] Hayashi H and Nakano H 2010 *J. Alloy and Compounds*, **502**, 360
[7] Hayashi H, Nakano H and Jones M I 2010 *J. Ceram. Soc. Japan*, **118**, 226.

IOP Conf. Series: Materials Science and Engineering **18** (2011) 082023 doi:10.1088/1757-899X/18/8/082023

Crystal structures of solid solution $(Ba_{1-x}Ca_x)(Sc_{1/2}Nb_{1/2})O_3$ system

Hiromi Nakano[1], Takashi Ida[2], Minoru Takemoto[3], Hiroyuki Ikawa[3]
[1]Toyohasi University of Technology, Tempaku, Toyohashi, 441-8580, Japan
[2]Nagoya Institute of Technology, Asahigaoka, Tajimi, 507-0071, Japan
[3]Kanagawa Institute of Technology, Shimo-ogino, Atsugi, 243-0292, Japan
E-mail: hiromi@crfc.tut.ac.jp

Abstract. The solid solutions of $(Ba_{1-x}Ca_x)(Sc_{1/2}Nb_{1/2})O_3 (0 \le x \le 0.8)$ are synthesized in a wide composition range. In the present study, the crystal structures are determined by a synchrotron X-ray diffraction and an electron diffraction method. The crystal structure of $Ba(Sc_{1/2}Nb_{1/2})O_3$ ($x = 0$) has a cubic symmetry ($Fm\bar{3}m$) with atomic parameters of about 0.8 nm (2 x 2 x 2 cells) judging by the appearance of very weak 111 reflections. The reflection intensity depends on the ordering in the B-cation. Furthermore, structural changes occur in the crystal symmetry, where the symmetries tend to decrease with increasing Ca content. This is controlled by the BO_6 tilting system, since the cell sizes become smaller with increasing Ca content. Consequently, in the B-site, Sc^{3+} and Nb^{5+} ions come to have an orderly arrangement with increasing Ca content.

1. Introduction

The development of high-performance dielectric material is needed for microwave communication circuits. In general, the paraelectric properties of the perovskite oxides change as a matter of course by partial substitutions of their A-site ion or B-site ion. Various double perovskites have been studied with systems of $(A_{1-x}A'_x)(B^{2+}_{1/3}Ta^{5+}_{2/3})O_3$ (A, A' = Ba, Sr, Ca; B= Mg, Zn) and $A_2B^{3+}M^{5+}O_6$(A =Ba, Sr; B = rare earth, M = Sb, Nb, Ta) [1-3]. To design such new material, crystal structural analysis is important for clarifying the mechanisms of the electrical properties.

Recently, Ikawa et al. have succeeded in synthesizing a new solid solution of $(Ba_{1-x}Ca_x)(Sc_{1/2}Nb_{1/2})O_3$ $(0 \le x \le 0.8)$ in a wide composition range [4]. Substitution of the Sc ion in the B-site might be successful for synthesis in the wide composition range of in the solid solution. The detailed structures of A_2B^{3+} Ta O_6 and A_2B^{3+} Nb O_6 have been reported; Ba_2ScNbO_6 is a cubic structure with a space group of $Fm\bar{3}m$, and Ca_2ScNbO_6 is a monoclinic structure with $P2_1/n$ [5]. The crystal structure of the perovskite has been investigated systematically by tilting systems describing BO_6 octahedral tilting. The magnitude of distortion in the tilt systems is estimated by substitutions in the A-site or B-site of double perovskite [6]. In this solid solution system, structural change can be expected from a cubic symmetry to a monoclinic symmetry. The detailed structure was determined with a synchrotron X-ray diffraction and an electron diffraction method. We discuss the changes in the structure related to the tilt system of the perovskite structure.

Coresponding author H. Nakano : 1 Toyohasi University of Technology, Tempaku, Toyohashi, 441-8580, Japan

2. Experimental procedure

Starting materials used were $BaCO_3$, $CaCO_3$, Sc_2O_3 and Nb_2O_5 (> 99.9% grade) to prepare the solid solution of $(Ba_{1-x}Ca_x)(Sc_{1/2}Nb_{1/2})O_3$. After the first and second calcinations at 1473 K for 12 h and 9 h, respectively, the mixtures were sintered at 1923 K for 12 h in air. The detailed procedure was previously described [4]. The structures of the obtained specimens were analyzed by electron diffraction (JEM-2100F, JEOL, Tokyo, Japan) and by synchrotron X-ray diffraction at the KEK-PFBL-4B2 experimental station in Tsukuba, Japan. The high-resolution images and chemical compositions were taken by a transmission electron microscope (TEM) equipped with energy-dispersive spectroscopy (EDS).

3. Results and discussions

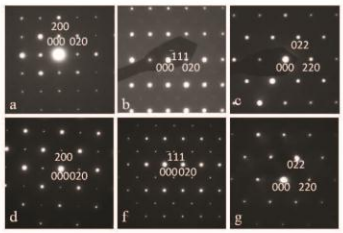

Figure 1. SAED patterns of oxides in (a)-(c) x = 0, (d)-(g) x = 0.3. Zone axes are [001] in (a) and (d), [101] in (b) and (f), and [111] in (c) and (g).

The selected area diffraction (SAED) patterns of oxides (x = 0, 0.3, 0.5, 0.8) were taken from several zone axes, and the chemical composition of each grain was determined by EDS. The chemical compositions calculated from the EDS measurements agreed with the nominal compositions within the experimental errors. However, the observed ratios of Sc/Nb contents were slightly smaller than the unity for all the samples. Small amount of Sc_2O_3 particles were also detected as a secondary phase in the products. It is suggested that the content of Sc ion is slightly lowered in the principal phase and the charge valence should be maintained by generating defects of alkaline earth ions located at the A-site of the perovskite structure.

Table 1. Atomic parameters of oxides refinement by Rietveld analysis

	site	Atom	Occupancy	x	y	z
$Ba_{0.98}(Sc_{0.48}Nb_{0.52})O_3$	8c	Ba^{2+}	0.980(10)	1/4	1/4	1/4
a = 0.823810(1) nm	4a	Nb^{5+}/Sc^{3+}	0.52/0.58	0	0	0
R_{wp} = 8.57 %	4b	Sc^{3+}/Nb^{5+}	0.48/0.52	1/2	1/2	1/2
	24e	O^{2-}	1	0.25(8)	0	0
$(Ba_{0.7}Ca_{0.3})_{0.98}(Sc_{0.48}Nb_{0.52})O_3$	8c	Ba^{2+}/Ca^{2+}	0.686/0.294	1/4	1/4	1/4
a = 0.815908(0) nm	4a	Nb^{5+}/Sc^{3+}	0.787/0.213	0	0	0
R_{wp} = 5.60 %	4b	Sc^{3+}/Nb^{5+}	0.748/0.252	1/2	1/2	1/2
	24e	O^{2-}	1	0.2483(7)	0	0

Figure 1 shows typical SAED patterns of oxides (x = 0 and 0.3). The reflections were indexed as cubic structures of about 0.8 nm (2 x 2 x 2 cells) in the oxides. These SAED patterns were clearly different with increasing Ca content. In Fig. 1(b), very weak 111 reflection and equivalent reflections were

detected. The reflections were caused by the ordering of the Sc and Nb ions in the B-site [5]. The unit cell size should be 2 x 2 x 2 cells by the appearance of the 111 reflection. The crystal symmetry of the oxide was expected to be cubic with a space group of $Fm\bar{3}m$. In the oxide ($x = 0.3$), the 111 reflection intensity became stronger with increasing Ca content in the same crystal symmetry. This means that the Sc and Nb ions were arranged in a more orderly manner in the B-site due to the reduction in cell size with increasing Ca content. The synchrotron X-ray diffraction analysis was carried out based on the results. Atomic parameters refined by Rietveld analysis are shown in Table 1. The R_{wp} value of the oxide ($x = 0$) was higher, since very weak 111 reflections could not be detected by the synchrotron X-ray diffraction method.

Figure 2. SAED patterns of oxide ($x = 0.5$) taken from the [001] axis in (a), [101] axis in (b), [111] axis in (c).

In the oxide ($x = 0.5$), weak 110 reflection appeared as shown in Fig. 2. Therefore, the crystal symmetry was not in agreement with $Fm\bar{3}m$. The crystal structure with $Fm\bar{3}m$ belongs to a non-tilting system described as $a^0\ a^0\ a^0$ in the perovskite structure [5]. By reduction of the cell size, the structure should change from a non-tilting to a tilting system. The pattern of the synchrotron X-ray diffraction showed broad peaks in the high-angle range. This means that the crystal structure is not a cubic symmetry. We considered some possible crystal symmetries based on the extinction rule from the SAED patterns. Finally, the space group of $C2/c$ (No. 15) was adopted as the most possible symmetry. The symmetry belongs to a two-tilt system as $a^0\ b^+c^-$. Atomic parameters refined by Rietveld analysis are shown in Table 2.

Table 2. Atomic parameters of $(Ba_{0.5}Ca_{0.5})_{0.98}(Sc_{0.48}Nb_{0.52})O_3$ refinement by Rietveld analysis

site	Atom	Occupancy	*x*	*y*	*z*
4e	Ba^{2+}/Ca^{2+}	0.4925/0.4925	0	0.0053(2)	1/4
4e	Ba^{2+}/Ca^{2+}	0.4925/0.4925	0	0.4975(2)	1/4
4c	Nb^{5+}/Sc^{3+}	0.823/0.177	1/4	1/4	0
4d	Sc^{3+}/Nb^{5+}	0.793/0.207	1/4	1/4	1/2
8f	O^{2-}	1	0.2352(3)	0.0100(2)	0
8f	O^{2-}	1	0.00100	0.2648	-0.0421(2)
8f	O^{2-}	1	0.2079(12)	0.25	0.24

$a = 0.868(8)$ nm, $b = 0.80865(3)$ nm, $c = 0.80876(8)$ nm, $\beta = 90.000(10)$ degree, $R_{wp} = 5.11\%$

Furthermore, the crystal symmetry became lower in the oxide ($x = 0.8$). We noticed that there were many nano-twin domains in the TEM images taken from the [001] zone axis as a pseudo-cubic cell. In the cubic cell, no domains could be observed along the [001] zone axis because [100] and [010] are equivalent. Therefore, we took the SAED pattern using the smallest aperture of the selected area diffraction. The diffraction patterns in Fig. 3(a) and (b) are taken from the near area. The superposed pattern was composed by twinning in Fig. 3(c). The (100) spacing was nearly equal to the (010) spacing, and the split reflections were not observed in Fig. 3(c). Along the [111] zone axis, the superposed pattern of Fig. 3(e) is composed of three patterns in Fig. 3(d) rotated by 60°. Such a nano-twin structure has also been observed in a perovskite $(Sr_{0.67}Sm_{033})(Mn_{0.33}Ti_{0.67})O_3$ with a space group

of *Pnma* [7]. Finally, the space group of $P2_1/n$ (No. 14) was adopted as the most possible symmetry. The symmetry belongs to a three-tilt system as $a^+ b^- b^-$. Atomic parameters refined by Rietveld analysis are shown in Table 3.

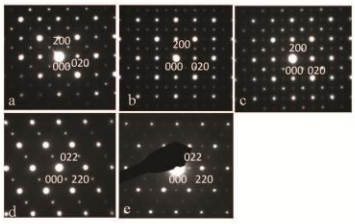

Figure 3. SAED patterns of oxide ($x = 0.8$) taken from the [001] axis in (a) -(c), [111] axis in (d)-(e) as a pseudo-cubic.

Table 3. Atomic parameters of $(Ba_{0.2}Ca_{0.8})_{0.96}(Sc_{0.46}Nb_{0.54})O_3$ refinement by Rietveld analysis

Atom	Occupancy	*x*	*y*	*z*
Ba^{2+}/Ca^{2+}	0.1927/0.7671	0.0004(4)	-0.01573(13)	0.26389(5)
Nb^{5+}/Sc^{3+}	0.741/0.259	0	1/2	0
Sc^{3+}/Nb^{5+}	0.668/0.332	1/2	0	0
O^{2-}	1	0.2539(7)	0.2591	-0.0460(2)
O^{2-}	1	0.2591	0.2539	0.5460
O^{2-}	1	0.4080	0.0100(10)	0.2526

$a = 0.56312(2)$ nm, $b = 0.563484(18)$ nm, $c = 0.79673(3)$ nm, $\beta = 89.951$ degree, $R_{wp} = 6.13\%$

5. Conclusion

The crystal structures of oxides of $(Ba_{1-x}Ca_x)(Sc_{1/2}Nb_{1/2})O_3$ $(0 \le x \le 0.8)$ were determined with a synchrotron X-ray diffraction and an electron diffraction method. The chemical compositions were analyzed by energy-dispersive spectroscopy. The oxide ($x \le 0.3$) possessed a cubic cell ($Fm\bar{3}m$) in a non-tilt system due to the ordering of Sc and Nb ions. With increasing Ca content, Sc and Nb became arranged in a more orderly way. Through a reduction in the cell size, the structure changed from a non-tilting to a tilting system. The oxide ($x = 0.5$) possessed a monoclinic cell ($C2/c$) in a two-tilt system, and the oxide ($x = 0.8$) possessed a monoclinic cell ($P2_1/n$) in a three-tilt system. In the A-site, however, Ba and Ca ions were arranged randomly. We clarified the relationship between Ca content and the structural symmetry in the $(Ba_{1-x}Ca_x)(Sc_{1/2}Nb_{1/2})O_3$ system.

References

[1] Wittmann U V, Rauser G, Kemmler S, Z.1981, *Anorg.Allg.Chem.* **482**, 143
[2] Ikawa H, Yamashiro M, Niwa M, Omata T, Urabe K, 1996, *Trans Mater. Res. Soc. Jpn.* **20**, 632
[3] Ikawa H, Yamashiro M, Fukuhara M, Takemoto M, 1998, *Proc. 11th International symposium on application of ferroelectrics* 529
[4] Ikawa H, Ohara M, Iida T, Takayama M, Takemoto M, 2004, *J. Ceram. Soc. Jpn.* 112(5) S1614
[5] Barnes PW, Lufaso MW, Woodword PM, 2006, *Acta Cryst.*, **B 62,** 384
[6] Woodward PM, 1997, *Acta Cryst.*, **B53**, 32
[7] Hiromi N, Kobayashi M, Kamegashira N, 2007, *J. Am. Ceram. Soc.*, **90(4)**, 1276

This work was partially supported by a Grant-in-Aid for Scientific Research (c) No. 21560702 (M. T.) and No. 21560704 (H. N.) by the Japan Society for the Promotion of Science.

Journal of Alloys and Compounds 502 (2010) 360–364

Contents lists available at ScienceDirect

Journal of Alloys and Compounds

journal homepage: www.elsevier.com/locate/jallcom

Evaluation and preparation of $Li_{1+x-y}Nb_{1-x-3y}Ti_{x+4y}O_3$ solid solution with superstructure as new phosphor

Hiroyuki Hayashi [a,*], Hiromi Nakano [b]

[a] KRI, Inc. Device Process Unit, Nano-Device Research Laboratory, Kyoto research Park, 134, Chudoji Minami-machi, Shimogyo-ku, Kyoto 600-8813, Japan
[b] Faculty of Science and Technology, Ryukoku University, Seta, Otsu, Shiga 520-2194, Japan

ARTICLE INFO

Article history:
Received 2 June 2009
Received in revised form 19 April 2010
Accepted 24 April 2010
Available online 4 May 2010

Keywords:
Superstructure
$LiNbO_3$
TiO_2
Phosphor
Eu_2O_3

ABSTRACT

New red phosphors have been investigated in this study with europium as an activator added to $Li_{1+x-y}Nb_{1-x-3y}Ti_{x+4y}O_3$ (LNT) solid solutions with an M Phase superstructure. The photo-luminescence intensity of LNT:Eu solid solutions was dependent on the levels of both the Eu doping and the TiO_2 content, and was superior to that of $LiNbO_3$:Eu. LNT:Eu solid solutions with 2.5 wt.% Eu_2O_3 showed the highest performance in this work, and maximum intensity was observed when the TiO_2 content of LNT:Eu solid solutions was 10 mol.%. Structural analysis by XRD and HREM showed that in these new phosphors the M Phase superstructure was affected by the doping, with the periodicity of the superstructure becoming wider and more random.

1. Introduction

$Li_{1+x+y}Nb_{1-x-5y}Ti_{x+4y}O_3$ ($0.11 \leqq x \leqq 0.33$, $0 \leqq y \leqq 0.09$) (hereafter LNT) forms solid solutions with a superstructure, known as the M Phase, in the Li_2O–Nb_2O_5–TiO_2 ternary system. Since the discovery of this M Phase by Villafuerte-Castrejon et al. [1,2], both its crystal structure [3–6] and the applications of Phase M [7–9] have been studied. LNT solid solutions of M Phase have a hexagonal subcell similar to the unit cell of $LiNbO_3$, which belongs to the trigonal system (*R*3*c*), and has lattice constants of $a = 0.5148$ nm, $c = 1.3863$ nm. The superstructure of LNT solid solutions was identified using HREM as having layer-like domains [4,5], where stacking faults are inserted parallel to the *c* axis in the $LiNbO_3$ structure. The stacking faults have a rock-salt structure and the dimension of the domain along the *c* axis based on a $LiNbO_3$-like subcell has been controlled by TiO_2 content and sintering temperature [5]. The period of superstructure was shown to decrease with increasing TiO_2 content.

Eu doped $LiNbO_3$ thin films showing stress luminescence have been reported [10] and recently, $LiNbO_3$ (hereafter LN) as a host crystal for phosphors has been studied [11]. The ionic radius of Eu is sufficiently larger than that of Li or Nb and if not controlled via sintering temperature, Nb_2O_5 reacts with Eu_2O_3 to form $EuNbO_4$ [11].

Fluorescent thin films with a superstructure formed by CVD have been researched, and it was reported that the luminescence was superior to that of a thin film with normal structure [6]. These superstructures consist of periodic layering where each layer has the same crystal structure, but the lattice constants and compositions of individual layers are different. Distortion of the structure introduced by differences in the two lattice constants was inserted periodically in the microstructure of the solid solution. This leads to improved properties when compared to the base compound due to the strain energy. However, in order to prepare them, special equipment is required such as CVD for semiconductor manufacturing equipment. In addition the applications of such superstructured materials are limited in the thin film field.

On the other hand, M Phase solid solutions have a self-organized super lattice which can be prepared in a commercial furnace. The super-periodicity of M Phase solid solutions can be controlled by the composition and sintering temperature, and employing this spontaneous superstructure it is possible to prepare by materials by a commercial powder mixing method and sol–gel method [5]. Therefore M Phase has the advantage that the sintered bodies can be prepared as single crystal [12,13], bulk body [5], powder and thin film [12,13].

In this work we have prepared Eu doped LN and Eu doped LNT solid solutions of M Phase. In terms of improving the luminescence property of LNT:Eu, the relationship between Eu additive amount or

* Corresponding author.
E-mail addresses: h-hayasi@kri-inc.jp (H. Hayashi), hiromi@rins.ryukoku.ac.jp (H. Nakano).

0925-8388/$ – see front matter © 2010 Elsevier B.V. All rights reserved.
doi:10.1016/j.jallcom.2010.04.168

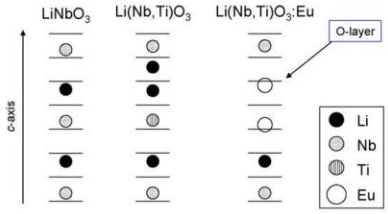

Fig. 1. The schematic of structure of $LiNbO_3$, LNT solid solution and Eu doped LNT solution.

Ti displacement amount and the luminescence intensity of LNT:Eu. has been clarified.

2. Experimental procedure

The compositions of LNT:Eu solid solutions in this work were $0 \le x \le 0.33$ and $y = 0$. Starting materials of Li_2CO_3 (Wako), Nb_2O_5 (Wako, 3N), TiO_2 (Wako) and Eu_2O_3 (Wako, 3N) were prepared by dry mixing. The mixed powder was sintered at both 1000 °C (3 h) and 1120 °C (10 h) in air. The Eu_2O_3 content was varied from 1 to 5 wt.%.

The excitation and emission spectra of the samples were measured by a spectrometer FP-6500 model (JASCO). XRD was carried out using a RINT2500 (Rigaku Co. Ltd.) at 50 kV and 200 mA. Structural images and selected area electron diffraction patterns (SAED) were observed by high-resolution TEM (JEM-3000F, JEOL Co. Ltd.) at 300 kV. Chemical composition was analyzed using a HREM, which makes it possible to provide electron probes with at half maximum of ~0.5 nm, and also with sufficiently high current for a point analysis by energy dispersive X-ray spectroscopy (EDS) (Noran Instruments Voyager III).

3. Results and discussions

The identification of phase and crystal structure analysis of Eu doped LNT solid solutions were observed by XRD. The microstructure of LNT solid solutions of Phase M have a $LiNbO_3$-like subcell structure and the structure of stacking faults periodically inserted in the LNT crystal is a rock-salt structure of Li_2TiO_3 [5]. The Ti mainly exists in the stacking faults of the superstructure. When considering the charge balance when Eu is doped into LNT, two types of the displacement are possible.

$$Li^{1+} + Nb^{5+} \rightarrow 2Eu^{3+}$$

$$2Li^{1+} + Ti^{4+} \rightarrow 2Eu^{3+}$$

It was considered that the Eu can therefore exist in both the $LiNbO_3$-like subcell and the stacking faults. Fig. 1 shows the schematic of structure of $LiNbO_3$, LNT solid solution and Eu doped LNT solution. Consequently, in these doped materials there is the possibility that $LiNbO_3$ and Li_2TiO_3 remains as a secondary phase, or unreacted Eu_2O_3 may be found in the product. There is also a danger that $EuNbO_4$ and $EuTiO_3$ may be produced. XRD spectra of the Eu doped LN samples are shown in Fig. 2. It can be seen that the prepared samples have the $LiNbO_3$ structure and $EuNbO_4$ is observed in both 2.5 and 5% Eu_2O_3 doped samples. The amount of $EuNbO_4$ in the product increased with increasing additive amount of Eu_2O_3.

Fig. 3 shows the XRD patterns of LNT solid solutions with 10 mol.% TiO_2 and different amounts of Eu_2O_3 additions. In these samples no $EuNbO_4$ was observed for Eu_2O_3 additions up to 3%. However, for the 5 wt.% Eu_2O_3 additive the excess Eu reacted with Nb to form $EuNbO_4$. The differences in the amount of Eu_2O_3 that is required before the $EuNbO_4$ phase is observed indicates that the solid solubility limit of Eu for LNT solid solutions is greater than that of LN.

The superstructure normally observed in LNT solid solutions results can be observed as a splitting of the (0 1 2) peak of the $LiNbO_3$

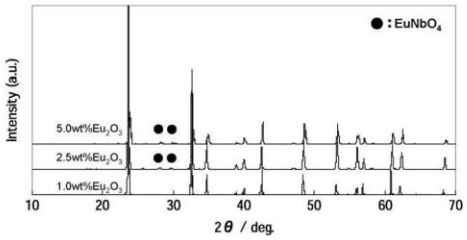

Fig. 2. XRD patterns of LN:Eu. Eu_2O_3 contents are 1.0, 2.5 and 5.0 wt.%.

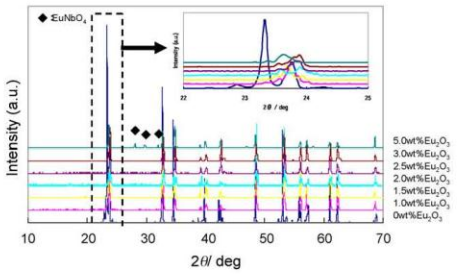

Fig. 3. XRD patterns of LNT:Eu solid solution (10 mol.% TiO_2) added various contents of Eu_2O_3. Focused patterns of $2\theta = 22–25°$ was inserted. Diamond symbol showed $EuNbO_4$.

structure at around $2\theta = 23$, where the peak can be resolved into 4 components. Increasing separation of the split peaks relates to a decrease in the super-periodicity of the LNT solid solution. The insert in Fig. 3 shows a close up of this region of the spectra. It can be seen that the LNT sample with no Eu shows peak splitting, but this is not observed in the Eu doped samples, indicating that the superstructure formation was obstructed by Eu doping.

It is thought that the Eu doping decreases the Ti diffusion rate and inhibits the introduction of the stacking faults. This is confirmed from structural observations by HREM and an analysis of distribution of Eu and Ti by TEM-EDS. The 10 mol.% TiO_2 LNT solid solutions with 0 and 2.5 wt.% Eu doping are shown in Fig. 3. It was observed that LNT solid solution with no Eu doping (Fig. 4a) had a periodic structure whereas the Eu doped sample (Fig. 4b), contained stacking faults that were discontinuous resulting in a loss of periodicity. The results of TEM-EDS analysis shown in Table 1 show that Ti and Eu elements are concentrated more in the stacking faults than in the $LiNbO_3$-like subcell. It is thought that Eu doping results in the destruction of the rock-salt structure of the stacking faults.

The luminescence of the LNT solid solutions with Eu as activator were measured by excitation at $\lambda = 380$ nm. The emission spectra presented in Fig 5a show that the main emission peak of Eu doped LNT solid solutions was at $\lambda = 625$ nm. An additional peak

Table 1
Compositions of LNT:Eu solid solution (10 mol.% TiO_2) analyzed by TEM-EDS.

	Additive		Non-additive
	Subcell	Stacking faults	Subcell + stacking faults
Nb	91.78	87.99	92.17
Ti	6.10	9.23	7.83
Eu	2.12	2.77	0.00

Atom%.

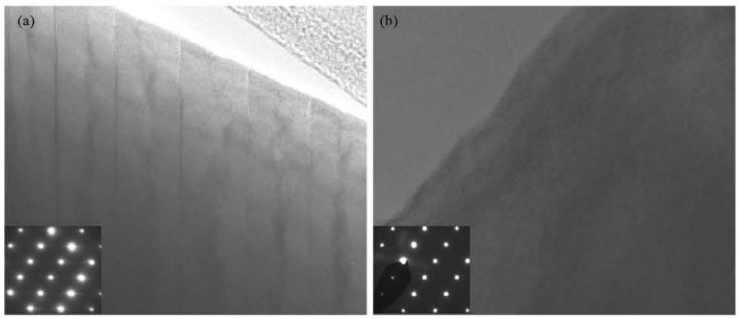

Fig. 4. (a) High-resolution TEM photograph and electron diffraction pattern of LNT solid solution (10 mol.% TiO_2). (b) High-resolution TEM photograph and electron diffraction pattern of Eu doped LNT solid solution (10 mol.% TiO_2).

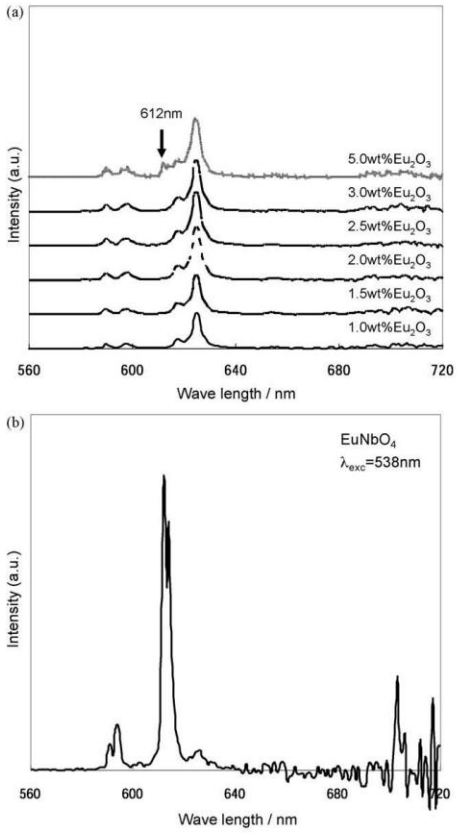

Fig. 5. (a) Relationship between emission spectrum excited by λ = 380 nm and Eu_2O_3 content for LNT:Eu solid solution (TiO_2 = 10 mol.%). (b) Emission spectra of $EuNbO_4$ (excited by λ = 538 nm).

at λ = 612 nm was observed only for the sample doped with 5 wt.% Eu_2O_3. Fig. 5b shows the emission spectra of pure $EuNbO_4$ where it can be seen that this peak is associated with the $EuNbO_4$ phase. The emission spectra results therefore support the XRD results where the $EuNbO_4$ phase was observed only for the 5 wt.% Eu doped sample.

Fig. 6a shows the excitation spectra of the Eu doped LNT solid solutions. All of the spectra show three absorption peaks at λ = 398 nm, 468 nm and 541 nm. For Eu contents up to 3%, which all emitted at λ = 625 nm the intensity of the 398 nm excitation peak showed the highest intensity. The 5 wt.% Eu_2O_3 doped LNT solid solutions showed two different spectra. The $EuNbO_4$ as a secondary phase was identified by XRD, and the luminescence of this $EuNbO_4$ was observed. For the 5% doped sample which emitted at λ = 612 nm, the strongest absorption peak was the one at λ = 538 nm. This is again related to the presence of the $EuNbO_4$ phase as indicated by Fig. 6b which shows excitation spectra for $EuNbO_4$. When the samples were excited at λ = 398 nm there was no difference in the emission spectra of the samples with different Eu contents as shown in Fig. 7. The luminescence intensity of LNT samples with different amounts of Eu additive when changing the TiO_2 content (varying composition of LNT solid solutions) is shown in Fig. 8 These samples were excited at λ = 398 nm. The luminescence intensities of LNT solid solutions:Eu were higher than that of LN:Eu, and for all Eu contents the maximum intensity was observed at 10 mol.% TiO_2. For LN:Eu samples the highest intensity was observed for the 2.0 wt.% Eu sample, and for the LNT:Eu samples the highest intensity was obtained with 2.5 wt.% doping. The relationship between the compositions and emission spectra of the LNT:Eu 2.5 wt.% is given in Fig. 9. For TiO_2 contents up to 10 mol.% there is a clear separation of peaks at λ = 618 nm and λ = 625 nm. For higher TiO_2 contents there was broadening of the peak at λ = 618 nm until it becomes absorbed by the peak at λ = 625 nm. It is thought that this is due to a change in the electron state associated with the change in crystal structure symmetry.

Comparing the luminescence of LNT:Eu phosphor with commercial phosphors of blue, green and yellow were shown in Fig. 10. It was thought Eu doped LNT phosphor prepared in this work was adapted to a phosphor for a white LED.

4. Summary

Eu doped $LiNbO_3$ and Eu doped LNT solid solutions were prepared and it was found that for small amounts of a $LiNbO_3$ type structure was observed. For the LN materials, Eu_2O_3 amounts greater than 2.0 wt.%, resulted in a secondary $EuNbO_4$ phase whilst

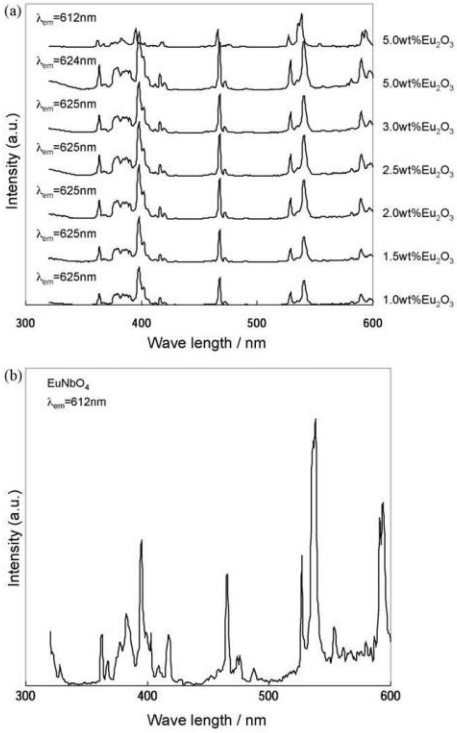

Fig. 6. (a) Variation of excitation spectrum of LNT:Eu solid solution (TiO_2 = 10 mol.%) for Eu_2O_3 contents. (b) Emission spectra of $EuNbO_4$ (emission by λ = 612 nm).

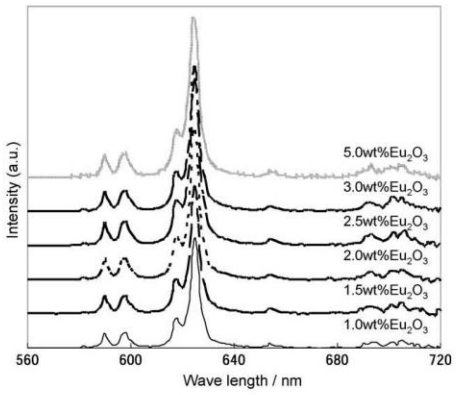

Fig. 7. Relationship between emission spectrum excited by λ = 398 nm and Eu_2O_3 content.

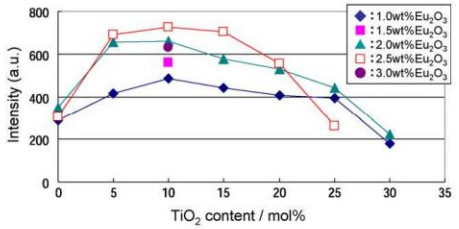

Fig. 8. Relationship between TiO_2 content of LNT:Eu solid solutions and photoluminescence intensity.

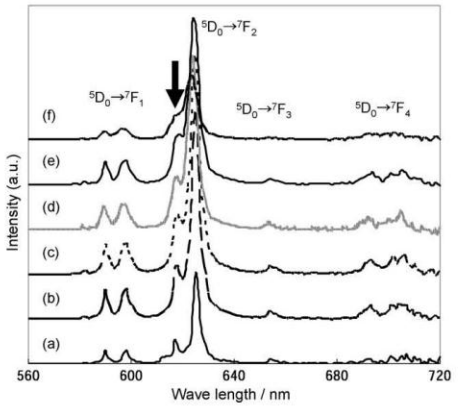

Fig. 9. Emission spectrum excited by λ = 398 nm of LNT:Eu solid solutions. Eu_2O_3 was added at 2.5 wt.%. TiO_2 content is (a) 0 mol.%, (b) 5 mol.%, (c) 10 mol.%, (d) 15 mol.%, (e) 20 mol.% and (f) 25 mol.%.

in the LNT solid solutions this was not observed for Eu_2O_3 amounts up to 3.0 wt.%. This suggests that solubility of Eu is greater in the LNT compositions. When TiO_2 and Eu_2O_3 were added to $LiNbO_3$, the luminescence intensity of the solid solutions markedly improved over that of the LN:Eu. In terms of luminescence intensity it was observed that the most suitable Eu additive density was 2.0 wt.% in $LiNbO_3$ and 2.5 wt.% in the LNT solid solutions, and it was confirmed

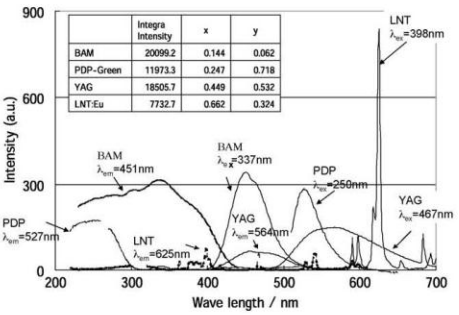

Fig. 10. The emission and excitation spectra of LNT:Eu and commercial phosphors. BAM: blue, Green: green and YAG: yellow.

that the intensity of LNT solid solutions was twice as large as that of $LiNbO_3$. In LNT solid solutions, the most suitable TiO_2 content was 10 mol.%. LNT solid solutions with 10 mol.% TiO_2 usually have a superstructure, but it was discovered that Eu doping prevented the formation of such a superstructure in LNT solid solutions. XRD measurements showed that no such structure was observed in the Eu doped LNT solid solution at the same level of TiO_2, and the destruction of the periodicity of the M Phase superstructure was confirmed by HREM. It is concluded that the increase in luminescence intensity does not arise from the superstructure, but is related to the most suitable density of Ti and Eu in the LNT solid solutions.

Acknowledgement

The authors gratefully acknowledge Dr. Mark I. Jones (Auckland University, New Zealand) for helpful discussions and for checking the manuscript, and Mr. Mutsuo Masuda (KRI Inc.) for helpful advice on emission characteristics.

References

[1] M.E. Villafuerte-Castrejon, J.A. Gracia, E. Cisneros, R. Valenzuela, A.R. West, Trans. J. Brit. Ceram. Soc. 83 (1984) 143.
[2] M.E. Villafuerte-Castrejon, A. Aragon-Pina, R. Valenzuela, A.R. West, J. Solid State Ceram. 71 (1987) 103.
[3] R.I. Smith, A.R. West, Mater. Res. Bull. 27 (1992) 277.
[4] H. Hayashi, H. Nakano, K. Suzumura, K. Urabe, A.R. West, Forth Ceram. Soc. 2 (1995) 391.
[5] H. Hayashi, K. Urabe, K. Niihara, Key Eng. Mater. 161–163 (1999) 501.
[6] H. Koinuma, Y. Matsumoto, Y. Shimomura, N. Kujima, JP 3,582,010 B2 (2004).
[7] A.Y. Borisevich, S.V. Kalinin, D.A. Bonnell, P.K. Davies, J. Mater. Res. 16 (2001) 329.
[8] A.Y. Borisevich, P.K. Davies, J. Am. Ceram. Soc. 85 (2002) 573.
[9] Y. Yamamoto, H. Hayashi, T. Sekino, T. Nakayama, T. Kondo, M. Wada, T. Adachi, K. Niihara, Mater. Res. Innovations 7 (2003) 74–79.
[10] A.A. Kaplyanskii, S. Kapphan, A.B. Kutsenko, K. Polgar, A.P. Skvortsov, Tech. Phys. Lett. 33 (2007) 337.
[11] L.A. Souza, Y. Messaddeq, S.J.L. Ribeiro, C. Fredericci, F. Lanciotti Jr., P.S. Pizani, Quim. Nova 25 (2002) 1067.
[12] Y. Yamamoto, T. Sekino, H. Hayashi, T. Nakayama, T. Kusunose, K. Niihara, Mater. Lett. 57 (2003) 2702.
[13] Y. Yamamoto, T. Sekino, H.T. Kusunose, T. Nakayama, K. Niihara, Mater. Integr. 17 (2004) 10.

Journal of the Ceramic Society of Japan 118 [3] 226-230 2010 Paper

Microstructure and luminescence of Eu-doped $Li_{1+x-y}Nb_{1-x-3y}Ti_{x+4y}O_3$ solid solutions with superstructure

Hiroyuki HAYASHI,† Hiromi NAKANO* and Mark I JONES**

KRI, Inc. Device Process Unit, Nano-Device Research Laboratory, Kyoto research Park, 134, Chudoji Minami-machi, Shimogyo-ku, Kyoto 600-8813
***Cooperative Research Facility Center, Toyohashi University of Technology, 1-1, Hibarigaoka Tempaku, Toyohashi 441-8580**
****Dept of Chemical & Materials Engineering, University of Auckland, Private Bag 92019, Auckland, New Zealand**

Eu doped Li–Nb–Ti oxide (LNT) solid solutions were prepared by heating mixed powders at temperatures of 1120°C for up to 24 h. Despite the fact that these materials often possess a crystallographic superstructure, no such structure was observed for a sintering time of 10 h. For the longer sintering period of 24 h, no superstructure was observed for samples with less additions of TiO_2, but it was confirmed by X-ray diffraction and a High-Resolution Transmission Electron Microscopy that samples with compositions containing 20 and 25 mol%-TiO_2 did possess superstructures. Heating for 24 h resulted in an improvement of the photoluminescence (PL) intensity of the LNT solid solutions, and this increase was more marked in the samples where the superstructure was developed. For the Eu-doped LNT solid solution containing 25 mol%-TiO_2, the PL intensity of the sample with the superstructure was almost 3 times as high as that of a sample with the same doping but without the superstructure.

Key-words : $LiNbO_3$, TiO_2, Superstructure, Eu_2O_3, Phospher

[Received September 28, 2009; Accepted January 15, 2010]

1. Introduction

$Li_{1+x+y}Nb_{1-x-3y}Ti_{x+4y}O_3$ ($0.11 \le x \le 0.33$, $0 \le y \le 0.09$) (hereafter LNT) forms solid solutions with a superstructure, known as the M Phase, in the Li_2O–Nb_2O_5–TiO_2 ternary system. Since the discovery of this M Phase by Villafuerte-Castrejon et al.,[1,2] both its crystal structure[3)–6)] and the applications of M Phase[7)–9)] have been studied. LNT solid solutions of M Phase have an hexagonal subcell similar to the unit cell of $LiNbO_3$, which belongs to the trigonal system ($R3c$), and has lattice constants of $a = 0.5148$ nm and $c = 1.3863$ nm. The superstructure of LNT solid solutions has been identified via High-resolution Transmission Electron Microscopy (HREM) studies as having layer-like domains.[4),5)] where stacking faults are inserted parallel to the c axis in the $LiNbO_3$ structure. These stacking faults have a rock-salt structure and the dimension of the domain along the c axis based on a $LiNbO_3$-like subcell has been controlled by TiO_2 content and sintering temperature.[5)] The period of the superstructure has been shown to decrease with increasing TiO_2 content.

The photoluminescence of Eu doped LNT solid solutions, with an optimum Eu content of 2.5 wt% and heated at 1120°C for 10 h, has been shown to be significantly higher than comparable $LiNbO_3$:Eu materials.[10)] However, it was also shown that doping with Eu prevented the formation of the superstructure. The purpose of this study was to clarify the relationship between photoluminescence and superstructure of Eu doped LNT solid solutions.

2. Experimental procedure

The starting materials were Li_2CO_3 (Wako Pure Chemical Industries, Ltd.), Nb_2O_5 (Wako Pure Chemical Industries, Ltd., 3N), TiO_2 (Wako Pure Chemical Industries, Ltd.) and Eu_2O_3 (Wako Pure Chemical Industries, Ltd., 3N). The compositions of the LNT:Eu solid solutions prepared in this work followed the general formula $Li_{1+x+y}Nb_{1-x-3y}Ti_{x+4y}O_3$ with $0 \le x \le 0.33$ and $y = 0$. Doping was carried out by the addition of 2.5 wt% Eu_2O_3 to the starting powder and the TiO_2 content of the samples was varied between 5 and 25 mol%. The powders were blended using dry mixing, and then heated in air at 1000°C for 3 h followed by heating at 1120°C for either 10 or 24 h.

Excitation and emission spectra of the sintered samples was measured by a spectrometer FP–6500 model (JASCO). Phase analysis was carried out by X-ray Diffraction (XRD) over a 2θ range of 10 to 70° with a step size of 0.01° using a RINT2500 (Rigaku Co.) operating at 50 kV and 200 mA Structural images and selected area electron diffraction patterns (SAED) were observed by HREM (JEM–3000F, JEOL Ltd.) at 300 kV. The use of the HREM allowed chemical composition analysis with an electron probe width of 0.4 nm, and with sufficiently high current for point analysis by energy dispersive X-ray spectroscopy (EDS) (Noran Instruments Voyager III).

3. Results and discussions

Figure 1 shows the XRD spectra of all samples heated for 24 h. The materials showed a crystal structure similar to the $LiNbO_3$ type unit cell. No $EuNbO_4$ was observed in any of the samples with the exception of the one containing 25 mol% TiO_2. The superstructure normally observed in LNT solid solutions can be observed as a splitting of the (012) peak of the $LiNbO_3$ structure at a 2θ angle of approximately 23°, where the peak splitting can be resolved in to 4 individual components. No such superstructure was observed for Eu doped LNT solid solutions with TiO_2 concentrations of 10 and 15 mol% whereas samples with 20 and 25 mol% TiO_2 did show a superstructure. The variation in the

† Corresponding author: H. Hayashi; E-mail: h-hayasi@kri-inc.jp

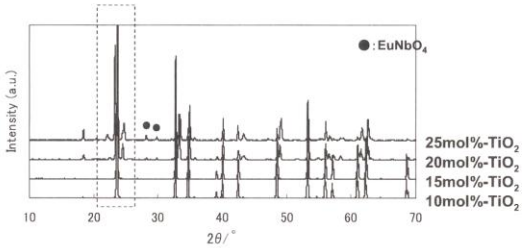

Fig. 1. XRD patterns of Eu doped LNT solid solutions. The peak of each sample in a square by broken line show the (012) peak of $LiNbO_3$.

(012) peak for the samples with both 10 and 25 mol% TiO_2 content and for different holding times at temperature is shown in **Fig. 2**. For the sample with a TiO_2 content of 10 mol%, the (012) peak became sharper with increasing holding time but there was no peak splitting to indicate the presence of the superstructure. On the other hand, for the high TiO_2 content sample, peak splitting was observed and the distance between the split peaks increased with increasing holding time. However, the splitting was not at regular intervals, suggesting that the periodicity of the superstructure was random.

The variation in unit cell volume with holding time for LNT:Eu solid solution samples containing 5, 10 and 25 mol% TiO_2 is shown in **Fig. 3**. There was an increase in unit cell volume for all samples with increasing holding time. **Table 1** shows the expansion coefficient determined for these samples. The observed expansion is attributed to the incorporation of the Eu ions in to the solid solution, which have a larger ionic radius than the Li, Nb and Ti elements and lead to the larger unit cell parameters.

LNT solid solutions with a superstructure show a plate-like crystal morphology as depicted schematically in **Fig. 4** where the *a* and *c*-axes lie parallel and perpendicular to the plate respectively. SEM images of samples containing 10 and 20 mol% TiO_2 are shown in **Fig. 5** and **Fig. 6** respectively. For the 10 mol% TiO_2 sample, grain growth was observed with an increase in holding time from 10 to 24 h, and the plate-like morphology was clearly observed for the sample held at temperature for 24 h. For the 20 mol% TiO_2 sample, the plate-like morphology was devel-

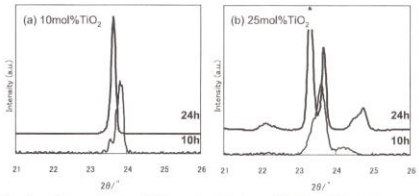

Fig. 2. Focused in the (012) peak of Eu doped LNT solid solutions sintered for10 and 24 h. TiO_2 content is (a) 10 mol% and (b) 25 mol%.

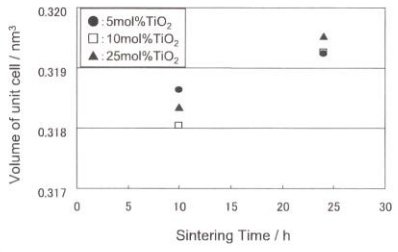

Fig. 3. Relationship of between volume of unit cell of LNT solid solutions and sintering time.

Table 1. Expansion Coefficient of the Unit Cell of LNT:Eu Solid Solutions

TiO_2 content (mol%)	Cubical expansion coefficient (%)
5	0.18
10	0.38
25	0.37

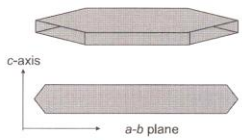

Fig. 4. Schematic of LNT solid solutions with superstructure shows a plate crystal. The perpendicular of the plate is *c*-axis and the parallel of the plate is *a*-axis.

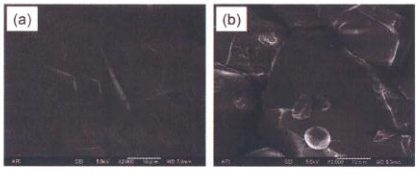

Fig. 5. SEM images of 2.5 wt% Eu_2O_3 doped 10 mol%-TiO_2 LNT solid solution. (a) sintered for 10 h and (b) sintered for 24 h.

oped but such extensive grain growth was not observed.

Low-magnification TEM images and SAED patterns for the [010] zone axis of samples with 20 mol% TiO_2 content with and without Eu_2O_3 doping are shown in **Fig. 7**. The superstructure was clearly observed for both samples, along with satellite diffraction along the c^* axis which was clearly observed in the electron diffraction pattern of the no-doped LNT sample. The distance between the intergrowth layers of the LNT:Eu sample was greater than that in the LNT solid solution with no doping. TEM micrographs and SAED patterns for the [010] zone axis of the Eu-doped LNT solid solutions with 10 and 25 mol% TiO_2 are shown in **Fig. 8**. For the sample with 10 mol% TiO_2, no satellite diffraction or superstructure were observed. These features were observable for the sample with 25 mol% TiO_2, although the satellite diffraction was not clear, but rather was observed as streaky lines. This indicates a loss in periodicity of the intergrowth layers of the superstructure, which can also be observed in the HREM image as a change in the spacing of the layers. These results are in agreement with the XRD and SAED patterns. Furthermore, the Eu was uniformly distributed within the crystalline LNT grains and no segregation of Eu was observed (**Fig. 9**).

A schematic of the formation mechanism of the structure of these materials is shown in **Fig. 10**. For the samples with no Eu

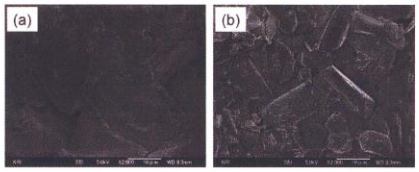

Fig. 6. SEM images of 2.5 wt% Eu_2O_3 doped 20 mol%-TiO_2 LNT solid solution. (a) sintered for 10 h and (b) sintered for 24 h.

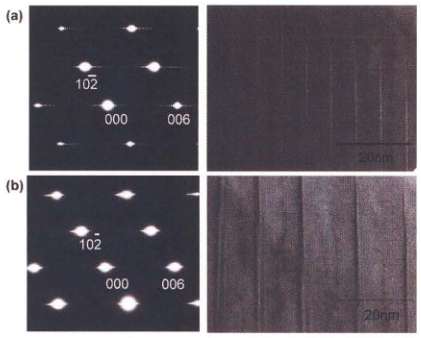

Fig. 7. (a) TEM image and SAED pattern of no-doped 25 mol%-TiO_2 LNT solid solution. Zone axis is [010]. (b) TEM image and SAED pattern of 2.5 wt% Eu_2O_3 doped 25 mol%-TiO_2 LNT solid solution. Zone axis is [010].

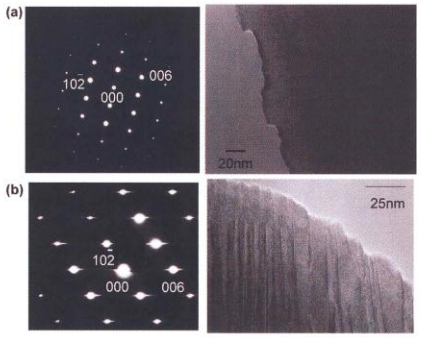

Fig. 8. (a) TEM image and SAED pattern of 2.5 wt% Eu_2O_3 doped 10 mol%-TiO_2 LNT solid solution. Zone axis is [010]. (b) TEM image and SAED pattern of 2.5 wt% Eu_2O_3 doped 25 mol%-TiO_2 LNT solid solution. Zone axis is [010].

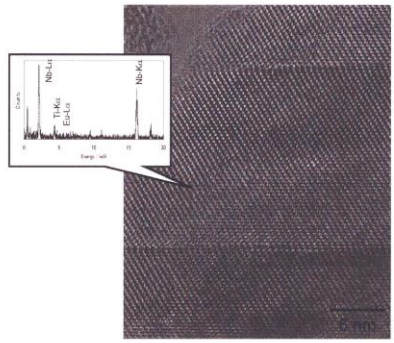

Fig. 9. High resolution TEM image and EDS analysis of Eu-doped 25 mol%TiO_2 LNT solid solution.

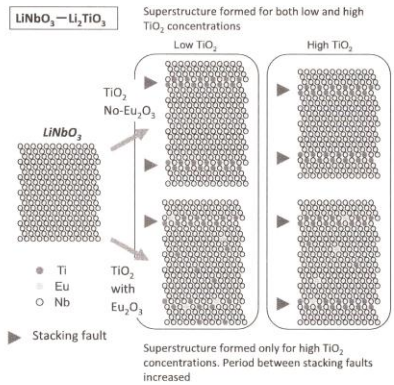

Fig. 10. A schematic of the formation mechanism of the structure of LNT:Eu solid solitions.

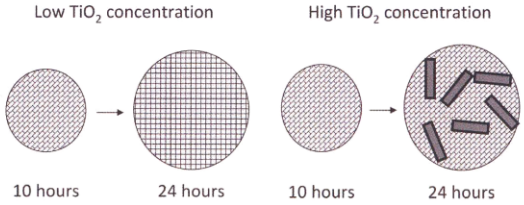

Fig. 11. Schematic showing the effect of TiO_2 content on the grain growth and superstructure formation. For low TiO_2 contents, no superstructure is formed and grain growth occurs for longer sintering times. For higher TiO_2 contents, the formation of the superstructure inhibits the grain growth.

doping, the superstructure is observed in the LNT samples at all levels of TiO_2 doping. However,it is thought that the Eu doping makes the diffusion of Ti more difficult and in Eu doped samples with low TiO_2 concentrations the diffusion was insufficient for the development of the superstructure. For higher TiO_2 concentrations, there is sufficient TiO_2 for the superstructure to form but the slow diffusion means that at 10 h holding it was not well developed. The improved diffusion at the longer holding time means that the development of the superstructure was enhanced. It is thought that the differences in the development of the superstructure with TiO_2 content results in the differences observed in grain growth that were shown in Fig. 10. For samples with low TiO_2 concentrations, the superstructure is not formed and the grains simply grow larger with holding time due to grain growth. For the samples with higher TiO_2 concentrations the formation of the superstructure inhibits the grain growth, as shown schematically in **Fig. 11**

The variation in the photoluminescence intensity (PL) of the Eu doped LNT solid solutions as a function of TiO_2 content, and for different holding times, is shown in **Fig. 12**. This figure represents the intensity of the 625 nm peak excited at 398 nm. The PL intensity of $LiNbO_3$:Eu (2.5 wt%) is also shown for comparison (0% TiO_2 data). The PL intensity of $LiNbO_3$:Eu decreased with increasing holding time. The solid solubility limit of Eu in $LiNbO_3$ is lower than that for LNT solid solutions[10] and for the longer holding time the formation of $EuNbO_4$ in $LiNbO_3$:Eu was observed, and photo luminescence of $EuNbO_4$ was seen. In the samples held at temperature for 24 h, it was thought that the PL intensity of the $LiNbO_3$:Eu decreased with increasing photoluminescence of the $EuNbO_4$.

For the Eu doped LNT samples, both holding times showed the same trend with the highest PL intensity being observed for samples with 10 mol% TiO_2 and decreasing with further increases of TiO_2. For all TiO_2 contents, the samples held for 24 h showed higher PL intensity than those held for 10 h. This difference in intensity between the samples held for periods of 10 and 24 h was more marked in samples with higher TiO_2 concentrations.

The emission spectra of the samples excited at 398 nm are shown in **Fig. 13**. There was no real change in the spectra as a function of holding time for either the 10 or the 25 mol% TiO_2 samples. However, the emission spectra of the samples did depend on the composition. For higher TiO_2 concentrations there was broadening of the peak at $\lambda = 618$ nm until it becomes absorbed by the peak at $\lambda = 625$ nm. It is thought that this is due to a change in the electron state associated with the change in crystal structure symmetry.[10]

The highest PL intensity observed for the 10 mol% TiO_2 LNT samples is thought to be related to the grain growth observed in

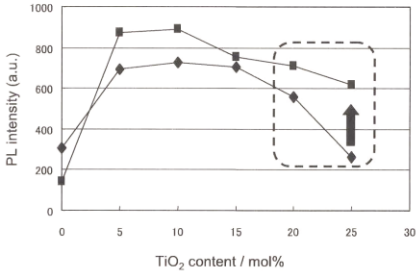

Fig. 12. Relationship between TiO_2 content and PL intensity of Eu doped LNT solid solutions. ◆:sintered for 10 h and ■:sintered for 24 h.

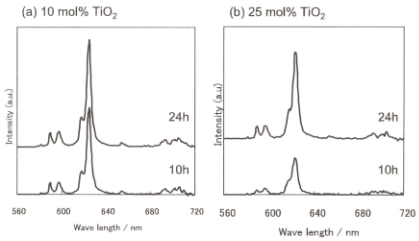

Fig. 13. Emission spectra excited by 398 nm of Eu doped LNT solid solutions. TiO_2 content is (a) 10 mol% and (b) 25 mol%.

those samples. The low PL intensity of the 20 and 25 mol% TiO_2 LNT solid solutions held for 10 h is thought to be causally related to a concentration quenching phenomenon. When heating at 1120°C for 24 h, it is thought that the distribution of Eu and Ti, and the relative distance between them, were optimized by the formation of the superstructure, and that this resulted in the increase in the PL intensity of these samples when compared to samples held for shorter periods.

4. Summary

The luminescence and microstructure of Eu doped LNT solid solutions prepared by heating at 1120°C for up to 24 h and with varying amounts of TiO_2 doping have been evaluated, and it was shown that for low TiO_2 concentrations, no superstructure was

observed in the solid solutions. This is attributed to insufficient Ti and slow diffusion caused by the presence of the Eu. Increasing the holding time for these samples had no effect on the superstructure formation. Samples with higher TiO_2 contents also exhibited no superstructure when held for 10 h, but with an increase in holding time, the 20 and 25 mol% TiO_2 content LNT solid solutions were shown to possess a superstructure as confirmed by XRD and TEM.

The highest PL intensity was observed for samples containing 10% TiO_2, and this is attributed to the grain growth observed in those samples. The PL intensity of the Eu doped LNT solid solutions decreased for samples containing higher TiO_2 concentrations. However, for these samples the PL intensity was improved by increasing the holding time. In particular, for those samples that possessed superstructures (20 and 25 mol% TiO_2 concentrations) the PL intensity showed a significant increase over comparable samples where no superstructure was observed when the holding time at temperature was increased from 10 to 24 h.

Acknowledgement The authors gratefully acknowledge Mr. Mutsuo Masuda (KRI Inc.) for helpful advice on emission characteristics.

References

1) M. E. Villafuerte-Castrejon, J. A. Gracia, E. Cisneros, R. Valenzuela and A. R. West, *Trans. J. Brit. Ceram. Soc.*, **83**, 143 (1984).
2) M. E. Villafuerte-Castrejon, A. Aragon-Pina, R. Valenzuela and A. R. West, *J. Solid State Ceram.*, **71**, 103 (1987).
3) R. I. Smith and A. R. West, *Mater. Res. Bull.*, **27**, 277 (1992).
4) H. Hayashi, H. Nakano, K. Suzumura, K. Urabe and A. R. West, *Forth Ceram. Soc.*, **2**, 391 (1995).
5) H. Hayashi, K. Urabe and K. Niihara, *Key Eng. Mater.*, **161–163**, 501 (1999).
6) H. Koinuma, Y. Matsumoto, Y. Shimomura and N. Kujima, JP 3582010 B2, (2004).
7) A. Y. Borisevich, S. V. Kalinin, D. A. Bonnell and P. K. Davies, *J. Mater. Res.*, **16**, 329 (2001).
8) A. Y. Borisevich and P. K. Davies, *J. Am. Ceram. Soc.*, **85**, 573 (2002).
9) Y. Yamamoto, H. Hayashi, T. Sekino, T. Nakayama, T. Kondo, M. Wada, T. Adachi and K. Niihara, *Mater. Res. Innov.*, **7**, 74–79 (2003).
10) H. Hayashi and H. Nakano, *J. Alloy Compod.* (accepted).

高温 TEM その場観察によるダイナミクス的考察に関連する研究成果

Journal of the Ceramic Society of Japan 119 [1] 1-7 2011 Special Article
The 64th CerSJ Awards for Academic Achievements in Ceramic Science and Technology: Review

Microstructural evolution by in-situ TEM observations of oxides

Hiromi NAKANO†

Cooperative Research Facility Center, Toyohashi University of Technology, 1–1 Tenpaku, Toyohashi, Aichi 441–8580

In-situ observations using high-temperature transmission electron microscopy (TEM) is a promising technique for obtaining new findings and developing phenomenological theory for ceramic materials at high temperatures. By observing the changes in hydrothermal $BaTiO_3$ due to heating, we clarify the vanishing mechanism of internal pores and the mechanism of $BaCO_3$ phase generation/vanishing at high temperatures. Through observations of the grain growth of $BaTiO_3$ prepared by radio-frequency plasma chemical vapor deposition, we calculate the grain-boundary diffusion coefficient, which is an important parameter controlling the sinterability of ceramics. Observations of the shrinkage and disappearance of $Ba_5Nb_4O_{15}$, as well as simulations, indicate that high energy and low diffusivity at the grain boundary make grains vanish while maintaining a truncated spherical shape. Finally, observations of the structural changes in layered perovskite $BaLn_2Mn_2O_7$ (Ln = Gd, Pr, Eu) reveal a first-order phase transition that has not been previously reported.

Key-words : TEM, In-situ observation, Grain growth, Phase transition, Microstructure

[Received July 26, 2010; Accepted October 8, 2010]

1. Introduction

As part of ongoing advances in nanotechnology, the transmission electron microscope (TEM) has come to play an important role in the control of material properties and the design of new materials in the field of ceramics.[1] This is because the bulk characteristics of ceramic materials are influenced by material structure at the atomic level, which drives the need for information obtained by atomic-level analysis.[2) 5)] Here, in-situ observation using high-temperature transmission electron microscopy is one technique for obtaining new findings and developing phenomenological theory for ceramic materials at high temperatures. In this way, diverse phenomena such as structural changes at high temperatures and grain growth behavior on a nanoscale can be clarified, and by merging observational and theoretical results, highly original information can be disseminated. This paper reports on new findings obtained by in-situ observations of several oxides. The knowledge obtained here is expected to be useful in the design of future materials.

2. Experimental procedure for in-situ TEM observations

The in-situ TEM observations were performed using a thermal specimen holder. A two-axis tilting thermal holder was used in the temperature range from 293 to 1073 K (JEM-2000EX, EM-SHU2 specimen holder, JEOL). A single-axis tilting thermal holder was used in the temperature range from 293 to 1203 K (EM-SHH4). The temperature was controlled manually, and TEM images were recorded in real time using a video system.

3. Results and discussion

3.1 Changes in internal pores and surface layer of $BaTiO_3$ prepared by hydrothermal synthesis

$BaTiO_3$ powders prepared by the hydrothermal synthesis technique are very fine and not agglomerated. The formation mechanisms and properties of the hydrothermal $BaTiO_3$ have been investigated.[6) 10)] The powders contain OH^- ions or H_2O in the lattice. Therefore, rectangular defects are often observed in the particles which was formed by the dissociation of hydroxyl ions by annealing, and their sizes increase with an increase in the annealing temperature.[11)] These behaviors, however, have not been sufficiently characterized.

We focused on the thermal behavior of the internal pores in $BaTiO_3$ powders prepared by hydrothermal synthesis. The as-received $BaTiO_3$ used was BT-006 (Sakai Kagaku Co., Osaka, Japan).[10)] The BT-006 particle size was found to be 60 nm by rough measurement.[12)] Some particles had internal pores of various sizes, and such internal pores are not lattice defects at the atomic scale because their sizes are a few tens of nanometers. The presence of the pores affects the particle's density. The particle's density increases with increasing temperature and reaches a theoretical value above 1173 K, as reported by Ikawa et al.[13)]

We successfully observed in-situ the change in the internal pore resulting from annealing for about 4 h on a thermal stage in the TEM. The temperature of the thermal stage was controlled manually, and its profile was recorded and then plotted against time.[12)] **Figure 1** shows TEM images of $BaTiO_3$ particles at various annealing temperatures on the thermal stage. Above 573 K, an amorphous layer started to appear around the particle's surface as indicated by the arrows in Fig. 1(b). The annealing temperature was continuously increased to 973 K, and the internal pore opened out. The temperature was kept at 1128 K for 30 min in the period shown in (d)–(f), and the pore disappeared completely from the $BaTiO_3$ particle. At 1193 K, small grains indicated by arrows 1 and 2 merged with the observed large particle. Here, we see that the amorphous layer disappeared from the particle's surface at 1193 K. The temperature was kept at 1193 K for 90 min, and then the specimen's temperature was further increased to 1203 K. A facet formed on the particle's surface [Fig. 1(h)] by the movement of the surface's atomic layer. After cooling, no amorphous layer was found on the particle's surface. The composition of the thin amorphous layer [Fig. 1(b)] could not be identified at this experimental stage, but the same type of amorphous layer,

† Corresponding author: H. Nakano; E-mail: hiromi@crfc.tut.ac.jp

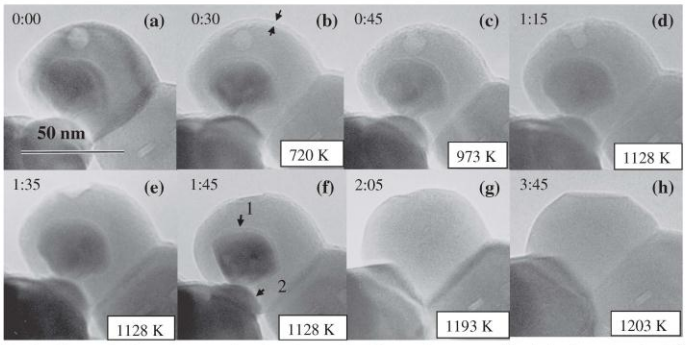

Fig. 1. Changes in internal pores and surface layer of $BaTiO_3$ powders prepared by hydrothermal synthesis.[12)]

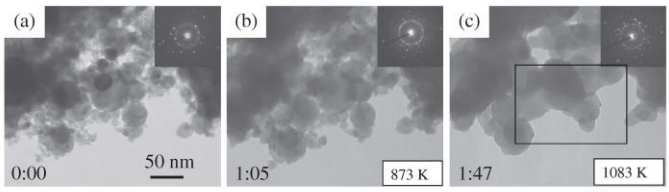

Fig. 2. Grain growth in $BaTiO_3$ powders synthesized by RF-plasma CVD method.[20)]

$BaCO_3$, has usually been observed on the $BaTiO_3$ particle's surface.[14)] The reaction that took place on the surfaces of the $BaCO_3$ particles was estimated to be $BaTiO_3 + x(H_2O + CO_2) = (Ba_{1-x}\ H_{2x})TiO_3 + xBaCO_3$.[14)] The surface's atom reacts easily with the H_2O and CO_2, and consequently a Ba^{2+} vacant site is formed. Actually, the $BaTiO_3$ powder in a container changes in color to yellowish-white when it is stored in a humid atmosphere for a few weeks, a phenomenon that might reflect the formation of the vacant sites. Accordingly, this observed amorphous phase in Figs. 1(b)–1(f) was also formed by the reaction between the surface's atom and the decomposed gases, H_2O and CO_2, during heating.[7)] The thin layer was decomposed at 1193 K, the point at which one part reacts with the $BaTiO_3$ grain and the other part is removed from the surface of the grains as a vapor phase.[12),15)] This observation result provides the information needed to understand the physical properties of the $BaTiO_3$. The relationship between the thickness of the surface layer and the dielectric property of the $BaTiO_3$ particle has been discussed.[16),17)] The thermal behaviors and properties of the $BaTiO_3$ particle depend closely on the synthesis process.[9),10),18)]

3.2 Grain growth mechanism of $BaTiO_3$ prepared by plasma chemical vapor deposition

Fine-grained and well-crystallized $BaTiO_3$ is required in the electronics industry. Well-crystallized $BaTiO_3$ nanoparticles were synthesized by the radio-frequency plasma (RF-plasma) chemical vapor deposition (CVD) method.[19)] The particle sizes ranged from 10 to 50 nm in diameter, and no internal pore was observed, unlike hydrothermally synthesized $BaTiO_3$ particles. The gas-desorption behavior and weight loss of the $BaTiO_3$ powder were characterized in a previous paper by TDS and TG measurements, respectively, in a heat range from room temperature to 1273 K.[20)]

We made in-situ TEM observations of the grain growth behavior of the $BaTiO_3$ nano-particles using a thermal holder. The migration rate was measured using video images, and the grain boundary diffusion coefficient was calculated around 1083 K. The temperature of the specimen was increased from room temperature at a heating rate of about 9 K/min and maintained at 1083 K for 20 min. **Figure 2** shows the changes in the $BaTiO_3$ particles by heating from room temperature to 1083 K. The consecutive images are recorded by video, as are a part of the fragmentary images. No remarkable grain growth occurred below 873 K. However, the selected area electron diffraction (SAED) patterns shown in the insets revealed that the degree of crystallinity increased with an increase in temperature up to 873 K. Around 1083 K, grain growth started, and small particles of 40–60 nm in diameter merged into large particles. This phenomenon is an initial stage of normal grain growth, which means that grain boundaries moved as a consequence of many individual atomic jumps across the plane of the boundary.[21)] The grain boundary diffusion coefficient (D_{gb}) is calculated by applying the migration rate across the grain boundary (v m/s) to the following equations:[22)]

$$v = D_{gb}\Delta F/(\lambda RT) = 2D_{gb}\gamma V/(\lambda RTr) \quad (1)$$

$$\Delta F = 2\gamma V/r \quad (2)$$

Here, ΔF is total free energy (J/mol) on the boundary, R is a gas constant, T is the temperature, and λ is the boundary thickness. V is molecular volume, and γ is boundary energy (J/m^2) estimated at roughly $1\ J/m^2$. In our experiment, the migration rate (v) and curvature ($2/r$) were determined from the movement of some particles by the series of thermal TEM images recorded by the video system. The grain boundary diffusion coefficient (D_{gb}) values were derived from the movements of $BaTiO_3$ nano-

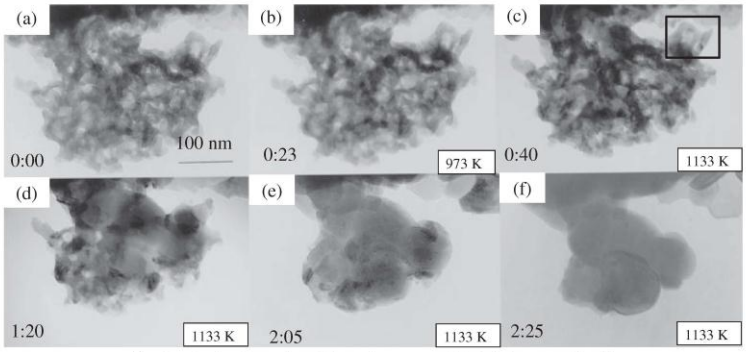

Fig. 3. In-situ observation of formation process of $Ba_5Nb_4O_{15}$ crystalline.[27]

particles of 40–60 nm in diameter at 1083 K. Kusunoki et al.[22),23)] determined the D_{gb} of ZrO_2, of about 30 nm in diameter, at 1473 K from thermal TEM images by a similar method. The average value of D_{gb} at 1083 K was calculated to be 4.39×10^{-18} m^2/s, and this value was nearly comparable with that of a ZrO_2 nanoparticle at 1473 K (1.4×10^{-17} m^2/s). Based on the results, dense products can be sintered using these $BaTiO_3$ powders at relatively low energy compared with hydrothermal $BaTiO_3$ powder.

3.3 In-situ observation of formation process of $Ba_5Nb_4O_{15}$ nano-grain from Ba–Nb ethoxide and the grain growth mechanism

The fabrication of advanced electronic components requires high-quality powders, and these must provide homogeneous quality, fine grains, and uniform grain sizes. Suyama et al. reported a new preparation route for the compounds $BaTiO_3$[24)] and $Ba_5Nb_4O_{15}$,[25)] in which these compounds could be successfully synthesized from double-metal alkoxides. This method could achieve synthesis at low temperature and obtain fine particles. To improve the morphology and microstructure, the crystallization process should be controlled under experimental conditions.[26)–28)] However, the crystallization behavior is not well understood.

In order to understand the crystallization process, a Ba5–Nb4 ethoxide was annealed in the range of 373–1273 K and observed with a high-resolution TEM.[29)] Below 673 K, the Ba5–Nb4 ethoxide was decomposed to the amorphous phase by heating, and organic gases were generated with the subsequent loss in weight. At 773 K, small crystals appeared in the amorphous matrix. With increasing temperature, the crystals' sizes became larger and their masses denser by the merging of small crystals. At 1173 K, the crystals of 70–150 nm in size were obtained at 1173 K.

Furthermore, in-situ observation of the crystal growth was made using a thermal holder in a TEM from ambient temperature through 1173 K. Structural changes in the $Ba_5Nb_4O_{15}$ crystal by heating were successfully recorded. The product in the TEM was, however, an oxygen-deficient compound of $Ba_5Nb_4O_{15-x}$ under a vacuum condition. **Figure 3** shows the changes in the microstructure of the specimen by heating on the thermal stage. The starting material used was a specimen annealed at 873 K in air for 1.5 h, which has small crystalline formations in the amorphous matrix. At 1133 K, dark contrast regions as a crystal phase increased in the amorphous matrix [Fig. 3(c)]. The temperature was kept at 1133 K for about 85 min. During observation at that temperature, the polycrystal containing an amorphous phase became dense crystals [Fig. 3(e)]. At 1173 K, the bulk consisted of five crystals as shown in Fig. 3(f).

Figure 4 shows the structural changes in the area enclosed by the rectangle in Fig. 3(c) at 1133 K for 50 min, in which the shrinkage and disappearance of small grains in a large grain matrix were observed. The crystalline region extended into the hole of the matrix for 20 min in Figs. 4(a)–4(c). In the next step, the boundaries moved by merging the small grains. In Fig. 4(d), crystal 1 moved toward the large crystal. After that, the boundary between crystals 1 and 2 moved quickly, and the small crystal 2 moved toward crystal 1. Eventually, crystals 1 and 2 disappeared. From the video of the processes in Figs. 4(d)–4(i), we observed that very small grains of $Ba_5Nb_4O_{15}$ on a nearly flat matrix shrank and vanished. This phenomenon has been analyzed by sintering two spherical grains with different sizes and by sintering a heterogeneous powder compact. The ratios of grain size and grain boundary diffusion to surface diffusion are the most important parameters controlling the sinterability of ceramics.[30)] We analyzed the shape change during shrinkage using a new material transport theory, in which we postulated that the rate of material transport is proportional to excess free energy in the system, and the diffusion coefficient and effective diffusion area are divided by the effective diffusion length. Calculations indicated that grain boundaries were high and that a single diffusion process did not fully simulate a shape change. It was assumed that grain boundary impedes grain shrinkage. By combining the two independent processes of grain shrinkage by grain boundary diffusion vertical to the boundary and reverse sintering by volume or surface diffusion, we succeeded in simulating the grain-shape change. We concluded that grain shrinkage maintaining a hemispherical truncated shape occurred only in the cases of high grain boundary energy and high impedance of grain boundary diffusion.[30)]

3.4 In-situ observation of phase transition of layered perovskite $BaLn_2Mn_2O_7$ (Ln = Gd, Pr, Eu)

The rare-earth manganite $BaLn_2Mn_2O_7$ (Ln = rare-earth element) has an $Sr_3Ti_2O_7$-type layered perovskite structure with double-block oxygen octahedra belonging to the Ruddlesden–

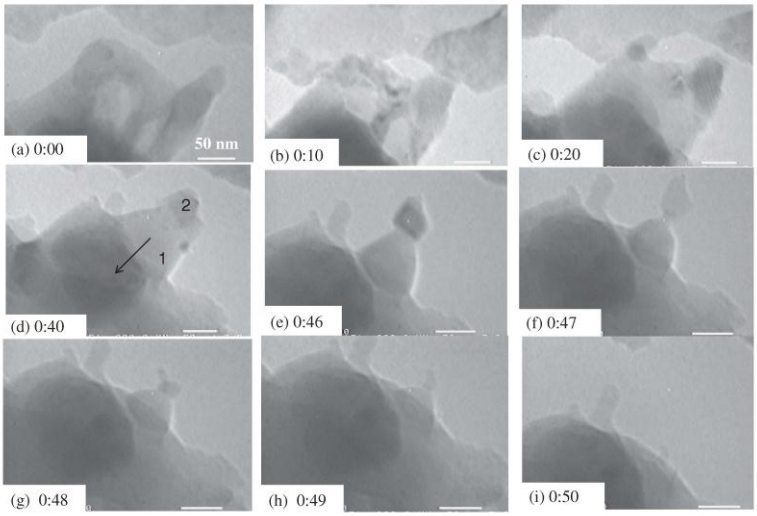

Fig. 4. Enlarged TEM images enclosed by the rectangle in Fig. 3(c) observed for 50 min at 1133 K.[27]

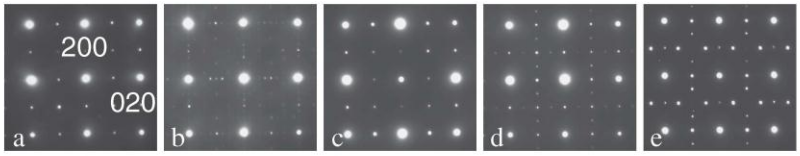

Fig. 5. SAED patterns of $BaGd_2Mn_2O_7$ along the [001] zone axis taken in-situ at various temperatures: at (a) R.T for phase I, (b) 373 K for intermediate phase, (c) 420 K for phase II, (d) 623 K for phase II + phase III, and (e) 723 K for phase III.[43]

Popper-type homologous series $AO(ABO_3)_2$.[31] Deschizeaux-Cheruy and Joubert were the first to synthesize these manganites (Ln = Nd–Gd) in an N_2 atmosphere.[32] After that, many phases were reported for the oxides, depending on the synthesis or annealing conditions.[33)–40)] High-temperature X-ray diffraction (XRD) analysis as well as electrical conductivity and thermal analyses revealed phase transitions for the Sm, Eu, Gd, Nd and Tb compounds, which change from orthorhombic to tetragonal by heating. Kamegashira has suggested that the tetragonal $I4/mmm$ structure is stable at high temperatures.[41] In the Gd-manganite, the tetragonal phase is, however, reported to transform into another orthorhombic form at 773 K on heating.[42] This is contradictory to the conventional understanding of the successive phase transition series common in perovskite-related families whose symmetries are expected to change from lower to higher with increasing temperatures and vice versa.

In-situ observation of the phase transition was made and we successfully observed the first-order phase transition for $BaGd_2Mn_2O_7$ using a high-temperature TEM. The orthorhombic phase of $BaGd_2Mn_2O_7$ was stable from room temperature up to approximately 450 K. The space group of phase I was assumed to be $Pnnm$ by an electron diffraction method, and the atomic parameters of the structure were refined by an X-ray four-circle diffractometer, as described in our earlier paper.[43] **Figure 5** shows the SAED patterns along the [001] zone axis at various temperatures. At around 333 K, the orthorhombic phase I started to transform into an intermediate phase with a rather complex diffraction pattern as shown in Fig. 5(b). Then, the intermediate phase transformed into the tetragonal phase II at approximately 420 K. The space group of phase II was assumed to be $P4_2/mnm$, and phase II was stable between 420 and 623 K. These results agree with the high-temperature XRD and electrical conductivity results from our experiments. With increasing temperature, a new phase III nucleated in the phase II matrix at 623 K. The SAED pattern at 623 K can be interpreted as a mixture of phases II and III, and the coexistence of phases II and III at 623 K was also confirmed by the dark-field images.[43] The coherency between phases II and III was good in the [001] zone. Phase III is sheath-shaped with dimensions of several tens of nanometers in width and much longer in length. Above 723 K, phase II finally disappeared, and then the crystal was composed of phase III.

A small misfit in the cell dimension along the c-axis was observed between phases II and III in **Fig. 6**. No such significant misfit was observed from room temperature up to approximately 600 K. This means that the transition between phases I ($Pnnm$) and II ($P4_2/mnm$) is hardly detectable in the [100] zone. Above 600 K, however, a composite diffraction pattern started to appear, as shown in Fig. 6(b). The pattern can be decomposed into two

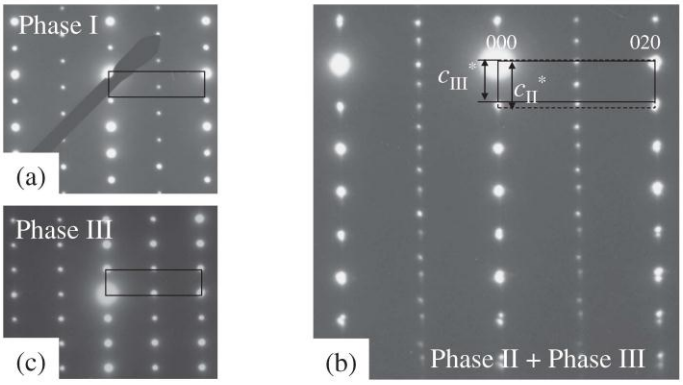

Fig. 6. Changes in SAED patterns taken from the [100] zone for $BaGd_2Mn_2O_7$ axis by heating. (a) At room temperature, (b) at 673 K, and (c) at 1023 K.[43)]

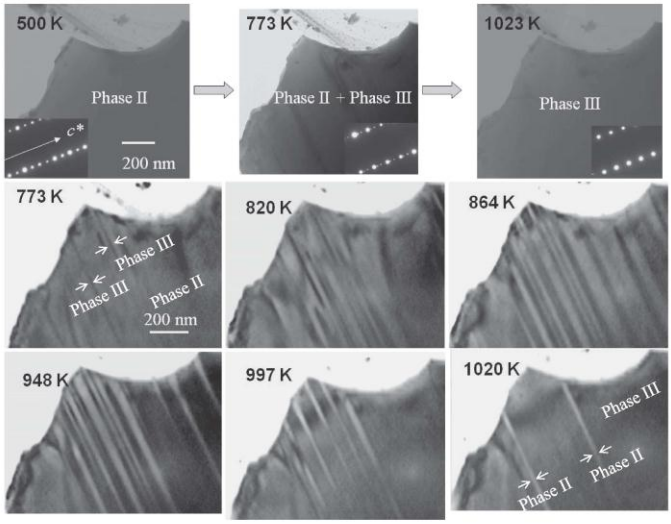

Fig. 7. In-situ observation of phase III growing in the phase II matrix of $BaGd_2Mn_2O_7$.

planar lattices: a face-centered rectangular lattice and a primitive rectangular lattice with half the repetition length along *b*. The former suggests the presence of phase II, and the latter corresponds to phase III. The split reflections at 673 K indicate that the *c* length of phase III is about 1.5% longer than that of phase II. The *c* length of phase III remained almost constant with increasing temperature. Phase II disappeared above 800 K. No significant change was observed in the specimen on further heating up to 1023 K, the highest temperature available for this in-situ TEM observation.

How did phase III extend into the phase II matrix? We could observe in-situ the first-order phase transition using a video camera as shown in **Fig. 7**. At 500 K, the TEM image shows a single-phase grain constructed by phase II. At 773 K, phase III appeared with a dark contrast parallel to the (00*l*) plane as a layer, and weak reflections were observed in the SAED pattern. The difference in the contrast depends on their crystal structures as shown in Fig. 6. Phase III grew until covering the entire inspected region at around 1023 K. The I–II transition at around 420 K may accompany tilts of the MnO_6 octahedra because the symmetries suggest a change in the octahedral tilt system from (Φ00) (0Φ0) for $P4_2/mnm$ to ($\Phi_1\Phi_2$0)($\Phi_2\Phi_1$0) for *Pnnm*.[43)] On the other hand, the nucleation-growth process observed in the II–III transition suggests that this is a first-order transition. Actually, the repeated in-situ experiments revealed that the transformation speed is temperature-dependent. The II–III transition point could be related to the inflection of the electrical conductivity curve against temperature at approximately 620 K in

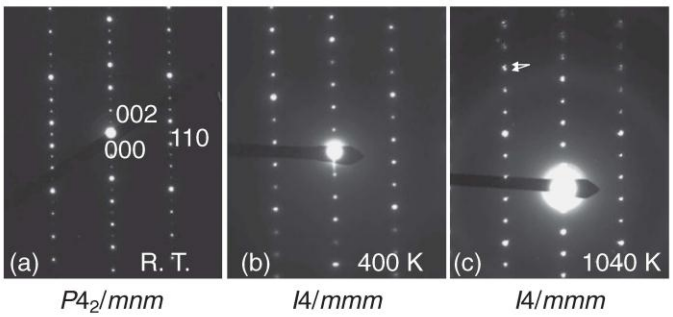

Fig. 8. Changes in SAED patterns of $BaPr_2Mn_2O_7$.[45]

our experiment. From the SAED patterns, phase III seems to have a close relation with the monoclinic $B112/m$ structure that was observed in $BaTb_2Mn_2O_7$ upon annealing.[39] It is expected that one or more phase transitions occur at temperatures above 1023 K because the symmetry of phase III is still much lower than the $F4/mmm$ assumed for the prototype.

A similar first-order phase transition was observed even in $BaPr_2Mn_2O_7$. As shown in **Fig. 8**, two types of transitions were observed: a transition from primitive tetragonal ($P4_2/mnm$) to body-centered tetragonal ($I4/mmm$) at around 400 K and a first-order phase transition at around 1040 K. The former transition may be controlled by the tilting of octahedra MnO_6.[44] Above 1040 K, the reflections began to split into two along the c-direction [Fig. 8(c)], as indicated by arrows. The split was caused by the presence of two phases: a low-temperature phase and a high-temperature phase. The high-temperature phase had about 1.5% lattice mismatch along the c-axis compared with the low-temperature phase. After only about 10 min, the reflections from the low-temperature phase vanished. Three lengths, Mn–O1, Mn–O2, and Mn–O3, in $BaPr_2Mn_2O_7$ were measured by a high-temperature XRD, as described in our previous paper.[45] The Mn–O3 length indicates an anisotropic nature along the c-axis by the Jahn–Teller effect of the Mn^{3+} ion. Crystallographic data show that the Mn–O2 distance is obviously elongated by about 1% at 1173 K, and it is connected with two perovskite layers like Mn–O2–Mn. The changes in the cell dimensions indicate that the transition is irreversible by comparison of measurements on cooling and heating in XRD.[45] In general, phase transition is accompanied by tilting of the MnO_6 octahedra in the perovskite, and the symmetries change in the octahedral tilt system. In this case, however, the first-order phase transition occurred even in $BaPr_2Mn_2O_7$ ($I4/mmm$), which had no tilting of the octahedra.

The first-order phase transition should occur uniquely in the layered structure with double-block oxygen octahedra related to the Jahn–Teller effect of the Mn^{3+} ion. Recently, we also observed the multiple phase transition in-situ in $BaEu_2Mn_2O_7$.[46] In the future, we are going to clarify more systematically such issues as in-situ phase transition from liquid-N_2 temperature to high temperature in order to understand the nature of manganite with the layered perovskite structure.

4. Conclusions

The use of high-temperature TEM has been successful in revealing previously unreported phenomena in relation to oxides, grain growth, and structural phase transitions. In-situ observations using high-temperature TEM require advanced observational skills, and even though failures may be many, a successful observation can open the door to new and valuable findings. On the basis of $BaTiO_3$ observations, we have clarified the vanishing mechanism of internal pores and the mechanism of $BaCO_3$ phase generation/vanishing at high temperatures, and by observing the grain growth process, we have calculated the grain-boundary diffusion coefficient at high temperatures and obtained new findings on the thermal behavior of nanoparticles. Moreover, by making long-term observations of the crystallization process and grain growth of $Ba_5Nb_4O_{15}$, we have clarified the mechanism behind the formation of nanocrystalline particles from Ba–Nb ethoxide, and by observing the growth process of $Ba_5Nb_4O_{15}$ nanoparticles, we have proposed a theory of grain growth. We have also succeeded in making an in-situ observation of a first-order phase transition in manganite having a layered perovskite structure, which has not been previously reported on. The phenomenon of a high-temperature phase appearing in the base material (low-temperature phase) and spreading throughout the entire sample yields valuable data and highly original findings that can only be obtained by high-temperature TEM. This phase transition only took about 10 min to observe, which demonstrates the appeal of TEM in-situ observations. However, compared to today's computer-based research style in which data can also be obtained in a relatively short period of time, TEM in-situ observations require highly skillful professionals who are not afraid of a challenge and are prepared to experiment repeatedly with an eye toward success. Looking to the future, I expect studies of fine structures by TEM in-situ observations to make a great contribution to clarifying unexplained mechanisms in ceramic materials.

Acknowledgements I would like to express my deep appreciation to Prof. K. Urabe and Prof. H. Ikawa, both in heaven now, for many useful suggestions on this work. The author would like to thank Prof. N. Kamegashira of Toyohashi University of Technology, Dr. H. Tanaka of NIMS, Prof. N. Ishizawa of Nagoya Institute of Technology, Prof. Y. Suyama of Shimane University, Prof. M. Yashima of Tokyo Institute of Technology, and Prof. K. Kizima of Kyoto Institute of Technology for useful discussions on this paper. Thanks are also extended to Dr. K. Watari and Dr. Y. Kinemuchi of AIST, Prof. Y. Makino of Osaka University, Prof. Y. Aoi of Ryukoku University, Dr. H. Satoh of Toyohashi University of Technology, Prof. J. Tatami of Yokohama National University, Prof. K. Fukuda of Nagoya Institute of Technology, and Prof. M. Mabuchi of Kyoto University for their useful comments in related works.

References

1) Y. Ikuhara, *JEOL News*, 40, 8–23 (2005).
2) H. Kaga, Y. Kinemuchi, H. Yilmaz, K. Watari, H. Nakano, H. Nakano, S. Tanaka, A. Makiya, Z. Kato and K. Uematsu, *Acta Mater.*, 55, 4753–4757 (2007).
3) K. Sato, H. Horibe, S. Takashi, H. Yuji, H. Nakano, H. Nagai, K. Mitsuishi and K. Watari, *J. Mater. Chem.*, 20, 2749–2752 (2010).
4) Y. Sato, T. Yamamoto and Y. Ikuhara, *J. Am. Ceram. Soc.*, 90, 337–357 (2007).
5) H. Nakano, M. Yamada, M. Fukumoto and E. Yamaguchi, *J. Therm. Spray Technol.*, in press.
6) D. Hennings, C. Metzmacher and B. S. Schreinmacher, *J. Am. Ceram. Soc.*, 84, 179–182 (2001).
7) D. Hennings and S. Schreinemacher, *J. Eur. Ceram. Soc.*, 9, 41–46 (1992).
8) Z. Xinhua, Z. Jianmin, Z. Shunhua, L. Zhiguo and M. Naiben, *Cryst. Growth*, 310, 434–441 (2008).
9) P. J. Hoon and P. S. Do, *J. Chem. Eng. Jpn.*, 41, 631–638 (2008).
10) K. Fukai, K. Hidaka, M. Aoki and K. Abe, *Ceram. Int.*, 16, 285–290 (1990).
11) Y. Sakabe, N. Wada, J. Ikeda and Y. Hamaji, Proc. ISAF 11th IEEE, Ed. by E. Colla (1998) pp. 565–569.
12) H. Nakano, K. Urabe, T. Oikawa and H. Ikawa, *J. Am. Ceram. Soc.*, 87, 1594–1597 (2004).
13) H. Ikawa, N. Munekata, T. Ozeki, M. Takemoto and T. Shirakami, *Trans. Mater. Res. Soc. Jpn.*, 27, 707–710 (2002).
14) H. Nakano, K. Urabe and H. Ikawa, *J. Am. Ceram. Soc.*, 86, 741–743 (2003).
15) M. Kumota, K. Kyaw, F. Watanabe, H. Matsuda and M. Hasatani, *J. Chem. Eng. Jpn.*, 34, 326–332 (2001).
16) H. Ikawa, *Ceramics*, 27, 701–706 (1992) [in Japanese].
17) T. Wada and T. Tsurumi, *Ceramics*, 41, 300–305 (2006) [in Japanese].
18) K. W. Seo and J. K. Oh, *J. Ceram. Soc. Japan*, 108, 691–696 (2000).
19) K. Suzuki and K. Kizima, *J. Ceram. Soc. Japan*, 12, S916–S923 (2004).
20) H. Nakano, K. Suzuki and K. Kizima, *J. Am. Ceram. Soc.*, 89, 1461–1464 (2006).
21) W. D. Kingery, "Introduction to Ceramics," 2nd ed., John Wiley & Sons, Inc., New York (1976) pp. 448–515.
22) M. Kusunoki, K. Yonemitsu, Y. Sasaki, Y. Ikuhara and Y. Kubo, *Ceram. Trans.*, 44, 455–464 (1994).
23) M. Kusunoki, K. Yonemitsu, Y. Sasaki and Y. Kubo, *J. Am. Ceram. Soc.*, 76, 763–765 (1993).
24) Y. Suyama, T. Noritake and M. Nagasawa, *Jpn. J. Appl. Phys.*, 36, 5939 (1997).
25) T. Yano and Y. Suyama, *Proc. 19th Korea-Japan International Seminar on Ceramics*, **19**, 627–630 (2002).
26) Y.-J. Hsiao, Y.-H. Chang, Y.-S. Chang and T.-H. Fang, *J. Am. Ceram. Soc.*, 90, 2287–2290 (2007).
27) H. Nakano, Y. Hirano and Y. Suyama, *J. Soc. Mater. Sci. Jpn.*, 56, 500–504 (2007).
28) H. Nakano and Y. Suyama, *Adv. Sci. Technol.*, 63, 47–51 (2010).
29) H. Nakano, T. Yano and Y. Suayam, *J. Ceram. Soc. Japan*, 113, 59–63 (2005).
30) H. Tanaka, H. Nakano and Y. Suyama, *Acta Mater.*, 55, 2423–2432 (2007).
31) N. Ishizawa, *Ceramics*, 31, 409–413 (1996) [in Japanese].
32) M. N. Deshizeaux Cheruy and J. C. Joubert, *J. Solid State Chem.*, 40, 14–19 (1981).
33) N. Kamegashira, H. Nakano, G. Chan and J. Meng, *J. Rare Earths*, 22, 582–585 (2004).
34) J. Meng, H. Satoh and N. Kamegashira, *J. Alloys Compd.*, 244, 75–78 (1996).
35) N. Kamegashira, J. Meng, T. Murase, K. Fujita, H. Satoh, T. Shishido and T. Fukuda, 10th International Ceramics Congress, Part A, Ed. by P. Vincenzini, Florence (2002) pp. 181–186.
36) N. Kamgegashira, J. Meng, T. Mori, A. Murase, H. Satoh, T. Shishido and T. Fukuda, *Mater. Lett.*, 57, 1941–1944 (2003).
37) S. Ueno and N. Kamegashira, *Powder Diffr.*, 12, 103–105 (1997).
38) N. Kamegashira, A. Shimono and M. Hirokawa, *Mater. Chem. Phys.*, 24, 389–397 (1990).
39) N. Kamegasira, J. Meng, K. Fujita, H. Satoh, T. Shishido and K. Nakajima, *J. Alloys Compd.*, 408–412, 603–607 (2006).
40) N. Kamegashira, H. Satoh, J. Meng and T. Mikami, *J. Alloys Compd.*, 374, 173–176 (2004).
41) N. Kamegashira, *Shokubai*, 31, 222–226 (1989).
42) J. Meng, P. R. China, N. Kamegashira, A. Murase, H. Satoh, H. Y. Wang, Q. B. Bo and C. Peng, Proc. International J. Materials and Product Technology, Special Issue, SPM 1, Ed. by M. A. Dorgham (2001) pp. 397–401.
43) H. Nakano, N. Ishizawa, N. Kamegashira and M. Yashima, *J. Am. Ceram. Soc.*, 90, 1342–1345 (2007).
44) K. S. Aleksandrov and J. Bartolome, *J. Phys.: Condens. Matter*, 6, 8219–8235 (1994).
45) H. Nakano, N. Ishizawa, H. Satoh and N. Kamegashira, *Adv. Sci. Technol.*, 67, 113–117 (2010).
46) H. Nakano, N. Ishizawa and N. Kamegashira, *J. Eur. Ceram. Soc.*, 30, 233–236 (2010).

Dr. Hiromi Nakano received B.S., M.S., and Dr. (Eng.) from Toyohashi University of Technology, Japan in 1981, 1983 and 2000, respectively. She joined Murata Manufacturing Co., Ltd. in 1983. She transferred to Ryukoku University in 1989. She is as an associate professor at Cooperative Research Facility Center, Toyohashi University of Technology from 2009. Her current interest is characterization of ceramics using a transmission electron microscope to control of the material properties and the design of new materials.

Available online at www.sciencedirect.com
ScienceDirect
Journal of the European Ceramic Society 30 (2010) 233–236
www.elsevier.com/locate/jeurceramsoc

In-situ observation of phase transformations in layered perovskite $BaEu_2Mn_2O_7$

Hiromi Nakano [a,*], Nobuo Ishizawa [b], Naoki Kamegashira [c]

[a] *Electron Microscope Laboratory, Ryukoku University, Seta, Otsu, 520-2194, Japan*
[b] *Ceramics Research Laboratory, Nagoya Institute of Technology, Asahigaoka 10-6-29, Tajimi, 507-0071, Japan*
[c] *Department of Materials Science, Toyohasi University of Technology, Tempaku-cho, Toyohashi, 441-8580, Japan*

Available online 2 June 2009

Abstract

The layered perovskite $BaLn_2Mn_2O_7$ (Ln = rare earth) has a $Sr_3Ti_2O_7$-type structure with double-block oxygen octahedra belonging to the Ruddlesden–Popper-type homologous series $AO(ABO_3)_2$. The $BaEu_2Mn_2O_7$ shows multiple phase transformations upon heating by high-temperature TEM, from tetragonal phase I ($P4_2/mnm$) to monoclinic phase III via phase II ($I4/mmm$). Weak reflections from phase III started to appear on the selected area diffraction pattern along the c-direction above 277 °C and became stronger gradually with increasing temperature. Finally, all of the reflections were from only phase III above 750 °C. This shows a first-order phase transformation, and the coexistence of low- and high-temperature phases was also observed clearly in a quenched specimen. The differences in those structures are the periodicity along the *c*-axis and the high-temperature phase's 1.5% longer *c* length than that of the low-temperature phase.

Keywords: Electron microscopy; Microstructure; Perovskites; Phase transformation; Manganite

1. Introduction

The rare-earth manganite $BaLn_2Mn_2O_7$ (Ln = rare-earth element) has a $Sr_3Ti_2O_7$-type layered perovskite structure with double-block oxygen octahedra belonging to the Ruddlesden–Popper-type homologous series $AO(ABO_3)_2$.[1] Deshizeaux Cheruy and Joubert were the first to synthesize those manganites (Ln = Nd–Gd) in an N_2 atmosphere.[2] Subsequently, many phases were reported for the oxides, depending on the synthesis or annealing conditions.[3–9] Those annealing conditions were based on the phase transformation of the $BaLn_2Mn_2O_7$. The phase transformations of the oxides have been investigated by high-temperature X-ray diffraction (XRD), electrical conductivity, and thermal analyses.[3,10,11] The transformation temperatures tend to increase with decreasing ionic radii of the Ln cations.[10] These results showed that the transformation occurring is the successive phase transition series common in perovskite-related families, whose symmetries are expected to change from lower to higher with increasing temperature. As a result, it was reported that the tetragonal $I4/mmm$ structure of $BaLn_2Mn_2O_7$ is stable at high temperatures.[12]

Recently, however, we have found first-order phase transformations in the $BaGd_2Mn_2O_7$ and $BaPr_2Mn_2O_7$ by using a high-temperature transmission electron microscope (TEM).[13,14] These findings are contradictory to the conventional understanding of the successive phase transformation. We believe that the first-order phase transformation may uniquely occur in layered perovskite with double-block oxygen octahedra. In the case of $BaPr_2Mn_2O_7$, it occurred for only 10 min without change in the crystal symmetry.[14] On the other hand, the first-order phase transformation in $BaGd_2Mn_2O_7$ was observed slowly with increasing temperature. It was found that the time of phase transformation was related to the ionic radius of rare earth and its structural distortion. It is expected that similar phase transformations should occur in other rare-earth manganites. In order to observe such *in-situ* structural change, high-temperature TEM is the most suitable technique, even though it requires a high-level technique for observation.

In the present study, we report phase transformation of $BaEu_2Mn_2O_7$ observed mainly by a high-temperature TEM. Furthermore, the high-temperature phase appearing in the phase

* Corresponding author. Tel.: +81 77 543 7774; fax: +81 77 543 7758.
E-mail address: hiromi@rins.ryukoku.ac.jp (H. Nakano).

0955-2219/$ – see front matter © 2009 Elsevier Ltd. All rights reserved.
doi:10.1016/j.jeurceramsoc.2009.05.011

transformation was analyzed using a quenched specimen, which was heated to 700 °C and then cooled down.

2. Experimental procedure

The starting powders of $BaCO_3$, Eu_2O_3, and Mn_2O_3 were mixed together and calcined at 1350 °C in Ar atmosphere for 2 days. The product was confirmed as a single phase of $BaEu_2Mn_2O_7$ by the powder XRD analysis. The product was then pulverized and hydrostatically pressed into a rod. Single crystals were grown by the floating zone (FZ) method in Ar atmosphere. The procedure of crystal growth is detailed in the previous paper.[5] The crystals were examined by the four-circle single-crystal diffractometer Rigaku-AFC7R. The quenched specimen was annealed at 700 °C and then cooled down.

A fragment of the crystal was crushed and scooped onto a copper mesh with carbon-coated microgrids. The *in-situ* TEM observation was performed on a thermal stage in the temperature range from 20 to 800 °C (JEM-2000EX, EM-SHU2 specimen holder, JEOL). The temperature was controlled manually. The heating rate was approximately 600 °C/h. High

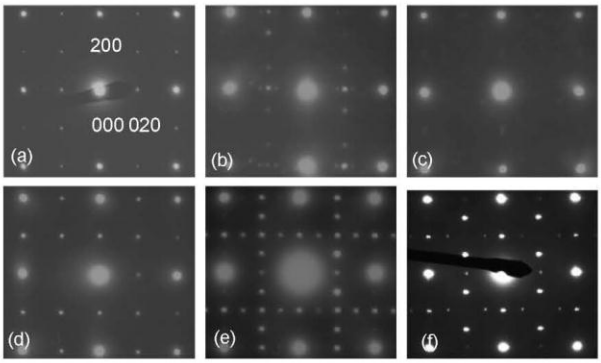

Fig. 1. SAED patterns of $BaEu_2Mn_2O_7$ along the [0 0 1] zone axis taken at various temperatures: (a) RT for phase I, (b) 100 °C, (c) 160 °C for phase II, (d) 227 °C, (e) 277 °C, and (f) 500 °C for phase III.

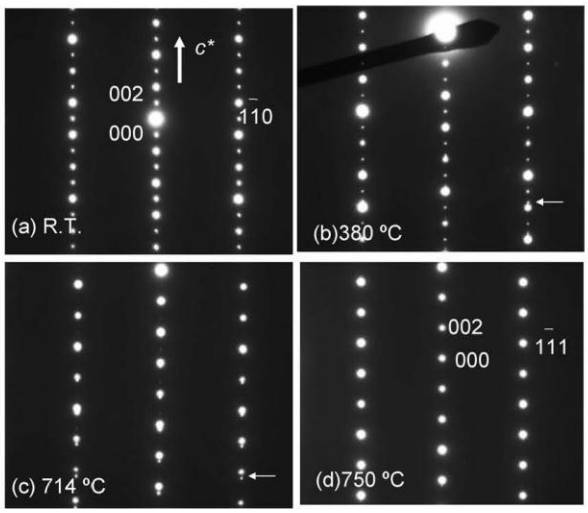

Fig. 2. Changes in SAED patterns taken from [1 1 0] zone axis. (a) RT, (b) at 380 °C, (c) at 714 °C, and (d) at 750 °C.

resolution image observation was using a TEM (JEM 3000F, JEOL).

3. Results and discussion

The as-grown crystal of $BaEu_2Mn_2O_7$ showed the tetragonal $P4_2/mnm$ symmetry by four-circle single-crystal diffractometer.[5] Fig. 1 uses high-temperature TEM to show the SAED patterns along the [0 0 1] zone axis at various temperatures. At around 100 °C, the tetragonal phase I ($P4_2/mnm$) started to transform into an intermediate phase with a rather complex diffraction pattern as shown in Fig. 1(b). Then, the intermediate phase transformed into the tetragonal phase II at approximately 160 °C in (c). The space group of phase II was assumed to be $I4/mmm$. However, the transformation temperature was lower than that of phase transition (277 °C) measured by DSC.[11] With increasing temperature, we found the phase transformation in the next step. The $I4/mmm$ phase was stable in a narrow temperature region. Pattern (c) changed into pattern (d), which was assumed to be $P4_2/mnm$. Then, a new phase III started to nucleate in the low-temperature phase matrix at 277 °C, and the temperature agreed with the DSC and electrical conductivity results.[10,11] The complex pattern (e) can be interpreted as a mixture of the low-temperature phase (d) and the high-temperature phase (f). At around 500 °C, the intensity of 1 1 0 reflection became very weak, which indicated that the low-temperature phase nearly disappeared in (f).

Structural change was *in-situ* observed clearly along the [1 1 0] zone axis, as shown in Fig. 2. Above 277 °C, weak reflections started to appear, as indicated by the arrow in (b), and the intensities grew stronger at 714 °C. The split reflections indicate that the c length of phase III is 1.5% longer than that of the low-temperature phase, as with $BaGd_2Mn_2O_7$.[13] With increasing temperature, the intensities of the reflections at $1\,\bar{1}\,0$ became weaker. Finally, the low-temperature phase disappeared above 750 °C. The repeated *in-situ* experiments revealed that the transformation speed is temperature-dependent. The results show that the transformation from the low-temperature phase into phase III was of first order due to the coexistence of low- and high-temperature phases.

A structure of coexisting phases was also observed using a quenched specimen, which was heated to 700 °C and quenched, as shown in Fig. 3. The lamellar structure was observed along the c-axis, which was composed of the low-temperature phase and the high-temperature phase with a lattice mismatch of 1.5%. The SAED pattern corresponded to Fig. 3. In the enlarged TEM image enclosed by the rectangle in (a), we can clearly observe the low-temperature phase region and the high-temperature phase region due to the difference in periodicity along the c-axis. These results show that phase III was nucleated in the low-temperature phase matrix.

Fig. 4 shows a TEM image and SAED pattern of the quenched specimen along the [0 2 1] zone axis. The lamellar structure formed by twinning at about 40-nm sizes was observed in (a). This structure of the phase is not a tetragonal because the angle formed by the planes of (2 0 0) and $(0\,\bar{2}\,4)$ is not 90°. Extra reflections were detected as 1/2, 1/2, $\bar{1}$. This result agrees with

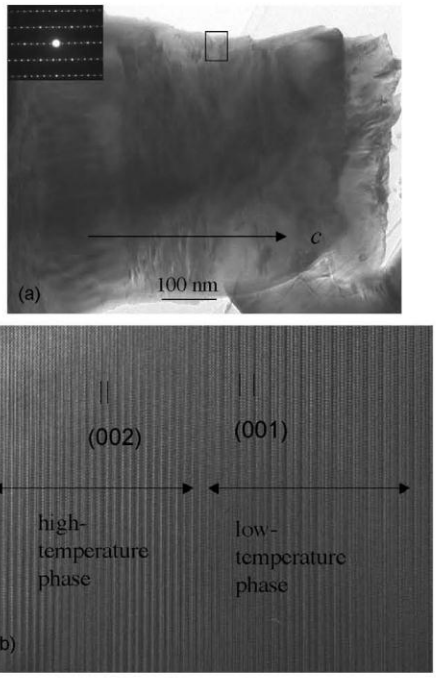

Fig. 3. TEM images of quenched specimen of $BaEu_2Mn_2O_7$ taken from the [1 1 0] zone axis. (a) Low-magnification image and (b) enlarged image from area enclosed by the rectangle in (a).

the SAED pattern shown in Fig. 1(f). Phase III seems to have a close relation with the monoclinic $B112/m$ structure, which was observed in annealed $BaTb_2Mn_2O_7$.[9] The complex diffraction pattern was caused by the twinning structure of the monoclinic cell.

The I–II transformation may accompany tilts of the MnO_6 octahedra because the symmetries suggest a change in the octahedral tilt system from (0 0 0)(0 0 0) for $I4/mmm$ to (Φ 0 0) (0 Φ 0) for $P4_2/mnm$.[15] A previous paper, by using high-temperature XRD, reported that the tetragonal $I4/mmm$ structure is stable at high temperatures.[12] In our experiment, we confirmed that the $I4/mmm$ phase is stable in a narrow temperature range during the phase transformation. In the case of $BaGd_2Mn_2O_7$, however, the $I4/mmm$ phase did not appear during the phase transformation. This seems to be related to the structural distortion and ionic radius of rare earth. On the other hand, later transformation of phase III suggested that the transformation is of the first order. We believe that the first-order phase transformation may uniquely occur in layered perovskite with double-block oxygen octahedra.[10,14] The multiple transformations are related to the distortion of the structure. In the repeated trial, the transformation occurred slowly via the $I4/mmm$ phase as a meta-stable phase. It is expected that Tb–manganite will require a longer

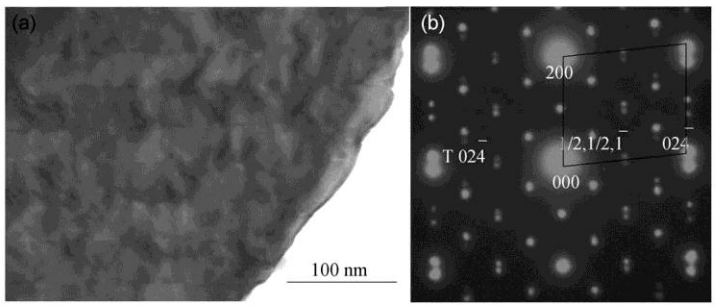

Fig. 4. Lamellar structure by twinning in quenched specimen of $BaEu_2Mn_2O_7$. (a) TEM image, and (b) SAED pattern taken from the [0 2 1] zone axis.

time for phase transformation because, like Gd–manganite, it has a small ionic radius. On the other hand, it is also assumed that the transformation for Nd–manganite, via the *I4/mmm* phase as a stable phase, will take a shorter time because, like Pr–manganite, it has a large ionic radius. Although we can make these assumptions based on the known experimental data for Pr–manganite and Gd–manganite, an *in-situ* experiment using high-temperature TEM should be conducted to more systematically clarify such issues as phase transformation. In the future, we are going to use high-temperature TEM to more systematically clarify such issues as *in-situ* phase transformation in order to understand the nature of layered perovskite structure.

4. Conclusion

Phase transformation in $BaEu_2Mn_2O_7$ has been studied by *in-situ* high-temperature TEM observation. The tetragonal phase I ($P4_2/mnm$) transformed into the tetragonal phase II (*I4/mmmm*) at a temperature roughly above 160 °C. The *I4/mmm* phase is stable at narrow temperature region. Then, phase III nucleated in the matrix at 277 °C and grew to cover the entire region under inspection at 500 °C. Phase III has an approximately 1.5% larger cell size along the *c*-axis compared with phase II. Phase III seems to have a close relation with the monoclinic structure. The transformation into phase III was considered a first-order transformation due to the coexistence of low-temperature and high-temperature phases. A structure of coexisting phases was observed in a quenched specimen, which was heated to 700 °C and then cooled down. The first-order phase transformation should occur uniquely in the layered structure with double-block oxygen octahedra.

Acknowledgement

This work was partially sported by Grant-in-Aid for Scientific Research No. 18560660 (H.N.) from the Japan Society for the Promotion of Science.

References

1. Ishizawa, N., layered perovskite-structure classification. *Ceramics*, 1996, **31**(5), 409–413 [in Japanese].
2. Deshizeaux Cheruy, M. N. and Joubert, J. C., Donnees cristallographiqes sur une nouvelle serie de manganites mixtes de terre rare et d'alcalino-terreux. *J. Solid State Chem.*, 1981, **40**, 14–19.
3. Kamegashira, N., Nakano, H., Chan, G. and Meng, J., Phase behavior of rare earth manganites. *J. Rare Earth*, 2004, **22**(5), 582–585.
4. Meng, J., Satoh, H. and Kamegashira, N., Crystal structure refinement of tetragonal $BaTb_2Mn_2O_7$. *J. Alloys Compd.*, 1996, **244**, 75–78.
5. Kamegashira, N., Meng, J., Murase, T., Fujita, K., Satoh, H., Shishido, T. *et al.*, Crystal growth and structure analysis of rare earth manganites with layered perovskite type. In *10th International Ceramics Congress PartA, Edi. P. Vincenzini, Florence*, 2002, pp. 181–186.
6. Kamegashira, N., Meng, J., Mori, T., Murase, A., Satoh, H., Shishido, T. *et al.*, Growth and structure analysis of single crystal of tetragonal $BaGd_2Mn_2O_7$ with a superlattice structure. *Mater. Lett.*, 2003, **57**, 1941–1944.
7. Ueno, S., Kamegasira, N., Nakano, H. and Enami, K., Crystal structure of layered perovskite, barium europium manganese oxide [$BaEu_2Mn_2O_7$]. *Mater. Res. Bull.*, 1996, **31**, 497–502.
8. Ueno, S. and Kamegashira, N., Crystal and X-ray diffraction data for orthorhombic $BaNd_2Mn_2O_7$ phase. *Powder Diffr.*, 1997, **12**(June (2)), 103–105.
9. Kamegashira, N., Satoh, H., Meng, J. and Mikami, T., Structure determination of a new phase of monoclinic $BaTb_2Mn_2O_7$. *J. Alloys Compd.*, 2004, **374**, 173–176.
10. Nakano, H., Satoh, H., Kamegashira, N. and Ishizawa, N., Phase behavior of layered manganites $BaLn_2Mn_2O_7$ (Ln = rare earth). *Phys. Status Solidi (c)*, 2006, **3**(8), 2812–2815.
11. Kamegasira, N., Meng, J., Fujita, K., Satoh, H., Shishido, T. and Nakajima, K., Study on the phase behavior on $BaEu_2Mn_2O_7$ through heat treatment of a single crystal. *J. Alloys Compd.*, 2006, **408–412**, 603–607.
12. Kamegashira, N., Phase transition and nonstoichiometry of rare earth manganites. *Shokubai*, 1989, **31**(4), 222–226 [in Japanese].
13. Nakano, H., Ishizawa, N., Kamegashira, N. and Yashima, M., In situ transmission electron microscopy observation of multiple phase transition in $BaGd_2Mn_2O_7$. *J. Am. Ceram. Soc.*, 2007, **90**(4), 1342–1345.
14. Nakano, H. and Kamegashira, N., Novel phase transition in $BaPr_2Mn_2O_7$. *J. Rare Earth*, 2006, **24**(S), 1–3.
15. Aleksandrov, K. S. and Bartolome, J., Octahedral tilting phases in perovskite-like crystals with slabs containing an even number of octahedral layers. *J. Phys.: Condens. Matter*, 1994, **6**, 8219–8235.

Advances in Science and Technology Vol. 67 (2010) pp 113-117
© (2010) Trans Tech Publications, Switzerland
doi:10.4028/www.scientific.net/AST.67.113

In-situ measurement of phase transition of layered perovskite $BaLn_2Mn_2O_7$

Hiromi Nakano[1a], Nobuo Ishizawa[2b], Hirohisa Sato[1c] Naoki Kamegashira[1d]

[1] Toyohashi University of Technology, Tempaku, Toyohashi, 441-8580, Japan

[2] Nagoya Institute of Technology, Asahigaoka, Tajimi, 507-0071, Japan

[a] hiromi @crfc.tut.ac.jp, [b]Ishizawa@nitech.ac.jp, [c]hsato@tutms.tut.ac.jp,[d]nkamegas@kktci.co.jp

Keywords: High-temperature TEM, High-temperature XRD, Phase transition, Perovskite

Abstract The $BaLn_2Mn_2O_7$ (Ln = rare earth) has a $Sr_3Ti_2O_7$-type structure with double block oxygen octahedra belonging to the Ruddlesden-Popper-Type homologous series $AO(ABO_3)_2$. *In-situ* measurement of the phase transition for $BaLn_2Mn_2O_7$ was performed using single-crystal X-ray diffraction and a high-temperature transmission electron microscope (TEM). Two types of transitions were observed in $BaPr_2Mn_2O_7$: the transition from primitive tetragonal ($P4_2/mnm$) to body-centered tetragonal ($I4/mmm$) at around 400 K and the first-order phase transition at around 1040 K. Multiple phase transitions were also observed in $BaEu_2Mn_2O_7$, with one from $P4_2/mnm$ to $I4/mmm$ at around 400 K and another, above 550 K, as a first-order phase transition. The high-temperature phase had a 1.5% lattice mismatch along the *c*-axis compared with the low-temperature phase. We succeeded in recording for the first time *in-situ* structural change in $BaGd_2Mn_2O_7$ as a movie by high-temperature TEM. The high-temperature phase nucleated parallel to the (00*l*) plane as a layer above 550 K and grew until covering the entire inspected region at around 1023 K. The first-order phase transition was caused by the structural and/or electrical distortion of the layered perovskite structure composed of Jahn-Teller ion Mn^{3+}.

Introduction

The rare-earth manganite $BaLn_2Mn_2O_7$ (Ln = rare-earth element) has a $Sr_3Ti_2O_7$-type layered perovskite structure with double-block oxygen octahedra belonging to the Ruddlesden-Popper-type homologous series $AO(ABO_3)_2$. Deschizeaux-Cheruy and Joubert were the first to synthesize those manganites (Ln = Nd- Gd) in an N_2 atmosphere [1]. Subsequently, many phases were reported for the oxides, depending on the synthesis or annealing conditions [2].

High-temperature X-ray diffraction (XRD), electrical conductivity, and thermal analyses revealed phase transitions for the Sm, Eu, Gd, Nd and Tb compounds, which undergo change from orthorhombic to tetragonal on heating. Kamegashira *et al*. suggested that the tetragonal *I*4/*mmm* structure is stable at high temperatures [2,3]. Recently, however, we have found first-order phase transitions in the Gd- and Pr- manganite by a high-temperature transmission electron microscope (TEM) [4,5]. These findings are contradictory to the conventional understanding of the successive phase transition. It is expected that similar phase transformations may occur in other rare earth manganites. So, It is important to understand the nature of the phase transition of the layered perovskite.

In the present study, we report and discuss the nature of the phase transitions of Pr- Eu- and Gd-manganites observed *in-situ* by a high-temperature TEM and high-temperature X-ray diffractometer (XRD).

Experimental procedure

The starting powders of $BaCO_3$, Eu_2O_3, and Mn_2O_3 were mixed together and calcined at 1623 K in Ar atmosphere for 2 days. The product was confirmed as a single phase of $BaEu_2Mn_2O_7$ by the powder XRD analysis. The product was then pulverized and hydrostatically pressed into a rod. Single crystals were grown by the floating zone (FZ) method in Ar atmosphere [4].

Precession imaes were taken by the CCD single-crystal diffractometer (Smart Apex II, Bruker) at various temperature in Ar gas flow.

A fragment of the crystal was crushed and scooped onto a copper mesh with carbon-coated microgrids. The *in-situ* TEM observation was performed on a thermal stage in the temperature range from 293 to 1073 K (JEM-2000EX, EM-SHU2 specimen holder, JEOL). The temperature was controlled manually. The heating rate was approximately 600 K/h. High resolution image observation was using a TEM (JEM 3000F, JEOL).

Results and discussion

Fig.1 shows selected area electron diffraction (SAED) patterns of $BaPr_2Mn_2O_7$ taken from the [110] zone axis at room temperature, 400 K, and 1040 K. Crystallographic data and selected interatomic distances are shown in Table 1. Temperature dependences of the cell dimensions in the range between 293 K and 1173 K are shown in Fig. 2.

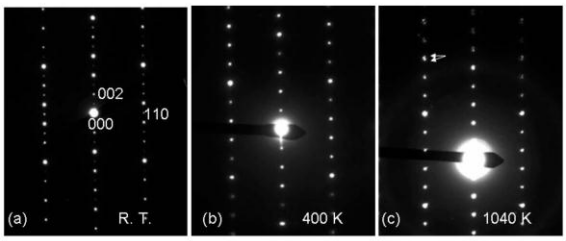

Fig. 1 SAED patterns of $BaPr_2Mn_2O_7$ taken at the [110] zone axis at room temperature in (a), 400 K in (b), and 1040 K in (c).

Table 1 Crystallographic data for $BaPr_2Mn_2O_7$

Temperature (K)	293 403 1173		
Crystal system	$P4_2/mnm$	$I4/mmm$	$I4/mmm$
a (Å)	5.5273(1) 3.	9074(3) 3.	9432(3)
c (Å)	20.6390(5) 20.	6805(2) 20.	8300(4)
volume (Å^3)	630.54(3) 315.	75(3) 323.	88(4)
Mn-O1 (Å)	1.9554	1.960	1.976
Mn-O2 (Å)	2.0476	2.051	2.068
Mn-O3 (Å)	2.218 2.	202 2.	200

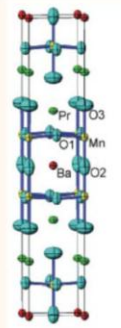

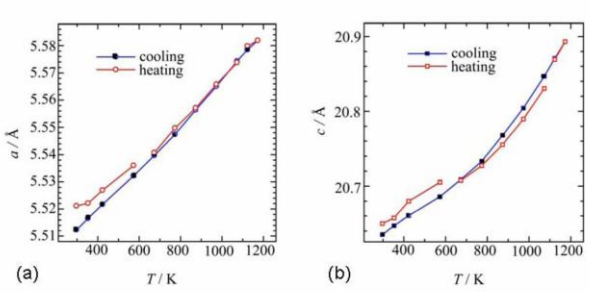

Fig. 2 Temperature dependence of the *a*-, *c*-lenhths of B a$Pr_2Mn_2O_7$. Black m arks on cooling and open marks on heating are connected.

In this time, we found two types of transitions: the transition from primitive tetragonal ($P4_2$/mnm) to body-centered tetragonal (*I*4/*mmm*) at around 400 K and the first-order phase transition at around 1040 K. The trasition from $P4_2/mnm$ to *I*4/*mmm* is controlled by the tilting of octahedra MnO_6[6]. It was occured easily even by an ir adiation of electron beam. Above 1040 K, the reflections began to split into two a long the *c*-direction (Fig, 1 c). The split was caused by the presence of two pha ses: low temperature phase and high te mperature phase. Therefore, it is the first-order phase transition. The high- temperature phas e had a 1 .5% lattice mis match along the *c*-axis com pared wi th t he low-temperature phas e. Af ter about 5 min, the r eflections f rom low tempe rature phas e vanis hed. Mn-O3 length indicates an anis otropic nature along the *c*-axis by Jahn-Teller effect of Mn^{3+} ion in Table 1. Crystallographic data s hows that the Mn-O2 distances are obviously elongated about 1 % at 1173 K. A small expansion of *c*-length was also observed at 1173 K by heating process, as shown in Fig. 2(b). The changes in the cell dimensions suggest that the transition is irreversible. In general, phase transition is accompanied by tilting of the MnO_6 octahedra in perovskite and the symmetries change in the octahedral tilt system. In this case, however, the first-order phase transition occured in the structure of $BaPr_2Mn_2O_7$ (*I*4/*mmm*) with no-tilting of the octahedra.

Similar pha se tra nsition o f fi rst-order wa s obs erved in B a$Gd_2Mn_2O_7$ [4] a nd B a$Eu_2Mn_2O_7$. Multiple pha se tra nsitions we re obs erved in B a$Eu_2Mn_2O_7$, with one f rom $P4_2/mnm$ to *I*4/*mmm* at around 400 K and another , above 550 K , as s hown in F ig.3. The s pace-group o f phas e I I was assumed to be *I*4/*mmm*. With increasing temperature, we found the phase transition in the next step. The *I*4/*mmm* phase was stable in a narrow temperature region. Pattern (b) changed into pattern (c), which was assumed to be $P4_2/mnm$. Then, a new phase III n ucleated in the low-temperature phase matrix at 550 K. The complex patter n (d) can be interpreted as a mixtur e of the low- temperature phase (c) and the high- temperature phase (e). The pattern (e) is compos ed of twinning r otatied by 90 degr ees, and i t indicates t hat t he equi valence bet ween *a*- a nd *b*- axis br oke down. T he high-temperature phas e is as umded to be monocl inic s tructure, as s een in annealing s pecimen of $BaTb_2Mn_2O_7$ [7].

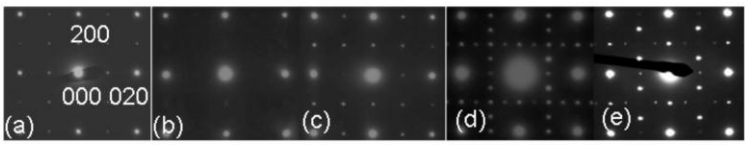

Fig.3 SAED patterns of $BaEu_2Mn_2O_7$ along the [001] zone axis taken at various temperatures: (a) RT for phase I, (b) 433 K for phase II, (c) 500 K, (d) 550 K, and (e) 773 K for phase III.

In this experiment, we succeeded to record the structural change of $BaGd_2Mn_2O_7$ by a video system. Figure 4 shows the *in-situ* TEM observation of the structural changes along the c- axis above 500 K. At 500 K, the TEM image shows a single phase grain constructed by a low temperature (L.T.) phase. At 773 K, the high- temperature (H.T.) phase appeared with a dark contrast parallel to the (00*l*) plane as a layer, and weak reflections were observed in the SAED pattern as indicated by an arrow. The H.T. phase grew until covering the entire inspected region at around 1023 K. We suggest that the first-order phase transition was caused by the structural and/or electrical distortion of the layered perovskite structure composed of Jahn-Teller ion Mn^{3+}.

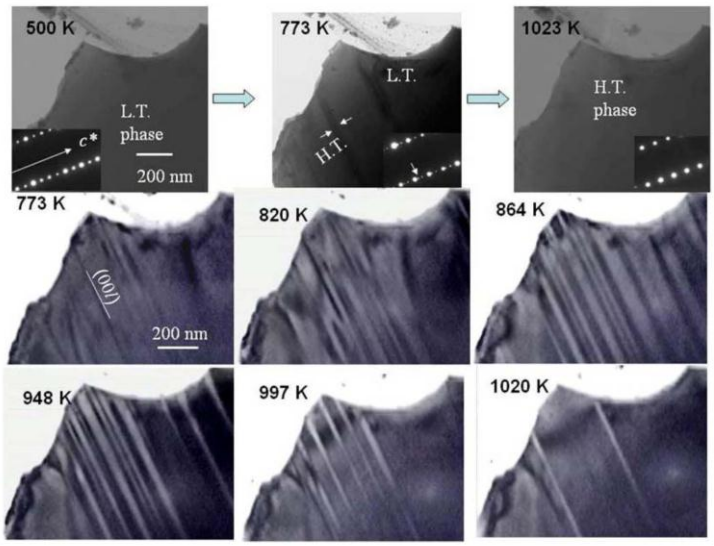

Fig.4 Structural changes in $BaGd_2Mn_2O_7$ from 500 K to 1023 K. (Heating rate is about 0.7 K/sec).

Conclusion

We found a novel phase transition in $BaLn_2Mn_2O_7$ (Ln = Pr, Gd, Eu) using a high-temperature TEM and high- temperature XRD. The phase transition was observed even in $BaPr_2Mn_2O_7$ with a prototype structure *I*4/*mmm* above 1040 K. Multiple phase transitions were also observed in Eu- and Gd- manganites. The high-temperature phase of Gd-manganite nucleated parallel to the (00*l*) plane as a layer and grew until covering the entire inspected region. The phase trasition was of the first-order and irreversible transition.

We wolud like to thank Mr. S. Kondo and Mr. T. Suwa of Nagoya Institute of Technology for helpful XRD measurements. This work was partially supported by a Grant-Aid for Scientific Research (c) No.21560704 by the Japan Society of the Promotion of Science.

References

[1] M. N. Deshizeaux Cheruy, and J. C. Joubert: J. Solid Satate Chem. Vol. 40, (1981), p.14.

[2] N. Kamegashira, H. Nakano, G. Chan, and J. Meng: J. Rare earths, Vol. 22(5), (2004), p. 582.

[3] N. Kamegashira, Shokubai: Vol. 31(4), (1989) p. 222. [in Japanese]

[4] H. Nakano, N. Ishizawa, N. Kamegashira, and M. Yashima: J. Am. Ceram. Soc. Vol. 90(4), (2007), p. 1342.

[5] H. Nakano and N. Kamegashira: J. Rare Erath, Vol. 24(S), (2006), p. 1.

[6] K. S. Aleksandrov and J. Bartolome: J. Phys. Condens. Matter, Vol. 6, (1994), p. 8219.

[7] N. Kamegashira, H. Satoh, J. Meng, and T. Mikami: J. Alloys and Compds. Vol. 374, (2004), p. 173.

Advances in Science and Technology Vol. 63 (2010) pp 47-51
© (2010) Trans Tech Publications, Switzerland
doi:10.4028/www.scientific.net/AST.63.47

In-situ TEM Observation of Crystallization Process for $LiNbO_3$ and $NaNbO_3$

Hiromi Nakano[1a], Yoko Suyama[2b]
[1]Toyohashi University of Technolog, Tempaku, Toyohashi, 441-8580, Japan
[2]Shimane University, Nishikawatsu-cho, Matsue, 690-8504, Japan
[a]hiromi@crfc.tut.ac.jp, [b]suyama@riko.shimane-u.ac.jp

Keywords: High-temperature TEM, nano-grain, microstructure, in-situ observation

Abstract. Fabrication of advanced electronic components requires high-quality powders. In this work, nano-powders of Li or Na niobates are synthesized from (Li or Na)-Nb ethoxide by a sol-crystal method. A single crystal of (Li or Na)-Nb ethoxide is decomposed to an amorphous matrix below 473 K. Next, small crystals are grown by heating at the appropriate temperature for each specimen. The sol-crystal method provides homogeneous quality and fine grains by heating at lower temperature. Structural analysis of the powders is performed by a transmission electron microscope (TEM) and X-ray diffraction. As a result, $LiNbO_3$ turns to dense-powders, but $NaNbO_3$ forms nano-porous powders. In order to understand this difference, we try to observe *in-situ* the crystallization and grain growth processes by high-temperature TEM. We successfully observe in-situ this processing and discuss the structural change and formation mechanism of $LiNbO_3$, comparing these features with those of $NaNbO_3$.

Introduction

Lithium niobate ($LiNbO_3$) is known as an important ferroelectric material because of its piezoelectrical, electro-optical, and photo-refractive properties [1]. $LiNbO_3$-$NaNbO_3$ and $NaNbO_3$-based piezoelectric ceramics have been investigated as Pb-free materials [2–4]. Fabrication of advanced electrical components requires high-quality powders, which must provide homogeneous quality, fine grains, and uniform grain size. In the case of $LiNbO_3$, the conventional process requires high sintering temperature and causes Li_2O loss. Suyama et al. reported a new preparation route for the compounds $BaTiO_3$ and $Ba_5Nb_4O_{15}$, in which those compounds could be successfully synthesized from double-metal alkoxides [5, 6]. This method could achieve synthesis at low temperature and obtain fine particles. In our previous study, $NaNbO_3$ nano-porous grains were synthesized by the sol-crystal method [7]. Optical and electrical properties of ceramics are strongly influenced by the structural defects and morphology [8]. For improving the morphology and microstructure, the crystallization process should be controlled under the experimental condition. However, the crystallization behavior is not well understood.
In this study, the crystallization behavior and microstructure were investigated by TEM and high-temperature TEM for $LiNbO_3$ nano-dense grains prepared by the sol-crystal method. Consequently, the obtained features were compared with those of $NaNbO_3$.

Experimental Procedure

$Nb(OEt)_5$ and (Li or Na)(OEt) were synthesized in ethanol from Nb_2O_5 and Li or Na metal, respectively. A crystal of (Li or Na)-Nb ethoxide was obtained from $Nb(OEt)_5$ and (Li or Na)(OEt). This procedure has been reported in detail elsewhere [7]. The crystal was annealed at 373–1173 K in air for 1.5 h.
Those specimens were structurally analyzed by powder XRD (Rigaku RINT-2100SL) with CuKα radiation and a high-resolution TEM (JEM-2100F, JEOL) equipped with energy-dispersive spectroscopy (EDS). The decomposition behaviors of Li-Nb and Li-Na-Nb ethoxides were measured by TG-DTA (Rigaku TG8120).

The crystallization process was observed *in-situ* by TEM (JEM-2000EX) using a thermal stage (EM-SHH4). The temperature on the stage was controlled manually from room temperature to 1038 K. TEM images were recorded in real time with a video camera.

Results and discussion

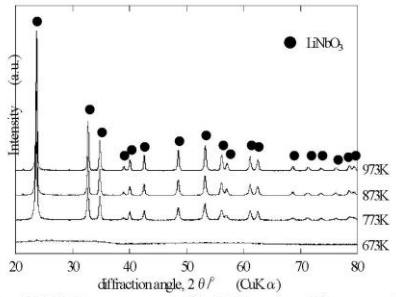

Fig. 1 XRD patterns of Li-Nb ethoxide annealed at various temperatures for 1.5 h.

Rectangular-shaped crystals of Li-Nb ethoxide with sizes of 1–5 mm were heated for 1.5 h. Figure 1 shows powder XRD patterns of specimens annealed at various temperatures. These crystals were decomposed to an amorphous state by heating. At >773 K, small peaks appeared, which indicated the existence of $LiNbO_3$ crystals with a rhombohedral phase (a = 0.5148 nm, c = 1.3863 nm as a hexagonal cell)[Inorganic crystal structure database ICSD#28294]. An exothermic peak was detected at 758 K by TG-DTA measurement, possibly indicating the crystallization temperature of $LiNbO_3$.

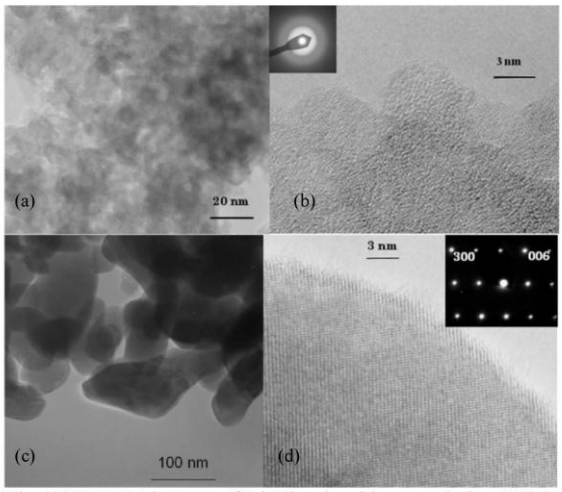

Fig. 2 HRTEM images of Li-Nb ethoxide annealed at 553 K in (a) and (b), and at 873 K in (c) and (d).

To determine the exact temperature at which the crystals begin to form in the amorphous matrix, microstructures were observed by TEM. Figure 2 shows TEM images of Li-Nb ethoxide annealed at 553 K and 873 K. At <553 K, the specimen was an amorphous state. At 553 K, small crystalline grains were observed in the amorphous matrix, as shown in (b). At 673 and 773 K, crystalline sizes grew, but an area having an amorphous state was also observed. The specimen annealed at 673 K was a porous material, like $NaNbO_3$ grains. At 873 K, the grains grew to an average of 100 nm, where the phase was a crystal with a rhombohedal cell, as seen in the selected area electron diffraction pattern (SAED) in (d). The specimen was a dense material, and no defect was observed in the grains.

Next, we attempted to observe the crystallization *in-situ* and the grain growth process by the thermal stage in TEM. The starting material used was a specimen annealed at 673 K. Figure 3 shows the changes in the microstructure of the crystalline phase during TEM observation from ambient temperature to 1038 K.

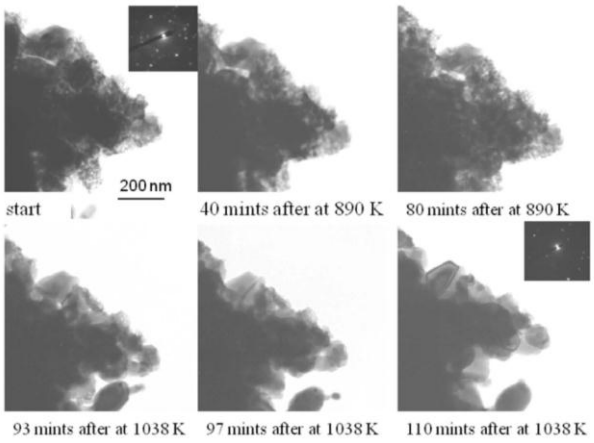

Fig. 3 Structural changes in the specimens by heating in TEM. Starting material used is a specimen annealed at 673 K for 1.5 h in air.

The heating rate was 890 K/30 min, and the temperature was maintained for 80 min at 890 K. After that, the temperature was raised to 1038 K and then the grains grew earlier. On the other hand, $NaNbO_3$ was fully transformed to a crystalline state at 773 K. The $NaNbO_3$ crystalline grains included inner-pores because some pores remain in the matrix, as a previous paper describes [7]. In the present case, the temperature was higher than that of $NaNbO_3$, and thus the inner-pore moved out during grain growth. *In-situ* observation data revealed the grain-growth process, although it was done under a high vacuum. Actually, the crystallization process of $LiNbO_3$ may be influenced by the oxidation condition because the stoichiometory was controlled [9].

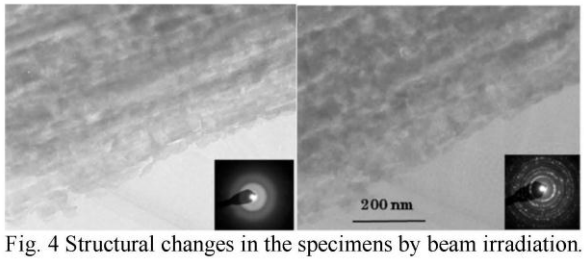

Fig. 4 Structural changes in the specimens by beam irradiation.

We found that the amorphous state changed to a crystalline state by the irradiation of a converged beam in TEM. Figure 4 shows structural changes in the specimen by beam irradiation. Starting material was annealed at 553 K as an amorphous state. This shows that the state of the specimen might be unstable and transform easily to a crystalline state by a small thermal impact. Therefore, we attempted to observe the crystallization process *in-situ* at the atomic scale by beam irradiation. The current density was controlled; the amorphous state transformed into a crystalline phase during the irradiation at current density of 15 pA/cm^2, and then this change stopped below 10 pA/cm^2. Some HRTEM images could be taken by controlling the beam irradiation. Figure 5 shows the crystallization process of $LiNbO_3$ at the atomic scale. Starting material was a polycrystalline grain in (a). After irradiation, the atomic arrangement changed along the arrow in (b), and the atom diffused perpendicular to the $(1\bar{2}0)$ indicated by the arrow in (c). Finally, the grain became a single phase, and a twin-grain boundary formed on the (113) in (d). Hirao et al. reported that $LiNbO_3$ crystalline film could be synthesized from double-alkoxide at 523 K by controlling the synthesizing condition and heating atmosphere [10]. Terabe et al. showed the crystallization temperature at about 573 K and a fully transformed crystalline state at about 753 K in sol-gel $LiNbO_3$ film [8]. Our experimental data corresponded to the latter, and the dense bulk grain could not be obtained at a lower temperature.

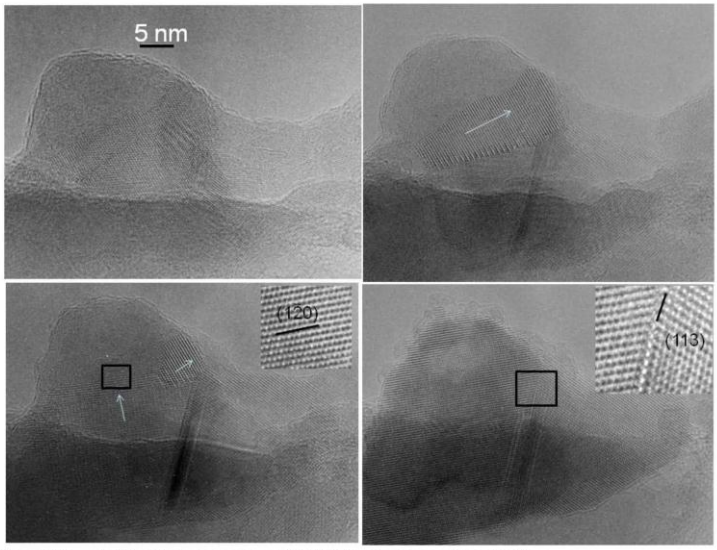

Fig. 5 Crystallization process of $LiNbO_3$ by beam irradiation.

Summary

We clarified the crystallization and grain-growth mechanism in $LiNbO_3$ from Li-Nb ethoxide by *in-situ* TEM observation. The difference in morphology between $LiNbO_3$ and $NaNbO_3$ was caused by crystallization temperature. At lower temperature, crystallization of the $LiNbO_3$ was possible, but a dense grain was not expected. These data will be useful for designing $LiNbO_3$-$NaNbO_3$ hybrid material.

This work was partially supported by a Grant-Aid for Scientific Research (c) No.21560704 by the Japan Society of the Promotion of Science.

References

[1] R. S. Weis and T. K. Gaylord: Appl. Phys., Vol. A37, (1985), p. 191.

[2] L. Pardo, P. Duran-Martin, J. P. Mercurio, L. Nibou, and B. Jimenez: J. Phys. Chem. Solids., Vol. 58(9), (1997), p.1335.

[3] L. Nibou, M. Manier, and J. P. Mercurio: Ann. Chem. Sci. Mat. Vol. 23, (1998), p. 135.

[4] K. Kusumoto: Jpn. J. Appl. Phys. Vol. 46(10B), (1997), p.7094.

[5] Y. Suyama and N. Nagasawa: J. Am. Ceram. Soc. Vol.77(2) (1994), p.603.

[6] H. Nakano, T. Yano, Y. Suyama: J. Ceram. Soc. Jpn., Vol. 113(1),(2005), p.59.

[7] H. Nakano, Y. Hirano, Y. Suyama: J. Soc. Mater. Sci. Jpn. Vol. 56(6), (2007), p.500.[in Japanese]

[8] K. Terabe, A. Gruverman, Y. Matsui, N. Iyi, K. Kitamura: J. Mater. Res. Vol.11(12), (1996), p. 3152.

[9] A. Z. Simoes, M. A. Zaghete, B.D. Stojanovic, A. H. Gonzalez, C. S. Riccardi, M. Cantoni, J. A. Varela: J. Europ. Ceram. Soc. Vol.24, (2004), p.1607.

[10] S. Hirano: Electronic Ceramics, Vol.(9), (1991),p.20.[in Japanese]

機能発現メカニズムの解明に関連する研究成果

Surface & Coatings Technology 206 (2011) 366–371

Contents lists available at ScienceDirect

Surface & Coatings Technology

journal homepage: www.elsevier.com/locate/surfcoat

The effect of post-treatments on the powder morphology of titanium dioxide (TiO_2) powders synthesized for cold spray

N. Tjitra Salim [a,*], M. Yamada [b], H. Nakano [c], K. Shima [b], H. Isago [b], M. Fukumoto [b]

[a] Venture Business Laboratory, Toyohashi University of Technology, 1-1, Tempaku-cho, Toyohashi, Aichi, 441-8580, Japan
[b] Mechanical Engineering, Toyohashi University of Technology, 1-1, Tempaku-cho, Toyohashi, Aichi, 441-8580, Japan
[c] Cooperative Research Facility Center, Toyohashi University of Technology, 1-1, Tempaku-cho, Toyohashi, Aichi, 441-8580, Japan

ARTICLE INFO

Article history:
Received 14 April 2011
Accepted in revised form 12 July 2011
Available online 23 July 2011

Keywords:
Titanium dioxide
Hydrolysis
Nanostructure
Cold spray

ABSTRACT

In this study, a novel synthesis method of TiO_2 powders that can be cold sprayed is presented. The synthesis technique is a simple hydrolysis method of titanyl sulfate ($TiOSO_4$) in distilled water with a small addition of inorganic salt. At a relatively low hydrolysis temperature, pure anatase TiO_2 can be obtained and post-synthesis treatments (annealing or hydrothermal treatment) do not alter this phase structure. The powder is agglomerated with fine nano primary particles, with different post-synthesis treatments leading to different TiO_2 nanostructures. Annealing causes a significant growth of primary particles with the existence of internal pores within a particle. On the other hand, hydrothermal treatment produces a unique oriented agglomeration structure where the primary particles are agglomerated in one single crystal axes. It is believed that the synergistic effect of inorganic ion adsorption and post-treatments results in the observed nanostructures. After cold spraying, it is revealed that these TiO_2 powders could be deposited via supersonic solid phase deposition (cold spray).

1. Introduction

TiO_2 is a much valued material due to its wide range of applications, especially in the area of photocatalysis, as is widely known for its excellent photocatalytic activity. Due to this unique property, TiO_2 can be applied for numerous environmental purposes, such as self-cleaning surfaces, antifogging materials, water purification, air cleaning, self-sterilization, etc. A TiO_2 coating covering a large surface area is desirable for most photocatalytic applications. Thermal spray process has been used widely for the fabrication of thick and large area coatings, including the fabrication of thick TiO_2 coatings [1,2]. However, these coatings were not targeted for the photocatalysis application as they possessed low photocatalytic activity due to the nature of thermal spray process that required the particles to be in the molten state. The melting temperature of TiO_2 is 1908 °C, however, at 900 °C, TiO_2 undergoes a phase transformation from anatase structure (higher photocatalytic activity) to rutile structure (lower photocatalytic activity). Due to this reason, the solid phase cold spray deposition method is more suitable to produce pure anatase TiO_2 coating for photocatalytic application. Cold spray deposition is a coating fabrication technique that uses a supersonic gas stream to accelerate the feedstock particles [3]. It is purely a solid phase deposition method hence, no melting of feedstock material. For the case of TiO_2 coating, the high photocatalytic anatase structure can be retained in the coating by the use of a cold spraying technique.

However, it is well known that cold spraying ceramic materials can be difficult. Cold spraying requires plastic deformation of the feedstock particles for adhesion to the substrate. However, it is difficult to plastically deform hard and brittle ceramic materials, such as TiO_2. Previous studies have reported the possibility of cold spraying TiO_2, however, defined coatings were not obtained [4,5]. Rather than adhesion, it was observed that particles were only embedded in the grooves of the substrates. A thick defined TiO_2 coating can be achieved via cold spraying when vacuum cold spray is used [6] and/or organic binder material is added to agglomerate the TiO_2 feedstock powder [7]. The binder materials would provide the ductility to assist with the plastic deformation upon collision. From these observations, one can deduce that cold spraying of TiO_2 can be done by modifying the cold spray equipment (in vacuum) or modifying the feedstock material. In this study, we are reporting the novel synthesis method of TiO_2 powder for cold spray without the addition of a binder. The synthesized powder can be cold sprayed without the need of vacuum.

It is known that TiO_2 powder can be synthesized using various methods, such as the sol–gel hydrolysis of Ti alkoxides [8,9] and Ti chloride [10], flame pyrolysis of volatile Ti compounds [11], etc. All of these methods are generally complicated which would require the use of various reagents and high temperatures. Our synthesis technique is a much simpler method that involves the reaction of titanyl sulfate ($TiOSO_4$) and water, also known as hydrolysis reaction, to obtain TiO_2 powder.

* Corresponding author. Tel/fax: +81 532 81 5118.
E-mail address: noviana@isf.me.tut.ac.jp (N.T. Salim).

0257-8972/$ – see front matter © 2011 Elsevier B.V. All rights reserved.
doi:10.1016/j.surfcoat.2011.07.030

2. Experimental method

10 wt.% of $TiOSO_4$ was mixed with distilled water to perform the hydrolysis reaction. Ammonium sulfate $[(NH_4)_2SO_4]$ was added during hydrolysis. The solution was stirred on a hot plate to hold the temperature at 120 °C for 8 h after which a white precipitate formed. The precipitate was then dried in an oven for 10 h at 120 °C to obtain a powder. The powder was post-treated to improve its crystallinity via two methods: the hydrothermal treatment; and annealing at 600 °C for 1 h. The hydrothermal treatment was performed by soaking the TiO_2 powder with distilled water in an autoclave and heat-treated at 150 °C for 5 h. The crystal phase of the synthesized powders from the two methods was characterized using X-Ray Diffraction (XRD: RINT 2500, Rigaku), while the powder morphologies were analyzed by Field Emission Scanning Electron Microscope (FE-SEM: SU8000, Hitachi, accelerating voltage 5 kV) and Transmission Electron Microscope (TEM: JEM-2100F, JEOL, accelerating voltage 200 kV). X-ray Photoelectron Spectroscopy (XPS: Quantera SXM-CI, ULVAC-Phi, Inc.) was used to study the chemical composition and bonding of powders. The XPS provided useful information in order to explain the formation of the powders' nanostructures.

The powders were then deposited via cold spray process using the conventional cold spray parameters on custom-made cold spray equipment built in our laboratory. Nitrogen at 500 °C and 1 MPa was used as the process gas. A grit blasted pure copper metal was used as the substrate. After cold spraying, the coatings' cross section was observed using the scanning electron microscope (SEM: JSM-6390TY JEOL Co. Ltd.) to determine the coating thicknesses.

3. Results and discussion

The XRD spectra in Fig. 1 reveal that the synthesized TiO_2 has a single phase anatase structure and this phase is retained even after post-synthesis treatments. Single phase anatase structure is highly desirable for photocatalysis application. Improvement in crystallinity is observed after post-treatments, indicated by the sharper and greater attenuation of diffraction peaks. Such improvement due to annealing or hydrothermal treatment is not surprising and has been reported widely [12,13]. Annealing results in higher degree of powder crystallinity compared to hydrothermal treatment due to the larger primary particle size. The crystallite sizes calculated using the Scherrer's equation were 9, 12 and 15.6 nm for as-synthesized, hydrothermal treated and annealed TiO_2 powder, respectively. Post-treatment clearly increases the particle size and annealing post-treatment increases the particle size more than hydrothermal treatment.

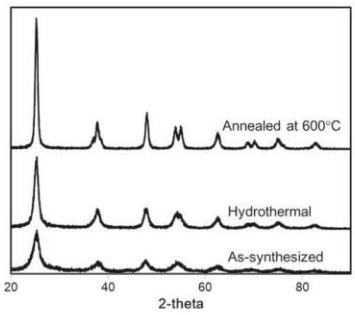

Fig. 1. The XRD spectra of as-synthesized, hydrothermal treated and annealed TiO_2 powders.

Fig. 2 shows the powder morphologies obtained by the FE-SEM. The synthesized TiO_2 powders have an agglomerated structure consisting of very fine nano primary (1°) particles. The nanoparticles are agglomerated to form the secondary (2°) particle with a size of about 2 μm. These 2° particles are further agglomerated into tertiary (3°) particles with a size of 17 μm as shown in Fig. 2a–c. The FE-SEM image also indicates that post-treatments do not alter the structure and size of the 2° and 3° particles. On the contrary, the higher magnification images in Fig. 2d–f show the growth of 1° particles structure into more well-defined crystals after post-treatments, confirming the increase in 1° particle size due to post-treatments. The higher magnification images also reveal larger particle size of annealed TiO_2 (Fig. 2e) than hydrothermal TiO_2 (Fig. 2f).

From the TEM images in Fig. 3, the 1° particle sizes of as-synthesized, hydrothermal treated and annealed powders were determined to be about 3, 5 and 25 nm, respectively. The 1° particle sizes determined by the Scherrer's equation and TEM are fairly different. The TEM provides direct observation of particles, although possible artifacts that are related to sampling are possible. Moreover, the contrast can cause problems in distinguishing smaller particles, especially smaller particles in agglomerates [15]. On the contrary, the particle size obtained by the Scherrer's equation may be even less accurate than the direct observation of TEM images. The Scherrer's equation uses the diffraction peak broadening of XRD spectra. The peak broadening can be caused by microstrains (lattice deformation), faulting, and/or crystal size [15]. The Scherrer's equation assumes that particles are free from strains and faulting which is not necessarily true. Hence, this study would refer mostly to the 1° particle size obtained by direct observation of TEM images instead of the ones measured by Scherrer equation.

As-synthesized, the TEM image in Fig. 3a confirms TiO_2 powder with very fine 1° nano-particles with an average size of 3 nm. Annealing is a rapid crystallization process that promotes grain growth at the expense of smaller crystals (Ostwald ripening) [14], therefore an increase in 1° particle size from 3 nm to 25 nm after annealing at 600 °C is expected and observed (Fig. 3b). Larger grain size indicates fewer amounts of grain boundaries, hence less structural imperfections which in turn would increase crystallinity as observed by the XRD results. The TEM image in Fig. 3b has revealed not only grain growth in the annealed powder, but also the existence of internal pores within 1° particles (as indicated by the arrows).

There is no significant increase in the average 1° particle size observed between TiO_2 powders as-synthesized and after hydrothermal treatment. Hydrothermal treatment is a mild crystallization process occurring at a lower temperature that allows structural rearrangement. As a result, hydrothermal treatment would yield finer particles [14]. Therefore, it does not increase the 1° particle size significantly, an increase from 3 to 5 nm only was observed (Fig. 3a and c). As shown by the XRD (Fig. 1), there is an improvement in crystallinity due to hydrothermal treatment; however the mechanism of improvement in crystallinity is believed to be different from that of the annealed powder which is caused by the physical increase of 1° particle size. The TEM image in Fig. 3c shows a special type of growth in hydrothermal treated powder that involved the agglomeration of 1° particles (~5 nm) within one single crystal axis of a size about 20 nm. This unique particle orientation causes the increase in crystallinity of hydrothermal treated powder.

To understand the mechanism behind formation of these structures due to post-treatments, an XPS study was performed. Fig. 4 is the XPS wide scan spectra of as-synthesized and post-treated TiO_2 powders. Peaks corresponding to Ti 2p, O 1s, S 2p, N 1s and C 2p are observed for all powders. The C 2p peak corresponds to the carbon tape used during XPS observation. The wide scan spectra are useful to determine elemental compositions of the powders. However, it does not provide sufficient information regarding the elemental bonding that exists within the TiO_2 powders. The narrow scan spectra of

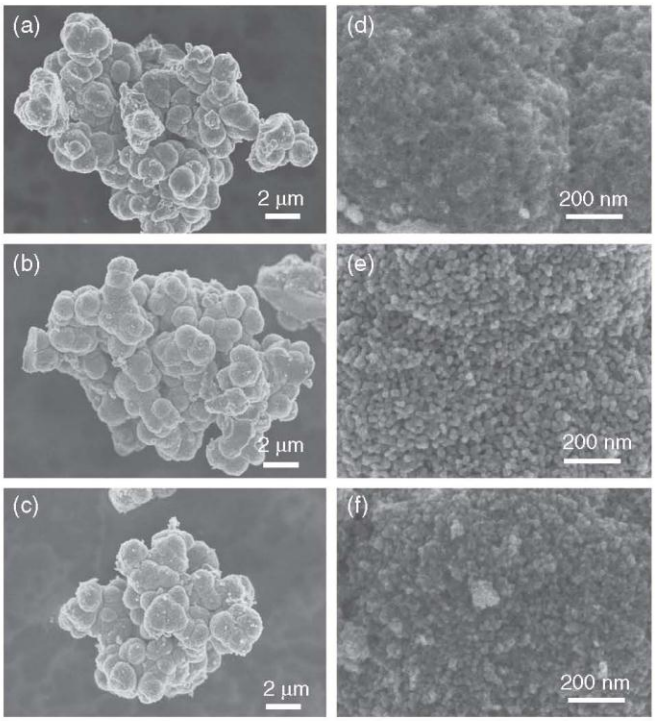

Fig. 2. The FE-SEM images taken at low magnification of (a) as-synthesized, (b) annealed and (c) hydrothermal treated TiO_2 powders; and at high magnification of (d) as-synthesized, (e) annealed and (f) hydrothermal treated TiO_2 powders.

individual elements are required to understand the elemental bonding and are shown in Fig. 5. The Ti 2p narrow scan spectra in Fig. 5a show a peak only at 459.3 eV which corresponds to Ti–O bonding. No other peaks are observed, indicating that Ti is only bonded to O, hence, the S and N compounds observed in the wide scan spectra correspond to compounds adsorbed onto the surface of TiO_2. These adsorbed compounds are detected in powders synthesized with and without post- treatments. The O 1s narrow scan spectra in Fig. 5b confirms the Ti–O bonding with the existence of peak at 531 eV. The O 1s narrow scan spectra also shows a peak at 532.4 eV which corresponds to sulfate (SO_4^{2-}) bonding. Therefore, the S compound detected by the XPS wide scan corresponds to adsorption of SO_4^{2-} ions. The intensity of the peak corresponding to SO_4^{2-} ions decreases with post-treatments, indicating that the SO_4^{2-} ions desorption occurs as a result of post-treatments. The existence of SO_4^{2-} ion adsorption on the surface of TiO_2 and its desorption due to post-treatments are also confirmed by the narrow scan spectra of S 2p in Fig. 5c. Finally, the N 1s narrow scan spectra in Fig. 5d shows a peak at 402.4 eV which corresponds to ammonium (NH_4^+) ion adsorption on the surface of TiO_2. These adsorbed NH_4^+ ions are detected in all TiO_2 powders.

It is believed that the SO_4^{2-} and NH_4^+ ions adsorptions play important roles in the formation of unique structures due to post-treatments. Such structural modification by $(NH_4)_2SO_4$ has been reported by Sun et al. to obtain titania tubes [16].

By observing the change in atomic surface concentrations of S and N between before and after post treatment (Fig. 6), the structural formation mechanism can be explained. The atomic surface concentrations of S and N were obtained by the XPS. As the S and N compounds in TiO_2 powders correspond to SO_4^{2-} and NH_4^+ ions respectively, their change in atomic concentrations caused by post-treatments are good indicators to the change in SO_4^{2-} and NH_4^+ ions concentrations.

Fig. 6 shows that the TiO_2 powders have more S compounds compared to N compounds, indicating more SO_4^{2-} ions than NH_4^+ ions adsorbed on the surface. It is clear that these adsorbed ions originated from the raw materials. The sources of SO_4^{2-} ions are $TiOSO_4$ and $(NH_4)_2SO_4$ while the source of NH_4^+ ions is only from $(NH_4)_2SO_4$. Therefore, it is not surprising that the amount of adsorbed SO_4^{2-} ions is higher compared to NH_4^+ ions. Fig. 6 also reveals the reduction in both S and N atomic concentrations, i.e. SO_4^{2-} and NH_4^+ ion concentrations due to annealing, confirming the desorption of these ions. Annealing provides the energy required not only for grain growth but also for residual ion desorption from the surface of TiO_2. Due to this ion desorption, internal pores observed by the TEM in Fig. 3b are formed. The existence of internal pores within ceramic particles has been observed by other studies [17–19]. Sakabe et al. [18] observed the existence of rectangular shaped pores inside the particles after annealing due to the dissociation of hydroxyl group during heat treatment at moderate temperature (less than 800 °C). Above 800 °C, the particles start to grow and restructuring takes place to create pore defect free particles. In our case, annealing at 600 °C results in ion desorption however, it does not provide sufficient energy for particle growth to occur and fill the pores.

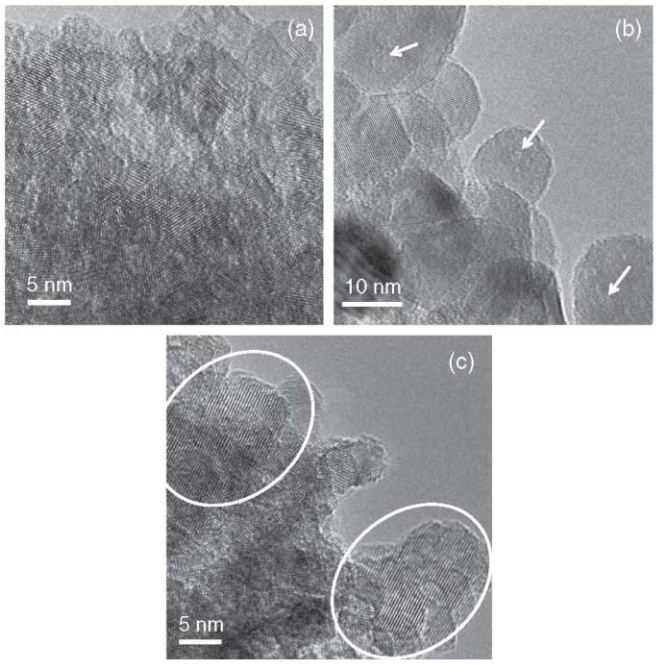

Fig. 3. The TEM images of (a) as-synthesized, (b) annealed and (c) hydrothermal treated TiO_2 powders.

The same approach can be used to explain the formation of unique oriented agglomeration structures due to hydrothermal treatment as observed in Fig. 3c. Fig. 6 also shows the concentration of S and N between as-synthesized and after hydrothermal treatment. After hydrothermal treatment, the graph clearly shows the reduction in the concentration of S content, i.e. SO_4^{2-} ions, confirming SO_4^{2-} ions desorption due to hydrothermal treatment, similar to the annealed powder. The hydrothermal treatment also provides sufficient energy for the desorption of SO_4^{2-} ions from the surface of TiO_2. While it reduces the amount of adsorbed SO_4^{2-} ions, there is no significant change in the amount of adsorbed NH_4^+ ions after hydrothermal treatment, indicated by the minor change in N concentrations of as-synthesized and hydrothermal treated powders (Fig. 6). It is believed that hydrothermal treatment provides the energy and time required for electrostatic attraction between adsorbed NH_4^+ and SO_4^{2-} ions to take place and as a result, this would allow the TiO_2 primary particles to rotate and orient in a single crystal axis as observed by the TEM. This concept is illustrated in Fig. 7. Therefore, the concentration of NH_4^+ ions would remain relatively constant even after hydrothermal treatment. As there is higher amount of SO_4^{2-} ions initially compared to NH_4^+ ions, there would be some SO_4^{2-} ions unbound and these unbound ions are desorbed out from TiO_2 surface, as confirmed by the reduction in S concentration, i.e. SO_4^{2-} ions after hydrothermal treatment (Fig. 6).

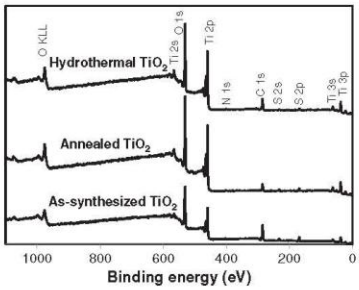

Fig. 4. The XPS wide scan spectra of as-synthesized, annealed and hydrothermal treated TiO_2 powders.

Crystal growth via oriented agglomeration due to hydrothermal treatment and surface adsorptions has been reported [12,20]. Huang et al. [12] synthesized an oriented agglomerated ZnS through the hydrothermal treatment of mercaptoethanol-stabilized ZnS nanoparticles. Penn et al. [20] also showed the formation of oriented agglomerated TiO_2 due to hydrothermal coarsening. They have recognized that depending on the molecules adsorbed, it may enhance or hinder oriented agglomeration. In this case, we have also shown the synergistic effect of hydrothermal coarsening and NH_4^+ and SO_4^{2-} ions adsorption to form oriented agglomerated TiO_2. It is believed that oriented agglomeration is formed to reduce the overall surface energy by elimination of surfaces at which crystals join. The presence of water during hydrothermal treatment assists with the movement of particles via Brownian motion and the thermal energy provides driving force for particle movements [12,20]. Concurrently, the mobile particles would need to reorient and agglomerate to reduce the overall surface energy by rotating themselves [20]. Particle rotation is induced by the electrostatic

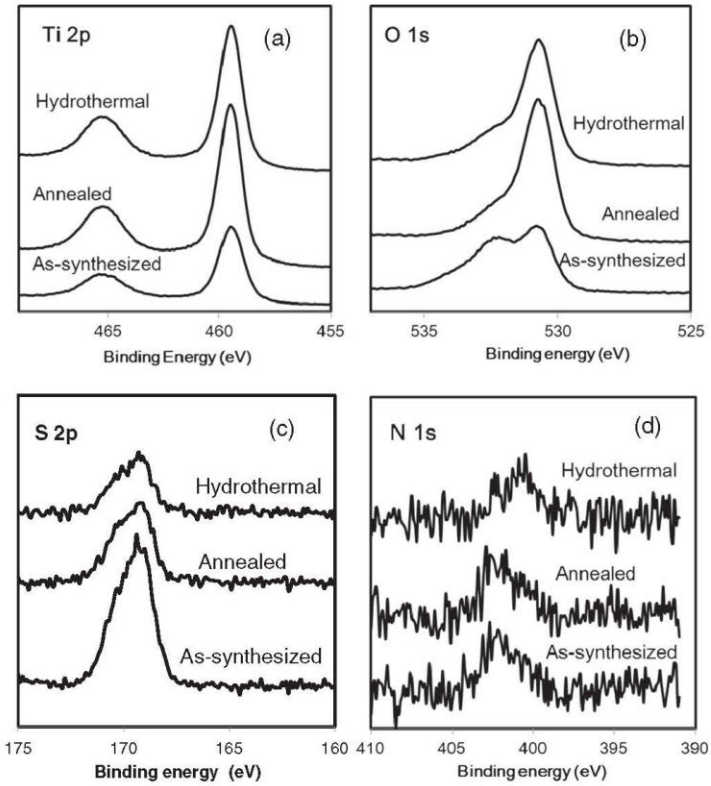

Fig. 5. The XPS narrow scan spectra of as-synthesized, annealed and hydrothermal treated TiO_2 powders for corresponds to (a) Ti 2p, (b) O 1s, (c) S 2p and (d) N 1s.

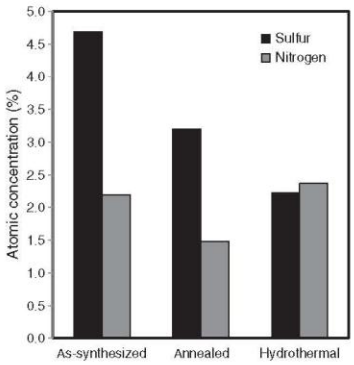

Fig. 6. The atomic concentrations of sulfur and nitrogen in the as-synthesized, annealed and hydrothermal treated TiO_2 powders.

attraction between adsorbed NH_4^+ and SO_4^{2-} ions. Such crystal growth is very different with the one observed in the annealed powder, where grain growth occurs as a result from dissolution of fine particles to form larger particles.

TiO_2 powders with unique structures for cold spray process have been synthesized and its formation mechanism has been studied thoroughly. It is of interest to confirm the deposition of these powders via supersonic solid phase deposition technique (cold spray). Fig. 8 shows the SEM cross sectional images of the three cold sprayed TiO_2 powders on copper substrate. Cold spray coating was not obtained by

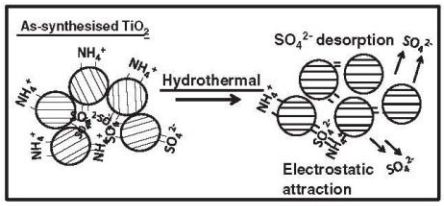

Fig. 7. The formation mechanism of oriented agglomeration TiO_2 created after hydrothermal post-treatment.

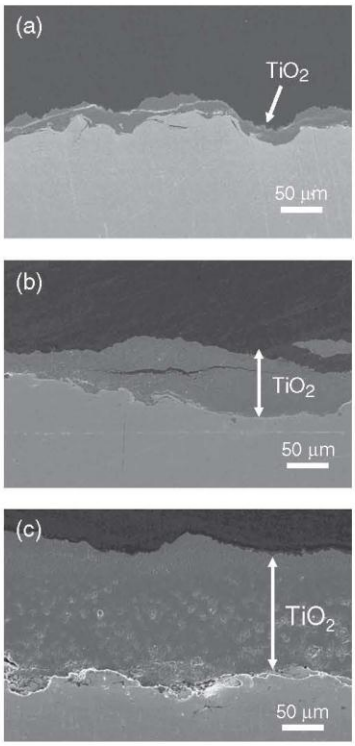

Fig. 8. The cold spray result of (a) as-synthesized, (b) annealed, and (c) hydrothermal treated TiO_2 powders deposited on copper.

the as-synthesized powder, instead only particle embedment was observed as shown in Fig. 8a. On the contrary, the post-treated powders formed more defined and thicker coatings (Fig. 8b–c). When deposited using the same cold spray parameters, the hydrothermal treated TiO_2 (Fig. 8b) formed a thicker coating of about 150 μm than the annealed TiO_2 (Fig. 8c) with a coating thickness of about 75 μm. It is believed that the oriented aggregated structure of hydrothermal TiO_2 is the crucial factor causing thick deposition of TiO_2 coating via cold spray. These results are remarkable, showing that we have successfully discovered a novel synthesis method to produce a cold-sprayable TiO_2, by fine-tuning the nano-structure of TiO_2.

4. Conclusion

In summary, we have synthesized anatase TiO_2 powder that can be cold sprayed. The powder is agglomerated and consisted of nano 1° particles. We believe that the synergistic effects of NH_4^+ and SO_4^{2-} ion adsorption on surface of TiO_2 combined with post-treatments result in the formation of the special nanostructures of TiO_2 described in this paper. Internal pores are observed as a result of ion adsorption and annealing, while the combined effect of hydrothermal treatment and ion adsorption results in the oriented agglomerated structure. These unique structures have been proven to be cold sprayable. The deposition of TiO_2 via cold spray without the addition of binder and vacuum process is a breakthrough. To date, no other research groups have shown such achievement.

References

[1] A. Ibrahim, R.S. Lima, C.C. Berndt, B.R. Marple, Surf. Coat. Technol. 201 (2007) 7589.
[2] R.S. Lima, B.R. Marple, Surf. Coat. Technol. 200 (2006) 3428.
[3] A. Papyrin, V. Kosarev, S. Klinkov, A. Alkhimov, V. Fomin, Cold Spray Technology, Elsevier Science, 2006.
[4] J. Han, S.W. Lee, E.A. Lee, T. Xiong, Z. Bao, H. Du, Mater. Sci. Forum 510–511 (2006) 130.
[5] I. Burlacov, J. Jirkovsk'y, L. Kavan, R. Ballhorn, R.B. Heimann, J. Photochem. Photobiol. A 187 (2007) 285.
[6] S.Q. Fan, C.J. Li, G.J. Yang, L.Z. Zhang, J.C. Gao, Y.X. Xi, J. Therm. Spray Technol. 16 (2007) 893.
[7] G.J. Yang, C.J. Li, F. Han, W.Y. Li, A. Ohmori, Appl. Surf. Sci. 258 (2008) 3979.
[8] M.R. Mohammadi, D.J. Fray, A. Mohammadi, Microporous Mesoporous Mater. 112 (2008) 392.
[9] S. Gelover, P. Mondragón, A. Jiménez, J. Photochem. Photobiol. A 165 (2004) 241.
[10] Q.-H. Zhang, L. Gao, J.-K. Guo, NanoStruct. Mater. 11 (1999) 1293.
[11] S.E. Pratsinis, P.T. Spicer, Chem. Eng. Sci. 53 (1998) 1861.
[12] F. Huang, H. Zhang, J.F. Banfield, Nano Lett. 3 (2003) 373.
[13] C. Su, B.-Y. Hong, C.-M. Tseng, Catal. Today 96 (2004) 119.
[14] C.C. Wang, J.Y. Ying, Chem. Mater. 11 (1999) 3113.
[15] A. Weibel, R. Bouchet, F. Boulc'h, P. Knauth, Chem. Mater. 17 (2005) 2378.
[16] J. Sun, L. Gao, Q. Zhang, J. Mater. Sci. Lett. 22 (2003) 339.
[17] H. Nakano, K. Urabe, T. Oikawa, H. Ikawa, J. Am. Ceram. Soc. 87 (2004) 1594.
[18] Y. Sakabe, N. Wada, J. Ikeda, Y. Hamaji, Proceedings of ISAF 11th IEEE, Montreaux, Switzerland, 1998 565.
[19] D. Hennings, S. Schreinemacher, J. Eur. Ceram. Soc. 9 (1992) 41.
[20] R.L. Penn, J.F. Banfield, Geochim. Cosmochim. Acta 63 (1999) 1549.

journal

J. Am. Ceram. Soc., **94** [8] 2339–2343 (2011)
DOI: 10.1111/j.1551-2916.2010.04373.x

Microstructural Evidence of Hall Mobility Anisotropy in *c*-Axis Textured Al-Doped ZnO

Yoshiaki Kinemuchi,[†,‡] Hiromi Nakano,[§] Hisashi Kaga,[‡] Satoshi Tanaka,[¶] Keizo Uematsu,[¶] and Koji Watari[‡]

[‡]National Institute of Advanced Industrial Science and Technology, Advanced Manufacturing Research Institute (AIST), Nagoya 463-8560, Japan

[§]Cooperative Research Facility Center, Toyohashi University of Technology, Toyohashi 441-8580, Japan

[¶]Department of Materials Science and Technology, Nagaoka University of Technology, Nagaoka 940-2188, Japan

The high electrical conductivity, 1150 S/cm at room temperature, in the *ab*-plane of *c*-axis textured Al-doped ZnO is attributed to its high Hall mobility that is almost double the mobility in the *c*-axis direction. Temperature-independent mobility in the *ab*-plane below 200 K suggests that ionized impurity dominates the scattering of electron transport, which reasonably agrees with a modified Brooks–Herring–Dingle model taking into account nonparabolic *E–k* dispersion. However, the pronounced anisotropy between *ab*-plane and *c*-axis cannot be expected based on the model. Detailed observations of the grain boundary (GB) by means of high-resolution transmission electron microscopy, high-angle annular dark-field scanning transmission electron microscopy, and energy-dispersive X-ray spectroscopy revealed the existence of an Al-enriched, Zn-deficient layer near the GB traversing the *c*-axis direction. In contrast, the highly conductive direction encompasses a tilt grain boundary, in which coincident sites were observed and Al segregation was barely evident. We conclude that such a preferential segregation in the GB and/or GB structure itself are responsible for the anisotropy of mobility in the textured Al-doped ZnO.

I. Introduction

The well-known zinc oxide is an *n*-type semiconductor whose conductivity is effectively enhanced by Al[1,2] or Ga[3] impurity doping, which is promising for practical applications such as thermoelectric materials or transparent conductive oxides.

We previously reported that for highly *c*-axis oriented Al-doped ZnO ceramics, textured by magnetic alignment, the electrical conductivity at room temperature along the *ab*-plane, i.e., the basal plane of ZnO, increased to >1000 S/cm, which was almost twice that along the *c*-axis.[4–6] This high conductivity along the *ab*-plane originated from a high mobility of ~90 $cm^2/V \cdot s$. In addition, the conductivity was found to be a function of the degree of orientation: a higher degree of orientation resulted in a higher level of conductivity. However, an analysis based on a tensor calculation indicated that the orientation of the crystallite was not responsible for the enhancement in conductivity.[4] A study on the Hall mobility of ZnO single crystal without doping reported nearly isotropic properties above room temperature, supporting our analysis.[7]

A probable mechanism for the anisotropy of the textured Al–ZnO is the difference in scattering at the grain boundary, which generally originates in the structure and/or the chemical homogeneity at the grain boundary (GB).

In order to solve the uncertainty in the textured Al-doped ZnO system, we performed detailed observations on GBs using high-resolution transmission electron microscopy (HRTEM), high-angle annular dark-field scanning transmission electron microscopy (HAADF-STEM), and energy-dispersive X-ray spectroscopy (EDS). Hall measurement was also carried out to clarify the anisotropy in mobility.

II. Experimental Procedure

C-axis textured Al-doped ceramics were prepared via the magnetic field alignment method. Nominal composition of the ceramics was $Al_{0.02}Zn_{0.98}O$, which was prepared from commercial ZnO powder adding γ-Al_2O_3 of 1 mol%. Details of sample preparation can be found elsewhere,[6] but briefly, the procedure was as follows. Because of the anisotropic magnetic susceptibility of ZnO, particles dispersed in liquid start to align within a few seconds in correlation with the magnetic field. These aligned particles were fixed by the gelation of monomer mixed in the liquid. Upon completion of gelation, the samples were dried and sintered via standard ceramic processing. The texture strength of the ceramic was almost 100 multiple of random distribution confirmed by a pole figure of 002 diffraction.

Next, the samples were sliced perpendicular to the *c*-axis (*ab*-plane) and parallel to the *c*-axis (see Fig. 1). Carrier concentration and mobility were analyzed at a temperature range of 80–400 K using a DC Hall measurement system (Resitest8300, Toyo Corporation, Tokyo, Japan). Here, the van der Pauw method was adopted. The current–voltage characteristics of these contacts showed a linear relationship. The applied magnetic field was 0.75 T during the measurement and reverse polarity measurement was carried out to cancel the voltage offset.

The microstructure of the sintered specimens was observed by transmission electron microscopy (TEM; 3000F, JEOL, Tokyo, Japan). TEM foils were prepared using the standard technique for thin ceramic foils: cutting, grinding, dimpling, and Ar-ion thinning. Energy-dispersive X-ray spectroscopy (EDS; Voyager III, NORAN Instruments Inc., Middleton, WI) was used for elemental analyses of GBs. The spot size was controlled to be <1 nm for this EDS analysis. Moreover, HAADF-STEM (JEM2100F equipped with Cs corrector, JEOL) was used to clarify the image contrast of atomic columns. EDS mapping was also carried out using JEM2100F under the conditions of the dwell time of 0.8 ms and the spot size of 0.6 nm. As to the view direction of the GB observations, refer to Fig. 1.

III. Results and Discussion

(1) *Anisotropy of Hall Mobility*

The results of Hall measurement for the *ab*-plane and *c*-axis are shown in Fig. 2. The carrier concentration in each direction

H.-J. Kleebe—contributing editor

Manuscript No. 28126. Received September 9, 2010; approved December 8, 2010.
[†]Author to whom correspondence should be addressed. e-mail: y.kinemuchi@aist.go.jp

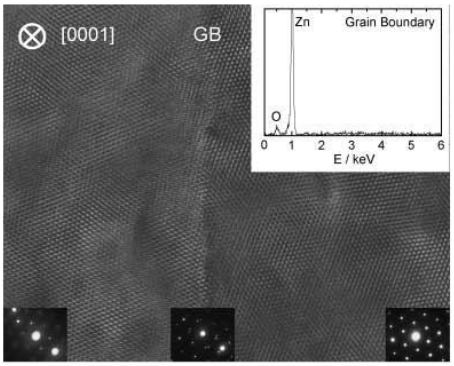

Fig. 3. Edge-on high-resolution transmission electron microscopic image of grain boundary (GB) on the *ab*-plane. Inset shows energy-dispersive X-ray spectroscopic spectrum at GB. No intergranular phase was found at the GB.

below that temperature, ionized scattering dominated the mobility confirmed by the $T^{3/2}$ dependence on nondegenerate semiconductors.[7]

The lines in Fig. 2 show the mobility based on Eq. (2). The estimated mobility shows less temperature dependence at low temperature, and decreases with temperature. As to the difference between *c*-axis and *ab*-plane, the anisotropy at low temperature is not expected so large compared with the observed mobility. Especially, deviation of the observation from the modified BHD model was unreasonably large for *c*-axis, indicating pronounced GB influence for *c*-axis which was not taken into account in the above calculation. In addition, the mobility of *c*-axis resembled with that of randomly oriented one,[5] which also implicates GB influence on the mobility.

(2) Origin of the Anisotropy

In a previous report,[4] we noted that periodic structure was often observed on the *ab*-plane. The typical structure of these grain boundaries is shown in Fig. 3. The edge on HRTEM image

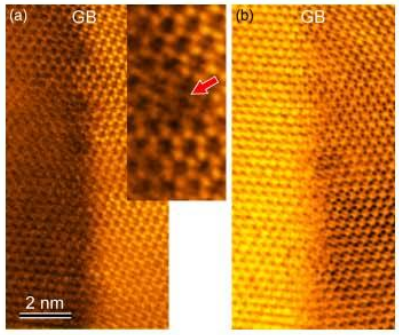

Fig. 5. Atomic-resolution scanning transition electron microscope (STEM) images of a grain boundary (GB) on the *ab*-plane. High-angle annular dark-field (HAADF)-STEM (a) and bright-field (BF)-STEM (b). The inset in (a) is a magnified HAADF-STEM image showing coincident sites at the GB. Local disorder of the atomic arrangement was also found, as denoted by the arrow.

depicts the absence of an intergranular phase[4] which was identified neither Al_2O_3 nor $ZnAl_2O_4$. It is rational that at a coherent grain boundary, the structure is energetically stable, so that a lower level of impurity segregation is tolerated compared with that in a random grain boundary.[13] In contrast, Al segregation was found to be pronounced at boundaries crossing the *c*-axis direction as shown in Fig. 4. In addition, Al was barely detected in the grain interior, suggesting that the solid solution of Al in the Zn site was less than the detection limit of 0.5 at%, which agrees reasonably well with an SIMS analysis.[14]

The detailed structure of grain boundaries on the *ab*-plane was further observed by HAADF-STEM. Figure 5 shows images at a GB on the *ab*-plane. In the HAADF-STEM image, the positions of the atomic columns are directly imaged as bright spots. In this case, the Zn-O columns are imaged as bright spots. It is surprising that the coincident sites were observed as seen in the inset in Fig. 5. It is also noted that the regular arrangement disappears near the neighbor shown by the arrow. Zn defects and/or Al atoms would exist in that area, which may be induced by the mismatch in atomic positions caused by the tilt angle of the grains.[13]

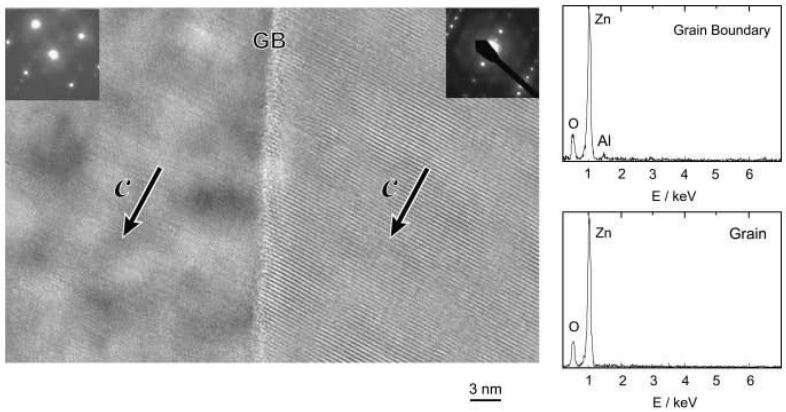

Fig. 4. Edge-on high-resolution transmission electron microscopic image of grain boundary (GB) traversing *c*-axis. Inset shows energy-dispersive X-ray spectroscopic spectrum at GB and grain interior, showing segregation of Al at GB.

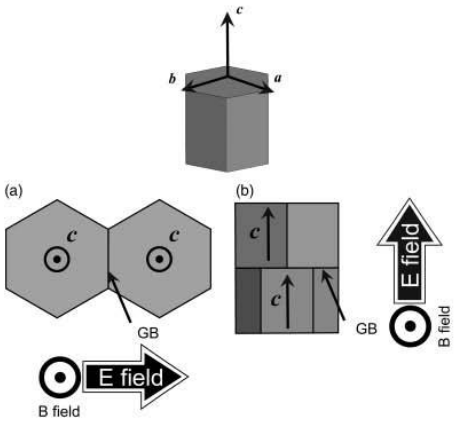

Fig. 1. Geometrical setup of mobility measurement and transmission electron microscopic (TEM) observation. ZnO crystals are schematically represented as hexagon with *a*, *b*, and *c* axes. The Hall mobility of *ab*-plane and *c*-axis was measured in the setup (a) and (b), respectively. Here, *E* and *B* fields indicate the direction of electric and magnetic fields during the measurement. Because of the *c*-axis texturing of the sample, grain boundaries (GBs) in *ab*-plane possess tilt GB (setup a) and those along *c*-axis resemble twist GB (setup b). TEM observations of each GB were performed in the direction orthogonal to the sheet.

was an identical value of 9×10^{19} cm^{-3} and independent of temperature, indicating degenerate semiconductors of the sample. The mobility of the *ab*-plane was almost double that of the *c*-axis for the entire temperature range. Below 200 K, the mobility was almost constant, which suggests scattering by ionized impurity. The influence of ionized scattering in degenerate semiconductors can be expressed by the Brooks Herring Dingle (BHD), model.[8] In addition, Minami *et al.*, [9] reported that a high carrier concentration leads to increase in density-of-states, DOS, effective mass that estimated from plasma frequency. Young *et al.*, [10] also reported the increase of DOS effective mass based on Seebeck and Nernst coefficients measurements. Their estimated DOS effective mass showed quantitative agreement. Therefore, it is reasonable to assume nonparabolic *E k* dispersion, and the BHD model can be modified as Pisarkiewics *et al.* [11] described:

$$\mu_i = \frac{3\pi^3\hbar^3(4\pi\varepsilon_0\varepsilon_r)^2}{2e^3}\frac{n}{Z^2N_i}\frac{1}{F}\frac{1}{m^{*2}} \tag{1}$$

where

$$F \quad \left[1+\frac{4x_1}{x_0}\left(1-\frac{x_1}{8}\right)\right]\ln(x_0+1)-\frac{x_0}{x_0+1}-2x_1\left(1-\frac{5}{16}x_1\right)$$

$$x_0 \quad \frac{4\pi\varepsilon_0\varepsilon_r\hbar^2(3\pi^2 n)^{1/3}}{e^2 m^*}$$

$$x_1 \quad 1-\frac{m_0^*}{m^*}$$

$$m^* \quad m_0^*\left[1+2C\frac{\hbar^2}{m_0^*}(3\pi^2 n)^{\frac{1}{3}}\right]^{\frac{1}{2}}$$

From the equations, it can be seen that the mobility is determined by the properties: relative static permittivity (ε_r), carrier concentration (n), DOS effective mass (m^*), effective mass at the bottom of conduction band (m_0^*), the charge of impurity (Z), and its concentration (N_i). The symbols π, ε_0, $\hbar$ and e have the standard meaning. When m^* is identical with m_0^* above equation reduces to BHD model. Adopting m^*/m_e of 0.31,[9] C of 1.04 eV,[9] ε_r(*c*-axis) of 8.75,[12] ε_r(*ab*-plane) of 7.8,[12] n of 9×10^{19} cm^{-3}, Z of 1, and $N_i = n$, μ_i is estimated as 119 and 102 cm^2/V·s for the *c*-axis and *ab*-plane, respectively. Here, higher μ_i is expected in the *c*-axis direction due to the higher ε_r of the *c*-axis. In addition, the anisotropy of m^* is considered to be negligible because of the isotropic Seebeck coefficient, which is a function of m^* and n, of this material.[5,10]

In order to estimate total mobility (μ) of the samples, the other scattering mechanisms must be included. To do that, we applied Matthiessen's rule

$$\frac{1}{\mu} = \frac{1}{\mu_{other}} + \frac{1}{\mu_i} \tag{2}$$

Here, μ_{other} means the mobility scattered by other mechanisms such as scattering by acoustic phonons. For the value of μ_{other}, we referred to the data on a single crystal with low doping concentration.[7] For the mobility of single crystal, it was analyzed that polar optical scattering, deformation potential scattering and piezoelectric scattering were responsible above 50 K;

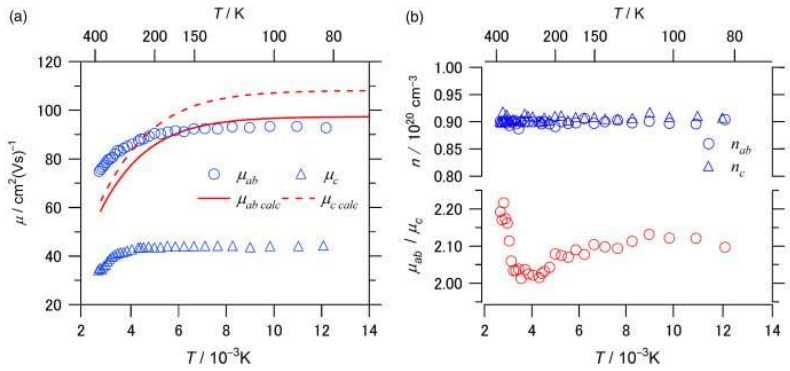

Fig. 2. Hall measurement of *c*-axis textured ZnO. (a) Temperature (T) dependence of mobility (μ) along the *c*-axis and on the *ab*-plane. (b) Carrier concentration (n) and anisotropy of mobility (μ_{ab}/μ_c). Lines in (a) indicate a semitheoretical prediction based on the modified Brooks–Herring–Dingle model and Matthiessen's rule.

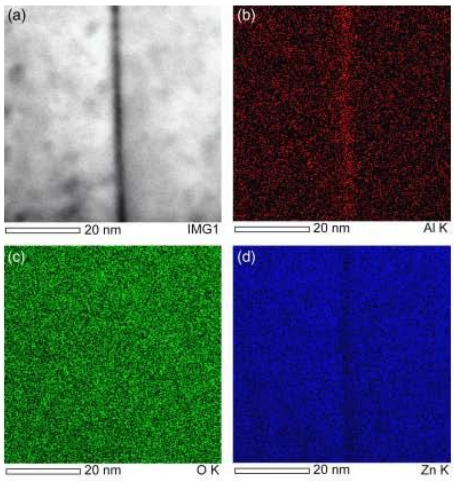

Fig. 6. Energy-dispersive X-ray spectroscopic mapping images of a grain boundary (GB) along the *c*-axis direction. Bright-field image (a), and mapping images of Al (b), oxygen (c), and Zn (d). Al segregation and Zn deficiency are pronounced at the GB.

The above observations clarified that the structural disorder at the GB across the *c*-axis direction causes the segregation of Al, while such segregation seldom occurs on the *ab*-plane. In order to clarify the chemical homogeneity in further detail, we performed EDS mapping along the grain boundaries. Figure 6 shows images of the GB along the *c*-axis direction. In the Al mapping image, a clear contrast at the GB is observed, indicating dopant segregation along the GB. In contrast, the mapping image for O shows a homogeneous distribution over the entire area. As for Zn, a dark contrast along the GB was observed,

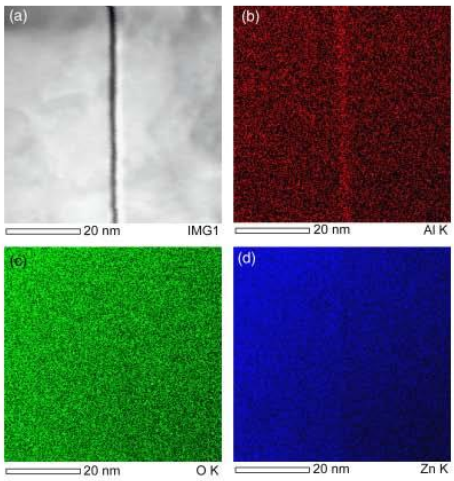

Fig. 7. Energy-dispersive X-ray spectroscopic mapping images of a grain boundary (GB) along the *ab*-plane. Bright-field image (a), and mapping images of Al (b), oxygen (c), and Zn (d). The tilt angle of the grains in this GB is larger than that of the GB shown in Figs. 3 and 5. Slight Al segregation is observed, while Zn deficiency is not significant.

showing a deficiency in Zn near the boundary. This Zn deficiency and the Al enrichment can be explained by the charge neutrality, which is expressed as $2[V''_{Zn}] - [Al^{\bullet}_{Zn}]$ or $[V'_{Zn}] - [Al^{\bullet}_{Zn}]$. So far, evidence of a Zn vacancy as the dominant acceptor in *n*-type ZnO has been confirmed by positron annihilation spectroscopy.[15]

EDS mapping was also carried out at the GB on the *ab*-plane. The mapping image at the GB with the direct bonding of atoms showed no contrast for Al, Zn, and O, indicating segregation below the detection limit. In addition, a GB with a relatively high tilt angle between adjacent grains showed a weak Al contrast, as seen in Fig. 7, even in the *ab*-plane direction. However, the Zn contrast at the GB was not significant.

Based on the aforementioned microstructural observations, GB structures and resultant dopant segregation along with defect formation are considered as possible causes for the anisotropy of mobility. In addition to the GB characters, the other geometrical factors such as the number as well as the width of GB may also influence to the anisotropy.

As with the *ab*-plane direction, our textured ceramics showed elongation of grain size.[5] Hence the number of GB was lower in the *ab*-plane, which agrees the trend of anisotropy. Besides, randomly oriented ceramics having similar grain size with that of the *ab*-plane stayed at half of the mobility of the *ab*-plane,[5] showing the GB density does not solely explain the high mobility along the *ab*-plane. Furthermore, the mobility along the *ab*-plane is mostly identical to that of a heavily doped single crystal as estimated in the previous section, which implies the electrons are mainly scattered by ionized impurity, in other words ionized dopant in the grain, and the scattering at GB is thus considered as minor effect. The atomically ordered GB along the *ab*-plane, Fig. 5, supports this argument.

In contrast to the *ab*-plane, the scattering at GB along the *c*-axis is thought to be significant. Accumulated defects as observed by STEM, segregated GB layer shown in Fig. 3, and potential barrier near GB are the possible causes for the lowering in mobility along the *c*-axis. Among them, the influence of scattering by potential barrier is considered to be limited, although the Arrhenius plot of conductivity above the room temperature suggests formation of the potential barrier along the *c*-axis.[16] This is clear from the mobility <200 K. In the temperature region, the temperature-independent lower mobility was observed in this direction, indicating that nonthermally activated scattering is responsible for the low mobility. Hence, we can discard the scattering via potential barrier. However, to distinguish other factors is not straightforward. The correlation between accumulation of defects and formation of GB layer makes it difficult further.

Generally speaking, the GB observed along the *c*-axis resembles to that of randomly oriented ceramics showing dopant segregation similarly. Considering the situation in the randomly oriented ceramics as well, plausible mechanism for the low mobility is summarized as follows. As we demonstrated by EDS mapping images, the dopant segregation occurs profoundly at the GB with low-coherency, possibly to reduce GB energy. Along with the segregation, Zn vacancy also accumulates near the vicinity to ensure the charge neutrality. Hence concentration of defects, i.e., dopant and zinc vacancy, near GB tends to be higher compared with that of grain interior. Such accumulated defects sure to shorten the mean free path of electron, resulting in low mobility. Other geometrical influence modifies mobility in some extent. Consequently, the difference in defect concentrations resulting from the crystallographic orientation of grains at GBs causes the anisotropy.

III. Conclusions

Zinc oxide essentially possesses high electron mobility, and shows anisotropy at low temperature, which was reported for a single crystal with low carrier concentration.[7] In degenerate semiconductors, however, the high mobility and anisotropy

should be reduced by ionized scattering as a result of doping, which we predicted based upon modified BHD model. Unexpectedly, significant anisotropy was experimentally observed in *c*-axis textured ceramic. Detailed observations of the grain boundaries were performed by means of HRTEM, HAADF-STEM, and EDS mapping, and the following conclusions were reached.

(1) On the *ab*-plane, tilt GB with periodic structure was frequently confirmed. Furthermore, coincident sites were directly observed by means of HAADF-STEM. On the contrary, there was no such specific arrangement at GB crossing the *c*-axis direction.

(2) An aluminum layer was observed at the GB along *c*-axis. On the other hand, such segregation was seldom found at GB on the *ab*-plane.

(3) EDS mapping revealed that Al segregation led to a deficiency in Zn.

These findings clarified that the anisotropy of *c*-axis textured ZnO originates in the GB structure. That is, there is a disordered GB itself as well as dopant segregation along with vacancy formation in the vicinity, resulting in low mobility along the *c*-axis in Al-doped ZnO. This structure resembles the GB of randomly oriented ZnO, which causes the low mobility.

Acknowledgments

We thank Dr. E. Okunishi of JEOL for his support in the HAADF-STEM observations. We also thank Dr. H. Hashimoto of AIST for his experimental help in the Hall measurement.

References

[1]M. Ohtaki, T. Tsubota, K. Eguchi, and H. Arai, "High-Temperature Thermoelectric Properties of $(Zn_{1-x}Al_x)O$," *J. Appl. Phys.*, **79** [3] 1816–8 (1996).

[2]T. Tsubota, M. Ohtaki, K. Eguchi, and H. Arai, "Thermoelectric Properties of Al-Doped ZnO as a Promising Oxide Material for High-Temperature Thermoelectric Conversion," *J. Matter Chem.*, 7 [1] 85–90 (1997).

[3]B. A. Cook, J. A. Harringa, and C. B. Vining, "Electrical Properties of Ga and ZnS Doped ZnO Prepared by Mechanical Alloying," *J. Appl. Phys.*, **83** [11] 5858–61 (1998).

[4]H. Kaga, Y. Kinemuchi, H. Yilmaz, K. Watari, H. Nakano, H. Nakano, S. Tanaka, A. Makiya, Z. Kato, and K. Uematsu, "Orientation Dependence of Transport Property and Microstructural Characterization of Al-Doped ZnO Ceramics," *Acta Mater.*, **55** [14] 4753–7 (2007).

[5]H. Kaga, Y. Kinemuchi, S. Tanaka, A. Makiya, Z. Kato, K. Uematsu, and K. Watari, "Preparation and Thermoelectric Property of Highly Oriented Al-Doped ZnO Ceramics by a High Magnetic Field," *Jpn. J. Appl. Phys.*, **45**, L1212–4 (2006).

[6]H. Kaga, Y. Kinemuchi, S. Tanaka, A. Makiya, Z. Kato, K. Uematsu, and K. Watari, "Fabrication of C-Axis Oriented $Zn_{0.98}Al_{0.02}O$ by a High-Magnetic-Field Via Gelcasting and its Thermoelectric Properties," *J. Ceram. Soc. Jpn.*, **114** [1335] 1085–8 (2006).

[7]P. Wagner and R. Helbig, "Halleffekt und anisotropie der beweglichkeit der elektronen in ZnO," *J. Phys. Chem. Solids*, **35** [3] 327–35 (1974).

[8]R. B. Dingle, "Scattering of Electrons and Holes by Charged Donors and Acceptors in Semiconductors," *Philos. Mag.*, **46** [379] 831–40 (1955).

[9]T. Minami, H. Sato, K. Ohashi, T. Tomofuji, and S. Tanaka, "Conduction Mechanism of Highly Conductive and Transparent Zinc-Oxide Thin-Films Prepared by Magnetron Sputtering," *J. Cryst. Growth*, **117** [1–4] 370–4 (1992).

[10]D. L. Young, T. J. Coutts, V. I. Kaydanov, A. S. Gilmore, and W. P. Mulligan, "Direct Measurement of Density-of-States Effective Mass and Scattering Parameter in Transparent Conducting Oxides using Second-Order Transport Phenomena," *J. Vac. Sci. Technol. A*, **18** [6] 2978–85 (2000).

[11]T. Pisarkiewicz, K. Zakrzewska, and E. Leja, "Scattering of Charge-Carriers in Transparent and Conductive Thin Oxide-Films with a Non-Parabolic Conduction-Band," *Thin Solid Films*, **174**, 217–23 (1989).

[12]K. Ellmer, "Resistivity of Polycrystalline Zinc Oxide Films: Current Status and Physical Limit," *J. Phys. D: Appl. Phys.*, **34** [21] 3097–108 (2001).

[13]Y. Sato, T. Yamamoto, and Y. Ikuhara, "Atomic Structures and Electrical Properties of ZnO Grain Boundaries," *J. Am. Ceram. Soc.*, **90** [2] 337–57 (2007).

[14]K. Shirouzu, T. Ohkusa, M. Hotta, N. Enomoto, and J. Hojo, "Distribution and Solubility Limit of Al in Al_2O_3-Doped ZnO Sintered Body," *J. Ceram. Soc. Jpn.*, **115** [1340] 254–8 (2007).

[15]F. Tuomisto, V. Ranki, and K. Saarinen, "Evidence of the Zn Vacancy Acting as the Dominant Acceptor in *n*-Type ZnO," *Phys. Rev. Lett.*, **91** [20] 205502 (2003).

[16]Y. Kinemuchi, H. Kaga, S. Tanaka, K. Uematsu, H. Nakano, and K. Watari, "Influence of Grain-Boundary on Textured Al-ZnO," *Ceram. Eng. Sci. Proc.*, **29** [10] 63–8 (2009). □

JTTEE5 20:407–411
DOI: 10.1007/s11666-010-9522-z
1059-9630/$19.00 © ASM International

Microstructure of Interfacial Region Between Cold-Sprayed Copper Coating and AlN Substrate Coated with Sputtered Titanium and Copper

Hiromi Nakano, Motohiro Yamada, Masahiro Fukumoto, and Eiji Yamaguchi

(Submitted February 17, 2010; in revised form May 24, 2010)

Cold spraying has been developed as a high-quality coating technique. In this article, copper is deposited on an AlN substrate coated by the sputtering of titanium and copper at a low pressure of less than 1.0 MPa, making this approach suitable for a wide range of engineering applications. In order to understand the adhesion mechanism at the atomic scale, the interfacial regions are carefully observed in thin foil samples from the cross sections of the specimens with a HREM. We find a unique wavy boundary between the sputtered titanium and the sputtered copper. It is assumed that the shear-instability phenomenon occurs due to the cold-spraying process and influences the adhesive strength. Furthermore, the cold-sprayed copper particles are connected directly without any oxidation layer due to the appearance of new metallic surfaces during the impact process. The TEM data clearly reveal the phenomena and mechanisms related to the impact of powder sprayed on the substrate.

Keywords cold gas dynamic spraying, coating-substrate interaction, porosity of coatings

1. Introduction

Since the early 1990s, cold spraying has been developed as a high-quality metallic coating technique (Ref 1, 2). In this technique, a metallic coating is formed by solid metallic particles that have a lower-temperature melting point than that of metallic powder as well as high velocity with less oxidization. In other words, the metallic powder is accelerated by injection into a high-velocity gas stream at low temperature and deposited onto a substrate as solid powder. The high-velocity gas stream is generated through a converging-diverging nozzle. Mechanically, softer metallic materials can be effectively coated by this process, and the resulting coating has superior properties when compared with conventional thermal-sprayed coatings. Copper is particularly suitable for spraying due to its high electrical and thermal properties (Ref 3). Fabrication of thick copper coatings without oxidation is expected through a cold-spray process.

Hiromi Nakano, Cooperative Research Facility Center, Toyohashi University of Technology, Tempaku, Toyohashi 441-8580, Japan; **Motohiro Yamada** and **Masahiro Fukumoto**, Department of Production Systems Engineering, Toyohashi University of Technology, Tempaku, Toyohashi 441-8580, Japan; and **Eiji Yamaguchi**, Sinto-brator, Ltd., Honohara, Toyokawa 442-8505, Japan. Contact e-mail: hiromi@crfc.tut.ac.jp.

Recently, low-pressure cold spraying at a pressure less than 1.0 MPa has been studied, and thus the range of applications for cold spraying has become wider (Ref 4, 5). Bonding strengths for particle-to-particle and particle-to-substrate contact are required in such application fields. In order to improve the adhesive strength between the coating material and the substrate, it is necessary to obtain microstructural data at the interfacial boundaries related to the adhesive mechanism. However, it is not easy to make a thin specimen at the region of interest with a transmission electron microscope (TEM). Only a few papers have reported microstructure findings by TEM in cold spraying (Ref 6-8).

In this study, copper was deposited by cold spraying on an AlN substrate at a low pressure of less than 1.0 MPa. On the surface of the AlN substrate, thin films of titanium and copper were sputtered because this produces a higher bonding strength than that obtained by coating directly on the AlN substrate (Ref 9). Thin specimens for TEM observation at the atomic scale were carefully prepared with an ion-slicer device using an Ar ion. Microstructural observations of the interfacial regions were made using a high-resolution TEM (HREM), and these observations clarified the impact phenomenon of high-velocity solid metallic particles.

2. Experimental Procedure

Cold-spray equipment installations were custom-designed and custom-made. Air is used as a process gas. The process gas pressure and temperature were 0.7 MPa and 623 K, respectively. The powder material used was

commercially available pure copper with a spherical shape and an average size of 5 μm. The substrate is sintered AlN plate with titanium and copper film. Those films were deposited by sputtering (CFS-4ES-231, Shibaura Mechatronics Corporation, Kanagawa, Japan). The titanium layer was deposited onto the AlN surface initially at 100 nm thickness, and then the copper layer was deposited onto the titanium layer at a thickness of 100 nm.

A stud pull adherence test was carried out using 5 mm × 5 mm stud to measure the adhesion strength of coating and substrate interface.

A TEM foil of the cross section of a deposited specimen was prepared by an ion slicer (EM-09100IS, JEOL, Tokyo, Japan) using Ar-gas. The thin specimen was finally etched by an accelerating voltage of 1.0 kV to reduce specimen damage and stress. A HREM image was observed with a TEM (JEM-3000F, JEOL, Tokyo, Japan) operating at 300 kV with spherical aberration of Cs = 1.0 nm (0.19 nm theoretical resolution, −53.3 nm Sherzer focus).

3. Results and Discussion

In the cold-spraying process, it is known that the evolution of interfacial microstructure has an influence on particle adhesion. In order to understand the adhesion mechanism at the atomic scale, an advanced TEM technique is needed to prepare a thin cross-sectional foil. In this experiment, we could make a thin foil by using an ion-slicer device, and thus we obtained many new microstructural data on the interfacial regions.

Figure 1 shows cross-section microstructures of an AlN substrate coated by sputtering Ti and Cu thin films in (a) and cold-spraying the copper coating on the Cu/Ti/AlN substrate in (b). The thin films of Ti and Cu were coated at about a 100 nm thickness by sputtering on the AlN surface. A glass cover was used to protect the thin films during preparation of the TEM foil. After depositing cold-sprayed copper (CS Cu) coating, the interfacial microstructure of these thin sputtered layers was clearly changed, as shown in Fig. 1(b). Compared to the initial flat structure shown in Fig. 1(a), a unique wavy structure at the boundary between sputtered Ti and Cu thin layers was identified after the cold spraying. A similar wavy structure is seen in the joint boundary formed by explosive welding. This phenomenon usually occurs at the boundary between different materials with different flow velocities, i.e., the so-called shear-instability phenomenon (Ref 6, 8, 11). In this case, the relative difference in velocities between sputtered Cu (SP Cu) and sputtered Ti (SP Ti) may cause shear instability because the shearing deformation of SP Cu connected to CS Cu is different from that of SP Ti connected to AlN, as shown by the schematic illustration in Fig. 2. Moreover, interfacial regions were observed, as indicated by the rectangles in Fig. 1(b). Figure 3 shows a TEM image of boundary 1 between CS Cu and SP Cu. The SP Cu film is composed of small grains. The cold-sprayed copper coating layer consists of larger grains, which include many dark contrasts due to strain. The boundary is wavy due to the impact process, and direct contact between metallic CS Cu and SP Cu was observed without any oxidized layer. The impact, with high-velocity particle

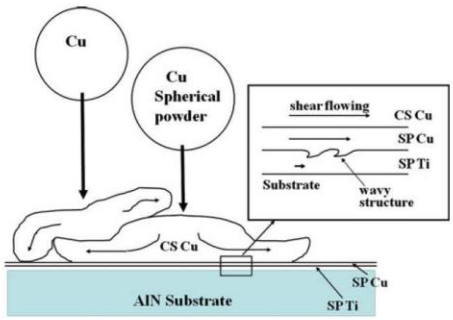

Fig. 2 Schematic illustration of shear-instability phenomenon during cold spraying

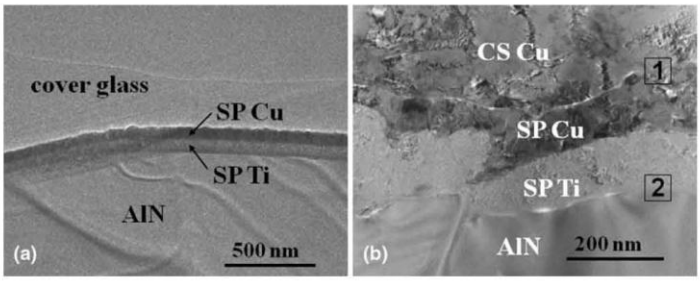

Fig. 1 TEM images of (a) AlN substrate coated by sputtered Cu and Ti films and (b) cold-sprayed Cu on Cu/Ti/AlN substrate

collision, influences the joint process by causing high cohesion intensity at the joint boundary. On the other hand, thin oxidation film of about 2 nm thickness was observed at boundary 2 between SP Ti and the AlN substrate, as shown in Fig. 4. This may be attributed to the fact that the surface of AlN ceramics usually contains a thin layer of Al_2O_3. The titanium was sputtered on the oxidation surface of the AlN substrate with a non-impact process, and therefore the oxidation film remained on the boundary. The bonding of SP Ti and AlN is strong because they are connected through oxidation film. These findings reveal that the wavy structure was formed at the boundary between the sputtered Cu and the Ti layer by the shear-instability phenomenon due to the cold-spraying process and that it influences the adhesive strength.

Figure 5 shows the TEM images of the CS Cu layer in (a) and the grain boundary of copper-copper particles

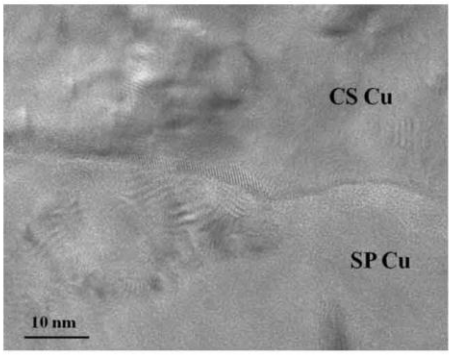

Fig. 3 TEM images of boundary between cold-sprayed (CS) Cu and sputtered (SP) Cu

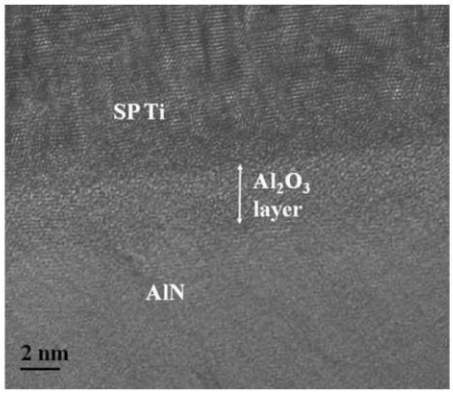

Fig. 4 TEM image of boundary between sputtered (SP) Ti and AlN substrate

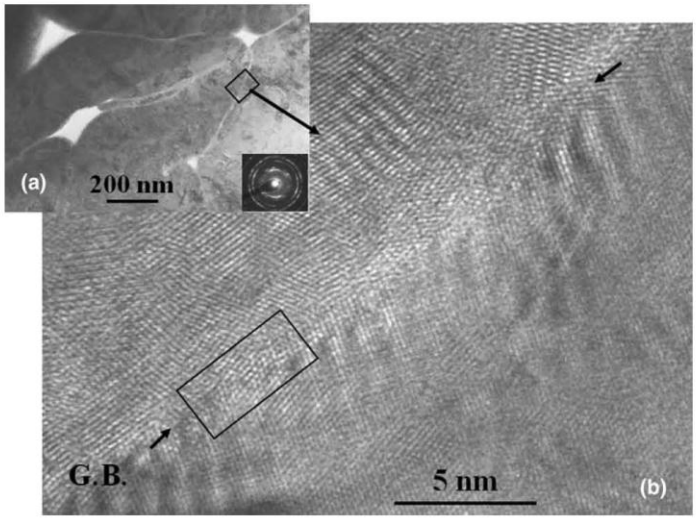

Fig. 5 TEM images of (a) CS Cu coating layer and (b) boundary between cold-sprayed copper particles

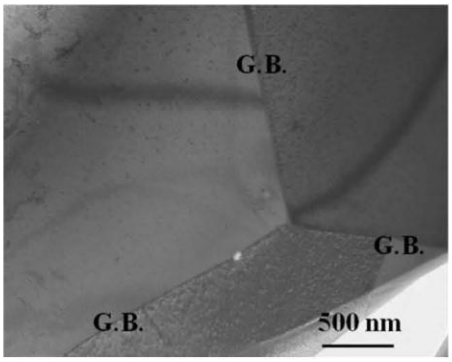

Fig. 6 TEM image of CS coating layer annealed at 973 K

in (b). In the CS Cu coating layer, copper particles are composed of polycrystal grains, as shown in the selected area diffraction pattern in Fig. 5(a). These copper particles are distorted and deformed with long and slender shapes, and thus many strains were observed in the lattices. On the two-grain boundary, a coherency boundary was observed with no oxidation film, as indicated by the rectangle in (b). In general, it is easy to oxidize the surface of metallic copper in air. The oxygen concentrations in the copper particles and coatings were not measured so that the oxygen concentration change due to cold splaying cannot be determined at this experimental stage. Actually, the oxidation film as an amorphous phase was observed at the boundary between the AlN substrate and the sputtered titanium. This finding reveals an impact phenomenon of the high-velocity solid metallic particles. We think that a new surface appears partially on the copper particles in the plastic deformation by the cold-spraying process (Ref 10), and the bonding boundary attains coherence. However, there are many spaces of 50-300 nm in size between the copper particles in the CS Cu coating layer, and it was shown that these weaken the cohesive strength between particles. This problem can be solved by annealing the coating material at 973 K. Figure 6 shows the CS Cu coating layer annealed at 973 K for 1 h in a vacuum. The grain boundaries are straight and adhere to each other. The strain in the copper grain decreased and few pores were observed at the grain boundaries. As a result, the spaces drastically decreased during grain growth. In the pre-experimental stage, the influences of feedstock powder, working gas pressure, and deposition temperature have been investigated to improve the adhesive strength (Ref 12). However, it has not been easy to improve adhesive strength by changing these conditions. Finally, the adhesive strength of this copper coating could be increased by annealing, and it finally achieved a level somewhat over 10 MPa, which is suitable for practical applications.

4. Conclusions

In this investigation, copper was deposited by cold spraying at a low pressure of less than 1.0 MPa on an AlN substrate, which was coated by sputtered titanium and copper. Microstructural characterization of the cold-sprayed copper coating is important for improving the adhesive strength at the joint boundary. The interfacial microstructures could be clearly observed at the particle-to-particle and particle-to-substrate boundaries with a high-resolution TEM. Consequently, the following conclusions were drawn:

1. A wavy boundary was observed between the sputtered titanium and the sputtered copper. We believe that this phenomenon occurs due to shear instability, even with low-pressure cold spraying, and thus improves adhesive strength.
2. A TEM image revealed oxidation film with about 2 nm thickness at the boundary between the sputtered titanium and the AlN substrate. Such oxidation film usually appears on the surface of an AlN substrate, and it permitted a strong bonding of the titanium layer.
3. On the other hand, no oxidation film was observed at the cold-sprayed particle-to-particle boundaries. The cold-sprayed copper particles were deformed by the collision, and many strains were observed in the crystal lattices. The results indicate that a new surface appears partially on the copper particles in the plastic deformation by a cold-spraying process.

References

1. A.P. Alkhimov, V.F. Kosarev, and A.N. Papyrin, A Method of Cold Gas-Dynamic Deposition, *Sov. Phys. Dokl.*, 1990, **35**, p 1047-1049
2. A.P. Alkhimov, V.F. Kosarev, N.I. Nesterovich, and A.N. Papyrin, Method of Applying Coating, Russian Patent No. 1618778, 8 Sept (1990)
3. J. Haynes, J. Karthikeyan C. Moreau, and B. Marple, Cold Spay Copper Application for Upper Stage Rocket Engine, *International Thermal Spray Conference*, May 5-8, 2003 (Orland), ASM International, Materials Park, OH, USA, 2003, p 79-83
4. H.Y. Lee, S.H. Jung, S.Y. Lee, Y.H. You, and K.H. Ko, Correlation Between Al_2O_3 Particles and Interface of Al-Al_2O_3 Coating by Cold Spray, *Appl. Surf. Sci.*, 2005, **51**, p 1891-1898
5. K. Ogawa, K. Ito, K. Ichimura, Y. Ichikawa, S. Ohno, and N. Onda, Characterization of Low-Pressure Cold-Sprayed Aluminum Coatings, *J. Therm. Spray Technol.*, 2008, **17**(5-6), p 728-735
6. K.H. Kim, M. Watanabe, J. Kawakita, and S. Kuroda, Grain Refinement in a Single Titanium Powder Impacted at High Velocity, *Script Mater.*, 2008, **59**, p 768-771
7. C. Bprchers, F. Gärtner, T. Stoltenhoff, and H. Kreye, Formation of Persistent Dislocation Loops by Ultra-High Strain-Rate Deformation During Cold Spraying, *Acta Mater.*, 2005, **53**, p 2991-3000
8. C.-J. Li, W.-Y. Li, and Y.-Y. Wang, Formation of Metastable Phases in Cold-Sprayed Soft Metallic Deposit, *Surf. Coat. Technol.*, 2005, **198**, p 469-473

9. S. Zhu and W. Wlosinski, Joining of AlN Ceramic to Metals Using Sputtered Al or Ti Film, *J. Mater. Process. Technol.*, 2001, **109**, p 277-282
10. R.C. Dykhuizen, M.F. Smith, D.L. Gilmore, R.A. Neiser, X. Jian, and S. Sampath, Impact of High Velocity Cold Spray Particles, *J. Therm. Spray Technol.*, 1999, **8**(4), p 559-564
11. T. Scmidt, F. Gärtner, H. Assdi, and H. Kreye, Development of a Generalized Parameter Window for Cold Spray Deposition, *Acta Mater.*, 2006, **54**, p 729-742
12. M. Fukumoto, H. Terada, K. Sato, M. Mashiko, M. Yamada, and E. Yamaguchi, Improvement in Deposition Efficiency of Copper Particles onto Metallic Substrate in Cold Spray Process, *Proceedings of International Thermal Spray Conference*, 2008 (Maastricht, CD)

JOURNAL OF APPLIED PHYSICS **108**, 053721 (2010)

Enhanced boundary-scattering of electrons and phonons in nanograined zinc oxide

Yoshiaki Kinemuchi,[1,a)] Hiromi Nakano,[2] Masashi Mikami,[1] Keizo Kobayashi,[1] Koji Watari,[1] and Yuji Hotta[1]
[1]*National Institute of Advanced Industrial Science and Technology (AIST), 2266-98 Anagahora, Shimoshidami, Moriyama, Nagoya 463-8560, Japan*
[2]*Toyohashi University of Technology, 1-1 Hibariga-oka, Tempaku, Toyohashi 441-8580, Japan*

(Received 2 April 2010; accepted 8 July 2010; published online 15 September 2010)

Nanoscale constituents in bulk materials can promote enhanced boundary-scattering in the transport of phonons as well as electrons, which is considered a key design factor for enhancing thermoelectric properties. Here, we demonstrate a method for synthesizing zinc oxide bulk materials from nanoparticles without significant grain growth by means of pressure-induced deformation at 200 °C. This allows us to comprehensively analyze the grain size dependence of thermoelectric properties in the nanoscale range above 30 nm, the size of a nanoparticle. Grain size was found to largely influence thermal conductivity as well as electrical conductivity. The observed thermal conductivity agreed with the Callaway model, indicating that enhanced phonon boundary-scattering was responsible for the variation. On the contrary, Seebeck coefficient was mostly governed by effective mass and carrier concentration, and was independent of the grain size. The dimensionless figure of merit systematically increased with grain size, which challenged the effect of nanograin on this system. © *2010 American Institute of Physics*. [doi:10.1063/1.3475650]

I. INTRODUCTION

Based on the design concepts for thermoelectric materials,[1] low dimensionality is the key to surpassing the properties of conventional materials. In thermoelectric applications, low thermal conductivity and high Seebeck coefficient along with high electrical conductivity are required for enhanced energy conversion efficiency. The two dominant concepts in low dimensionality for improving the thermoelectric properties are (a) quantum confinement by the introduction of nanoscale constituents and (b) enhanced phonon scattering by the interfacial surfaces in nanostructures. The former contributes to a high Seebeck coefficient with a certain carrier concentration while the latter reduces the thermal conductivity. These concepts are demonstrated in the two-dimensional quantum wells of $PbTe/Pb_{1-x}Eu_xTe$,[2] Si/Ge,[3] Bi_2Sb_3/Sb_2Te_3,[4] PbSeTe/PbTe,[5] $SrTiO_3/SrTi_{0.8}Nb_{0.2}O_3$,[6] nanowires of Si,[7,8] etc. Due to the technological importance of an energy-harvesting device that converts waste heat from fossil-fuel combustion into useful electric energy, the enhancement of thermoelectric properties by applying such concepts for practical bulk materials is highly demanded.

Sintering of nanoparticles offers a promising route to the synthesis of bulk samples with nanoscale constituents. Successful results of the sintering route have been reported for alloys such as $Si_{0.8}Ge_{0.2}$ (Ref. 1) and BiSbTe.[9] In the nanostructured bulk materials that have been tested, reduction in thermal conductivity has proven to be a primary effect of the enhancement in thermoelectric properties. It is noted that nanoparticles of 5–10 nm are retained in the bulk materials,[1,9] suggesting enhanced phonon scattering by such nanoscale constituents.

Oxide thermoelectric materials are promising candidates for operation in high temperature conditions. Nontoxic components and abundant natural resources in place of heavy-metal alloys are additional advantages of their practical applications. Moreover, their distinctive carrier-transport[10–12] properties and variety of nanoforms[13–15] offer a new strategy for nanostructuring as seen in the nanoblock integration concept.[16] Although oxides possess the above-mentioned desirable characteristics, their thermal conductivity tends to be higher than that of heavy-metal alloys, which stems from higher phonon frequency due to ionic bonding and lighter atomic mass. This is the primary motivation for introducing nanoscale constituents into oxide bulk materials.

In practical terms, the diffusion coefficient of oxides is lower than that of metals, resulting in smaller grain size in conventional bulk materials. In addition, nanoparticles of various oxides are already commercialized. Thus, the synthesis of nanostructures in oxides is regarded as a rational process. In fact, a grain size of 60 nm in Y_2O_3 has been achieved via a well-controlled firing schedule that suppresses grain growth during the final-stage sintering, although the grain size is 4–6 times larger than the starting nanoparticles.[17] On the contrary, the size of nanoparticles is almost retained in a bulk of metallic alloys[1,9] as mentioned earlier, which is chiefly due to densification via plastic flow induced by external pressure at a relatively low temperature where grain growth is inactive. Since oxides have limited slip planes and high yield stress, it was earlier believed that a high temperature was required to achieve densification by this mechanism that causes inevitable grain growth during bulk synthesis. However, several nanoparticles show evidence of diffusion at low temperatures such as 200–300 °C.[18] If adequate pressure is applied at this tem-

a)Electronic mail: y.kinemuchi@aist.go.jp.

perature range, diffusion creep could be induced, which might lead to densification via plastic flow and the resulting nanostructuring.

Here, we demonstrate the possibility of bulk synthesis of nanostructured ZnO by means of plastic flow induced by external pressure at low temperature and report how such enormous number of grain boundary influence the transport properties.

II. EXPERIMENTAL METHODS

Commercially available Ga-doped ZnO (Pazet GK40, Hakusui Tech. Co., Ltd.), x-ray diffraction (XRD) crystalline size of 24 nm and specific surface area of 44 m^2/g, was used as the starting raw material. The doping amount of nanoparticles was confirmed as 0.26 at. % by inductively coupled plasma spectrometry. We examined the carrier concentration independently for various doping amounts in this system[19] and the present doping amount accounted for the carrier concentration of 6×10^{19} cm^{-3}. Sintering was carried out by pulsed electric current sintering (SPS-511S, SPS Syntex Inc.) under vacuum ($<10^{-1}$ Pa) atmosphere. A heating rate of 50 K/min, holding time of 5 min and furnace cooling were adopted. Maximum uniaxial pressure was applied during the temperature holding. The pressure of 500 MPa was achieved by using a mold of tungsten carbide. The samples were subsequently annealed in vacuum of ~1 Pa for 1 h at 500 °C to release residual stress. Before the annealing, the Seebeck coefficient was higher than presently reported and electrical conductivity was quite low. In addition, their temperature dependence showed complex traits.[20]

Shrinkage behavior was evaluated by thermomechanical analysis (TMA; TD5200SA, Bruker AXS K.K.). Grain size was evaluated from full width at half maximum (FWHM) of XRD peaks, and for grains exceeding 100 nm, field emission scanning electron microscopy (S-4300, Hitachi) observation was carried out for fractured surfaces. The microstructure was observed by transmission electron microscopy (TEM; 3000F, JEOL). TEM foils were prepared using the standard technique for thin ceramic foils: cutting, grinding, dimpling, and Ar-ion thinning. Energy-dispersive x-ray spectroscopy (EDS; Voyager III, NORAN Instruments Inc.) was used for elemental analyses of the grain boundaries. Thermal diffusivity was measured by the laser flash method (TC7000, ULVAC-Riko Inc.) and specific heat was evaluated by differential scanning calorimetry (SSC5200, Seiko Instruments Inc.). Density was measured by the Archimedes method. Seebeck coefficient and resistivity were measured by the static dc method and the four-probe method respectively (ZEM-1, ULVAC-Riko Inc.).

III. RESULTS AND DISCUSSION

A. Synthesis of nanograined ZnO

Prior to the bulk synthesis, we first observed the temperature of active diffusion, i.e., sintering, by TMA. Ga-doped ZnO nanoparticles (27 nm in diameter) were dry-pressed and shrinkage was monitored. The results showed two distinctive peaks in the rate, as shown in Fig. 1(a). The highest peak, at ~800 °C, was responsible for the densification of the nanoparticles in conventional sintering. This peak is strongly related to the diffusion mechanism as well as to the evolution of microstructuring.[17] More importantly, the high rate of the peak indicates active diffusion among the nanoparticles, causing particle growth and eventual collapse of the nanostructure. Therefore, the onset temperature of this highest peak is the practical limit for the synthesis of nanostructured bulk, and we applied external pressure below this temperature. The progress of densification as a function of external pressure is shown in Fig. 1(b), which indicates monotonous increase in relative density with pressure. If we assume densification via plastic flow, the criterion for densification is expressed as

$$P \geq \frac{3\sigma_y}{4\pi r^2} aN \frac{\rho}{\rho_{th}},$$

where, P is external pressure, σ_y is yield stress, r is radius of nanoparticle, a is area of one particle contact, N is average number of contact neighbors per particle, and ρ/ρ_{th} is relative density.[21] Densification via plastic flow proceeds until the left term is equivalent to the right term. If it is assumed that the volume overlapping at the particle contact is deposited evenly across the noncontacting surface of each particle, then aN can be correlated with the relative density as follows:[21]

$$aN = r^2 \frac{\rho - \rho_o}{\rho}\left[160\frac{(\rho - \rho_o)}{\rho_{th}} + 16\right],$$

where, ρ_o/ρ_{th} is the relative density at the start of pressing (0.5 for the present study). From the equations, the density and the pressure can be expressed as a function of σ_y. The solid line in Fig. 1(b) is the fitted line based on the equations, in which σ_y of 73 MPa was optimized. However, this optimized value appears to be lower than the yield stress of the basal slip plane at this temperature range,[22] suggesting that the electric current sintering employed in the present process induced local heating at the particle contact. Nevertheless, its crystalline size was mostly identical to the size of the starting nanoparticles after the sintering process, as shown in Fig. 1(c). Further increase in process temperature resulted in grain growth without significant densification. In terms of nanostructure stability at high temperature, we annealed the bulk samples and confirmed that grain growth was suppressed up to 600 °C, which was identical to the onset temperature of rapid densification observed by TMA [Fig. 1(d)].

Figure 2 shows images obtained by TEM. As can be seen in Figs. 2(a) and 2(b), the crystalline size was retained through the bulk synthesis, which corresponds to the results of XRD. It is obvious that the starting nanoparticles were well-crystallized and their surface was not covered with amorphous phase; therefore, densification at the low temperature originated in the intrinsic deformation behavior of ZnO. In addition, segregation such as that of the dopant at the grain boundary may also have influenced the sintering behavior; so we examined this through EDS at both the grain interior and the grain boundaries. The results showed that there was no significant difference between the analyzed regions, indicating a chemically homogeneous sample within

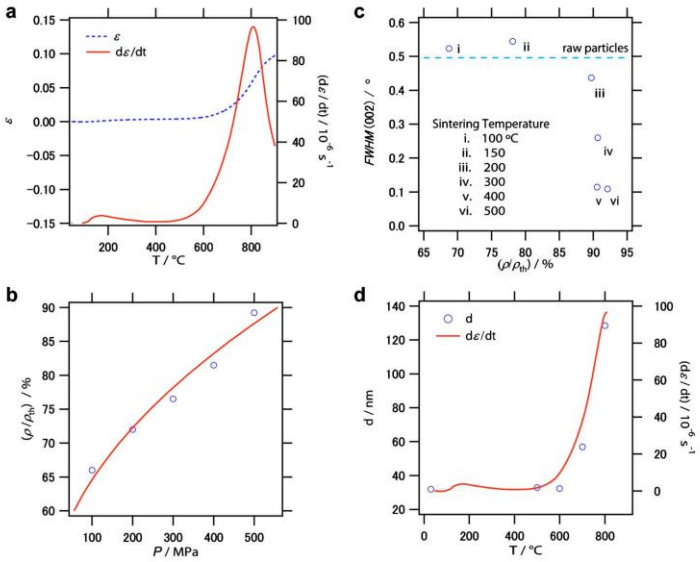

FIG. 1. (Color online) Evolution of density and grain size via heating and/or pressing. Shrinkage, ε, and its rate, $d\varepsilon/dt$, of ZnO nanoparticles of 28 nm during heating without external pressure (a), relative density, ρ/ρ_{th}, as a function of external pressure, P, at 200 °C (b), FWHM, of 002 diffraction and relative density with respect to heating temperature under a pressure of 500 MPa (c), and increase in grain size, d, in densified samples at different annealing temperatures (d). These results indicate that nanoparticles of ZnO densified at surprisingly low temperatures with the assistance of 500 MPa external pressure and the nanoparticle size was retained in the densified samples. Furthermore, the obtained nanograins show no apparent growth up to 600 °C.

the range of EDS analysis [Fig. 2(c)]. The absence of secondary phase at the grain boundary according to high-resolution TEM images also supported the high homogeneity of the sample [Fig. 2(d)].

B. Transport properties

Such numerous boundaries should explicitly influence the transport properties such as thermal conductivity. The

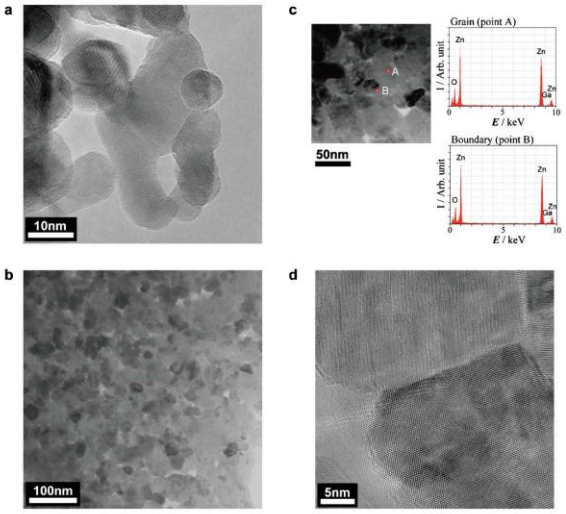

FIG. 2. (Color online) TEM images of nanograined bulk ZnO. Starting nanoparticles (a), densified bulk (b), EDS analysis at grain interior and grain boundary (c), and high-resolution image of densified bulk (d). All of the images indicate chemically homogeneous and well-crystallized samples of the synthesized nanograined bulk.

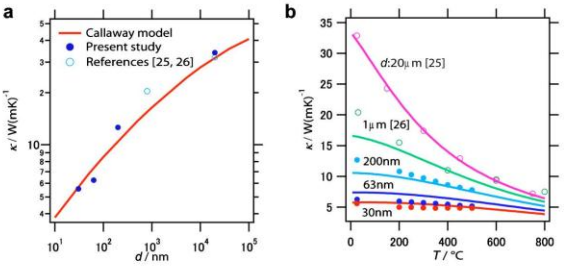

FIG. 3. (Color online) Influence of boundary-scattering on thermal conductivity, κ. The dependence of κ at room temperature on the grain size (a) and the temperature dependence of κ for different grain size, d (b). Solid lines indicate prediction based on the Callaway model in which the effect of boundary-scattering was taken into account. In addition, the phonon contribution governs this data due to the low electrical conductivity of samples.

influence of the boundary on thermal conductivity by phonon scattering is formulated by Callaway as follows:[23]

$$\kappa = CT^3 \int_0^{\theta_D/T} \frac{x^4 e^x (e^x - 1)^{-2}}{\alpha T^4 x^4 + (\beta_1 + \beta_2) T^5 x^2 + v/L} dx + \kappa_2,$$

$$C = \frac{k_B}{2\pi^2 v}\left(\frac{k_B}{\hbar}\right), \quad x = \frac{\hbar\omega}{k_B T},$$

where T is absolute temperature, θ_D is Debye temperature, v is phonon velocity, L is characteristic length of material, ω is circular frequency, k_B is Boltzmann constant and $\hbar$ is Planck constant. κ_2 is a correction due to the conservative nature of the N process and is generally ignored in numerical calculations. In this equation, three scattering processes are considered as expressed by three terms in the denominator: (i) impurity scattering, in which relaxation time is proportional to ω^{-4} and is independent of temperature, (ii) three-phonon scattering, in which relaxation time is proportional to $(\omega^2 T^3)^{-1}$, and (iii) boundary-scattering, expressed as L/v. In the present case, L would be represented by the grain size. Normally, the boundary-scattering is dominant only at low temperatures typically below ~10 K, and both the impurity and the three-phonon scattering mostly govern the thermal conductivity above room temperature. The impact of boundary-scattering in ZnO is shown in Fig. 3. It is clear that the reduction in grain size led to thermal conductivity lower than that of conventionally prepared ceramics (~30 W/mK) (Refs. 24–26) [Fig. 3(a)]. In addition, the thermal conductivity of the single crystal is naturally high and exceeds 100 W/mK,[27] so the thermal conductivity was reduced by less than one-tenth by the boundary-scattering. As for the temperature dependence of thermal conductivity, smaller the grain size, lower the dependence, which also supports the dominant influence of boundary-scattering in nanograined ZnO. To confirm the boundary-scattering effect quantitatively, we fitted the Callaway model to the observed thermal conductivities, in which the electron contribution was negligible according to the Wiedemann–Franz law. For conventionally prepared ceramics, θ_D of 400 K,[28] v of 3.4×10^3 m/s,[29] L of 20 μm were known experimentally, and α and $(\beta_1+\beta_2)$ were numerically optimized as 5.0×10^2 $K^{-4}s^{-1}$ and 1.1×10^{-2} $K^{-5}s^{-1}$, respectively. Then L was varied based on the observed grain size, while the other parameters were fixed. Corresponding to the optimized values, the phonon mean free paths for each scattering are estimated to be 4 nm and 300 nm (at 300 K) for impurity scattering and three-phonon scattering, respectively. The former value corresponds well to $n^{-1/3}$ (n: carrier concentration), suggesting that the dopant acts as the scattering center. The lines in Fig. 3 indicate the prediction based on the Callaway model, which shows reasonable agreement with the experimental data. Therefore, we can conclude that the effect of nanostructuring on thermal conductivity is principally due to the boundary-scattering.

The boundary influence on electric transport is summarized in Fig. 4. As with the Seebeck coefficient, mostly identical values were observed among the samples. This fact indicates lesser effect of boundary-scattering on the Seebeck coefficient. Theoretically, the Seebeck coefficient can be estimated based on the Boltzmann equation as follows:

$$S = -\frac{k_B}{e}\left[\frac{r+2}{r+1}\frac{F_{r+1}(\xi)}{F_r(\xi)} - \xi\right],$$

where e is the elementary electric charge, r is scattering parameter, $F_r(\xi)$ is Fermi–Dirac integral and ξ is Fermi energy. The Fermi–Dirac integral is expressed as

$$F_r(\xi) = \int_0^\infty \frac{x^r}{1 + \exp(x - \xi)} dx.$$

Based on the experimentally known n and effective mass (m^*), we fixed ξ to satisfy the relationship as follows:

$$n = 4\pi\left(\frac{2m^* k_B T}{h^2}\right)^{3/2} F_{1/2}(\xi).$$

The lines in the figure show the theoretical prediction based on the above equations for $r = 1/2$ or 0, where m^*/m_e of 0.28 (Ref. 30) and n of 6×10^{19} cm^{-3} were adopted. The $r=0$ corresponds to acoustic phonon scattering, which is dominant at high temperatures, while $r = 1/2$ is responsible for neutral impurity scattering.[31] It can be seen that the observed Seebeck coefficient is in the range of $r=0$ to 1/2, indicating that carrier concentration and effective mass reasonably determine the Seebeck coefficient in the nanograined ZnO.

Although the influence of boundary-scattering was not significant in the Seebeck coefficient, the electrical conductivity showed dependence on grain size: smaller the size, lower the electrical conductivity. For a size of 20 μm, the electrical conductivity decreased with temperature, indicating a degenerate semiconductor at this doping level. However, this temperature dependence gradually changed with

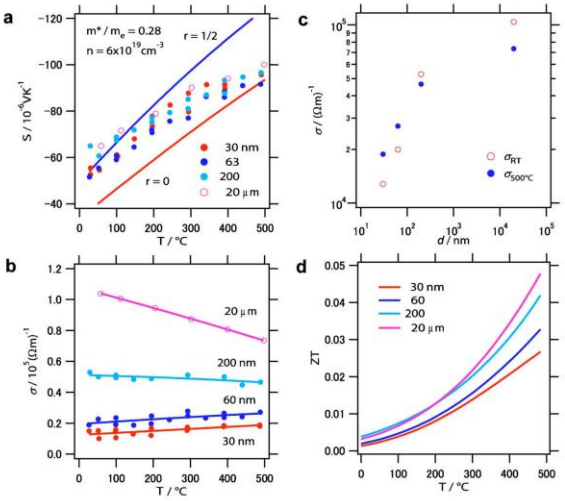

FIG. 4. (Color online) Electron transport and dimensionless figure of merit for different grain size. Seebeck coefficient, S, (a), electrical conductivity, σ, (b), dependence of σ on the grain size, d, at room temperature (c), and dimensionless figure of merit, ZT, (d). ZT was gradually reduced with smaller grain size, which originated from stronger electron scattering at the grain boundary compared with phonon scattering, while the Seebeck coefficient was insensitive to the boundary.

decrease in grain size and thermally activated conduction became significant for smaller grains. This is most likely due to the potential barrier at the grain boundary.

In addition, several models for improving the power factor, $S^2\sigma$, by nanostructuring are proposed, such as an energy filtering effect,[32] which is often quoted as a reason for the increase in Seebeck coefficient in nanostructured bulk materials.[1,9] This energy filtering effect is connected to a potential barrier that forms at the interface in semiconductors. In cases where the height of the barrier is close to the Fermi level, the low-energy carrier is screened out by the barrier depending on its energy, which gives rise to the increase in Seebeck coefficient with moderate reduction in electrical conductivity. Assuming that the potential barrier caused the difference in the activation energies of electrical conductivities between large grain and nanograin samples, we estimated the height based on Arrhenius plot of conductivity. As a result, the height of 30 nm grained ZnO was 41 mV higher than that of 20 μm grained ZnO. This barrier height is enough to increase the Seebeck coefficient according to the theory of energy filtering. In addition, the distance between barriers is also fundamental because restoration of electron distribution function due to inelastic collisions occurs when the distance reaches a certain length (l_e). Estimated l_e based on hot electron theory[33] was 3000–4000 times larger than the electron mean free path. Taking account of the mean free path of several nanometers of the sample, energy filtering is expected to occur, which contradicts the observed results. Further consideration of the energy filtering effect is required.

The dimensionless figure of merit (ZT), which is given by $S^2\sigma\kappa^{-1}T$, is summarized in Fig. 4(d). The trend clearly shows an increase in ZT with grain size, especially at high temperatures. At high temperatures, phonon scattering mostly dominates the transport, which hides the effect of boundary-scattering. Thus, the effect of nanostructuring relatively diminishes with temperature. The unfavorable trend of nanograins is that the reduction in thermal conductivity is overcompensated by the reduction in electrical conductivity. No enhancement in Seebeck coefficient is another reason for the low ZT, which poses a question about the potential barrier effect in this system.

IV. SUMMARY

A bulk process for a nanograined oxide has been demonstrated. This process effectively densifies nanoparticles without grain growth, which provides the opportunity to analyze the effects of nanostructuring in the thermoelectric bulk material comprehensively. Significant reduction in thermal conductivity was realized via nanograin in ZnO, which was well explained by the Callaway model, indicating that enhanced boundary-scattering dominates the thermal conductivity in nanograined ZnO. On the contrary, the Seebeck coefficient was insensitive to the nanostructure, and was governed by effective mass and carrier concentration as seen in conventional thermoelectric materials. Since the boundary-scattering also reduced the electric conductivity, overcompensating for the reduced thermal conductivity, ZT of the nanograined bulk was found to be moderate. Nevertheless, the present process offers a rational experimental approach for the discovery of high ZT bulk materials with nanostructuring, especially for oxides, which may contribute to effective energy utilization in the future.

[1]M. S. Dresselhaus, G. Chen, M. Y. Tang, R. G. Yang, H. Lee, D. Z. Wang, Z. F. Ren, J.-P. Fleurial, and P. Gogna, Adv. Mater. (Weinheim, Ger.) **19**, 1043 (2007).
[2]L. D. Hicks, T. C. Harman, X. Sun, and M. S. Dresselhaus, Phys. Rev. B **53**, R10493 (1996).
[3]T. Koga, S. B. Cronin, M. S. Dresselhaus, J. L. Liu, and K. L. Wang, Appl. Phys. Lett. **77**, 1490 (2000).

[4]R. Venkatasubramanian, E. Siivola, T. Colpitts, and B. O'Quinn, Nature (London) **413**, 597 (2001).
[5]T. C. Harman, P. J. Taylor, M. P. Walsh, and B. E. LaForge, Science **297**, 2229 (2002).
[6]H. Ohta, S. W. Kim, Y. Mune, T. Mizoguchi, K. Nomura, S. Ohta, T. Nomura, Y. Nakanishi, Y. Ikuhara, M. Hirano, H. Hosono, and K. Koumoto, Nature Mater. **6**, 129 (2007).
[7]A. I. Boukai, Y. Bunimovich, J. Tahir-Kheli, J.-K. Yu, W. A. Goddard III, and J. R. Heath, Nature (London) **451**, 168 (2008).
[8]A. I. Hochbaum, R. Chen, R. D. Delgado, W. Liang, E. C. Garnett, M. Najarian, A. Majumdar, and P. Yang, Nature (London) **451**, 163 (2008).
[9]B. Poudel, Q. Hao, Y. Ma, Y. Lan, A. Minnich, B. Yu, X. Yan, D. Wang, A. Muto, D. Vashaee, X. Chen, J. Liu, M. S. Dresselhaus, G. Chen, and Z. Ren, Science **320**, 634 (2008).
[10]T. Okuda, K. Nakanishi, S. Miyasaka, and Y. Tokura, Phys. Rev. B **63**, 113104 (2001).
[11]I. Terasaki, Y. Sasago, and K. Uchinokura, Phys. Rev. B **56**, R12685 (1997).
[12]A. C. Masset, C. Michel, A. Maignan, M. Hervieu, O. Toulemonde, F. Studer, and B. Raveau, and J. Hejtmanek, Phys. Rev. B **62**, 166 (2000).
[13]Y. Sun, G. M. Fuge, N. A. Fox, D. J. Riley, and M. N. R. Ashfold, Adv. Mater. (Weinheim, Ger.) **17**, 2477 (2005).
[14]E. Hosono, S. Fujihara, I. Honna, and H. S. Zhou, Adv. Mater. (Weinheim, Ger.) **17**, 2091 (2005).
[15]H. Q. Yan, R. R. He, J. Pham, and P. D. Yang, Adv. Mater. (Weinheim, Ger.) **15**, 402 (2003).
[16]A. Satake, H. Tanaka, T. Ohkawa, T. Fujii, and I. Terasaki, J. Appl. Phys. **96**, 931 (2004).
[17]I. W. Chen and X. H. Wang, Nature (London) **404**, 168 (2000).
[18]Y. Kinemuchi and K. Watari, J. Eur. Ceram. Soc. **28**, 2019 (2008).
[19]J. P. Wiff, Y. Kinemuchi, and K. Watari, Mater. Lett. **63**, 2470 (2009).
[20]Y. Kinemuchi, H. Nakano, M. Mikami, K. Kobayashi, K. Watari, and Y. Hotta, "Thermoelectric properties of nanograined ZnO," J. Electron. Mater. (to be published).
[21]E. Arzt, M. F. Ashby, and K. E. Easterling, Metall. Trans. A **14**, 211 (1983).
[22]I. Yonenaga, H. Koizumi, Y. Ohno, and T. Taishi, J. Appl. Phys. **103**, 093502 (2008).
[23]J. Callaway, Phys. Rev. **113**, 1046 (1959).
[24]M. Ohtaki, T. Tsubota, K. Eguchi, and H. Arai, J. Appl. Phys. **79**, 1816 (1996).
[25]H. Kaga, Y. Kinemuchi, S. Tanaka, A. Makiya, Z. Kato, K. Uematsu, and K. Watari, Jpn. J. Appl. Phys., Part 2 **45**, L1212 (2006).
[26]Y. Fujishiro, M. Miyata, M. Awano, and K. Maeda, J. Am. Ceram. Soc. **86**, 2063 (2003).
[27]M. W. Wolf and J. J. Martin, Phys. Status Solidi A **17**, 215 (1973).
[28]W. N. Lawless and T. K. Gupta, J. Appl. Phys. **60**, 607 (1986).
[29]N. Soga and O. L. Anderson, J. Appl. Phys. **38**, 2985 (1967).
[30]K. Ellmer, J. Phys. D: Appl. Phys. **34**, 3097 (2001).
[31]D. L. Young, T. J. Coutts, V. I. Kaydanov, A. S. Gilmore, and W. P. Mulligan, J. Vac. Sci. Technol. A **18**, 2978 (2000).
[32]Y. I. Ravich, in *CRC Handbook of Thermoelectrics*, edited by D. M. Rowe (CRC, Boca Raton, 1995), Chap. 7, p. 67.
[33]Y. Nishio and T. Hirano, Jpn. J. Appl. Phys., Part 1 **36**, 170 (1997).

[4]R. Venkatasubramanian, E. Siivola, T. Colpitts, and B. O'Quinn, Nature (London) **413**, 597 (2001).
[5]T. C. Harman, P. J. Taylor, M. P. Walsh, and B. E. LaForge, Science **297**, 2229 (2002).
[6]H. Ohta, S. W. Kim, Y. Mune, T. Mizoguchi, K. Nomura, S. Ohta, T. Nomura, Y. Nakanishi, Y. Ikuhara, M. Hirano, H. Hosono, and K. Koumoto, Nature Mater. **6**, 129 (2007).
[7]A. I. Boukai, Y. Bunimovich, J. Tahir-Kheli, J.-K. Yu, W. A. Goddard III, and J. R. Heath, Nature (London) **451**, 168 (2008).
[8]A. I. Hochbaum, R. Chen, R. D. Delgado, W. Liang, E. C. Garnett, M. Najarian, A. Majumdar, and P. Yang, Nature (London) **451**, 163 (2008).
[9]B. Poudel, Q. Hao, Y. Ma, Y. Lan, A. Minnich, B. Yu, X. Yan, D. Wang, A. Muto, D. Vashaee, X. Chen, J. Liu, M. S. Dresselhaus, G. Chen, and Z. Ren, Science **320**, 634 (2008).
[10]T. Okuda, K. Nakanishi, S. Miyasaka, and Y. Tokura, Phys. Rev. B **63**, 113104 (2001).
[11]I. Terasaki, Y. Sasago, and K. Uchinokura, Phys. Rev. B **56**, R12685 (1997).
[12]A. C. Masset, C. Michel, A. Maignan, M. Hervieu, O. Toulemonde, F. Studer, and B. Raveau, and J. Hejtmanek, Phys. Rev. B **62**, 166 (2000).
[13]Y. Sun, G. M. Fuge, N. A. Fox, D. J. Riley, and M. N. R. Ashfold, Adv. Mater. (Weinheim, Ger.) **17**, 2477 (2005).
[14]E. Hosono, S. Fujihara, I. Honna, and H. S. Zhou, Adv. Mater. (Weinheim, Ger.) **17**, 2091 (2005).
[15]H. Q. Yan, R. R. He, J. Pham, and P. D. Yang, Adv. Mater. (Weinheim, Ger.) **15**, 402 (2003).
[16]A. Satake, H. Tanaka, T. Ohkawa, T. Fujii, and I. Terasaki, J. Appl. Phys. **96**, 931 (2004).
[17]I. W. Chen and X. H. Wang, Nature (London) **404**, 168 (2000).
[18]Y. Kinemuchi and K. Watari, J. Eur. Ceram. Soc. **28**, 2019 (2008).
[19]J. P. Wiff, Y. Kinemuchi, and K. Watari, Mater. Lett. **63**, 2470 (2009).
[20]Y. Kinemuchi, H. Nakano, M. Mikami, K. Kobayashi, K. Watari, and Y. Hotta, "Thermoelectric properties of nanograined ZnO," J. Electron. Mater. (to be published).
[21]E. Arzt, M. F. Ashby, and K. E. Easterling, Metall. Trans. A **14**, 211 (1983).
[22]I. Yonenaga, H. Koizumi, Y. Ohno, and T. Taishi, J. Appl. Phys. **103**, 093502 (2008).
[23]J. Callaway, Phys. Rev. **113**, 1046 (1959).
[24]M. Ohtaki, T. Tsubota, K. Eguchi, and H. Arai, J. Appl. Phys. **79**, 1816 (1996).
[25]H. Kaga, Y. Kinemuchi, S. Tanaka, A. Makiya, Z. Kato, K. Uematsu, and K. Watari, Jpn. J. Appl. Phys., Part 2 **45**, L1212 (2006).
[26]Y. Fujishiro, M. Miyata, M. Awano, and K. Maeda, J. Am. Ceram. Soc. **86**, 2063 (2003).
[27]M. W. Wolf and J. J. Martin, Phys. Status Solidi A **17**, 215 (1973).
[28]W. N. Lawless and T. K. Gupta, J. Appl. Phys. **60**, 607 (1986).
[29]N. Soga and O. L. Anderson, J. Appl. Phys. **38**, 2985 (1967).
[30]K. Ellmer, J. Phys. D: Appl. Phys. **34**, 3097 (2001).
[31]D. L. Young, T. J. Coutts, V. I. Kaydanov, A. S. Gilmore, and W. P. Mulligan, J. Vac. Sci. Technol. A **18**, 2978 (2000).
[32]Y. I. Ravich, in *CRC Handbook of Thermoelectrics*, edited by D. M. Rowe (CRC, Boca Raton, 1995), Chap. 7, p. 67.
[33]Y. Nishio and T. Hirano, Jpn. J. Appl. Phys., Part 1 **36**, 170 (1997).

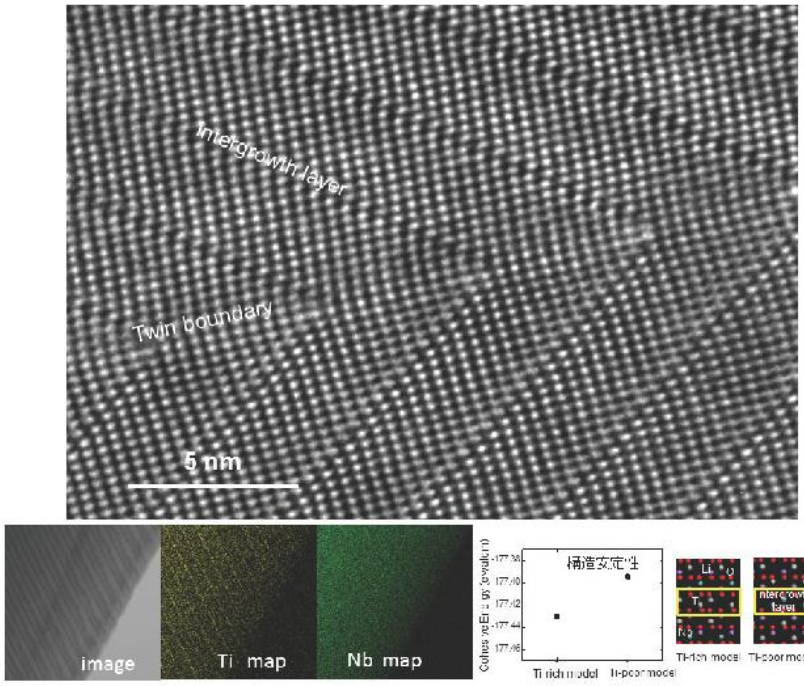

Li-Nb-Ti 系酸化物の構造異方性が作り出したミリ波照射による美的ナノ組織

出品者所属・氏名：豊橋技術科学大・中野裕美（なかのひろみ）、佐藤裕久（さとうひろひさ）、京都大・湯浅元仁（ゆあさもとひろ）、馬渕 守（まぶちまもる）

撮影者所属・氏名：豊橋技術科学大・中野裕美（なかのひろみ）

装置・撮影条件：JEM-2100F・200kV

Li-Nb-Ti 系酸化物固溶体は、限られた組成域で M-相と呼ばれる超構造を形成する固溶体として、その特異な異方性構造と誘電率の関係について研究が行われてきた。近年では、この M-相の組成域で、LED 用近紫外励起赤色蛍光体としての開発が試みられており、高い発光強度が得られ始めている。しかしながら、均質な超構造を有する Li-Nb-Ti 系酸化物固溶体の形成には、従来の電気炉では 1000 度で 3h の仮焼後、1120 度で 24h の焼結が必要であり、実用化のために低温・短時間焼結が喫緊の課題となっている。

今回、24GHz のミリ波炉(正確には 30GHz 以上がミリ波)を用いて低温・短時間焼結を試みた。その結果、仮焼なしで、1000 度でたった 1h の焼結により、均質で電気炉と同等の周期を有する超構造形成にはじめて成功した。TEM 写真は固溶体中で偶然に見つけたもので、超構造と双晶構造の複合的構造を有し、葉脈状の組織を構築しており、美的なナノ組織である。元素マッピング像は、$LiNbO_3$-like の母相中よりも intergrowth 相に Ti 原子がより多く分布していることを示し、intergrowth 相が rock-salt type の Li_2TiO_3 構造を形成している報告を支持している。なぜこのような異方性構造が、ミリ波照射により素早く合成できたのかを検証するため、第一原理計算により構造安定の指標となる cohesive energy を計算し、Ti 原子が intergrowth 相に poor に分布した場合と rich に規則配列した場合で比較した。この結果、rich に規則配列をする方がより安定であるという結論に達した。これにより、ミリ波照射下での急速焼結でも、異方性構造が安定的に形成されることが明らかになった。ミリ波焼結法は、内部加熱、選択加熱、急速加熱、また非熱効果など、電磁界との相互作用においてまだ未解明の現象を含んでいる。しかし、本研究の結果から、今後異方性構造や原子配列制御の分野への波及効果が大きいことが予想される。

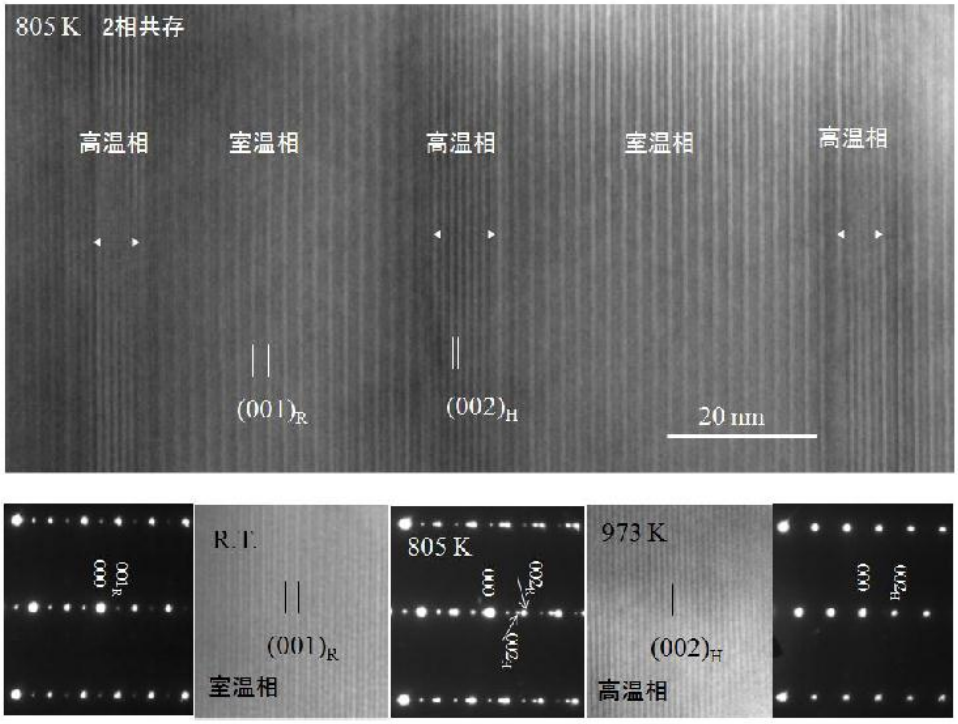

層状ペロブスカイトの一次相転移その場観察

出品者所属・氏名：豊橋技術科学大学・中野（なかの） 裕美（ひろみ）・名古屋工業大学・石沢（いしざわ） 伸夫（のぶお）

撮影者所属・氏名：豊橋技術科学大学・中野（なかの） 裕美（ひろみ）

装置・撮影条件：透過型電子顕微鏡(JEOL JEM-2100F)・200 kV 高温用ホルダー

$BaTb_2Mn_2O_7$ は、Ruddlesden-Popper 相と呼ばれる層状ペロブスカイト構造を有し、一般に $AO(ABO_3)_2$ で表記される。この構造は、ペロブスカイト層が岩塩型の層間構造で連結しており、層状コバルト酸化物が熱電材料として有名である。2 種類の結晶部位が配列して複合結晶場を形成し、電子系とフォノン系を別々に制御できるため、層状ハイブリッド結晶は、高性能発現の場としてナノブロックインテグレーションと名づけられ、新材料探索がはじまっている。このような新材料の持つ性質を、室温から高温まで正確に解析することは、材料探索において重要な課題である。

今回、$BaTb_2Mn_2O_7$ の構造相転移が一次であることを、高温 TEM その場観察により、ナノスケールではじめて明確にした。観察は、$BaTb_2Mn_2O_7$ の単結晶を砕いて Mo マイクログリッドメッシュにすくい取り、高温 TEM 用のホルダーで室温から温度を徐々に上げ、動画はビデオにより記録した。観察方位は、室温相（$P4_2/mnm$）の[100]方位で、773 K 付近から c 軸方向に矢印で示すような弱い回折反射が、基本反射の下方に出現し始めた。そこで、像(805 K)に切り替えると、高温相が母相（室温相）中に(00l)面に平行に、マルテンサイティックに出現しているのが観察できた。高温相は室温相よりも c 軸で約 1.5%長く、さらに周期の違いにより 2 相共存を明確に撮影することができた。出現した高温相は徐々に時間をかけて試料全域に広がり、973 K では高温相(monoclinic)の単一相に変化した。一般にペロブスカイトの構造相転移は、酸素八面体の傾斜にもとづく逐次相転移であり、空間群との関係が体系化されている。しかし、今回の一次相転移は、これまでの逐次相転移とは異なるものであり、Mn^{3+}イオンによるヤーンテラー効果と、2 種類の結晶部位が配列した複合結晶のひずみの緩和が引き起こしたものであると考える。このような特異な変化を時系列で撮影することができるのは、高温 TEM の最大の利点であり、2 相共存を確認できたことにより一次相転移であることを証明できた。今回の結果は、同系列の材料で、同様の相転移の可能性を示唆するものである。